IMU-Based Estimation of Human Lower Body Kinematics and Applications to Extravehicular Operations

by

Timothy M. McGrath

B.S., Mississippi State University (2015)
S.M., Massachusetts Institute of Technology (2017)

Submitted to the Department of Aeronautics and Astronautics
in partial fulfillment of the requirements for the degree of

Doctor of Philosophy

at the

MASSACHUSETTS INSTITUTE OF TECHNOLOGY

February 2021

Author .....
Department of Aeronautics and Astronautics
January 7, 2021

Certified by .....
Leia A. Stirling, PhD
Associate Professor, Aeronautics and Astronautics
Thesis Supervisor

Accepted by .....
Zoltán Spakovszky
Professor, Aeronautics and Astronautics
Chair, Graduate Program Committee

IMU-Based Estimation of Human Lower Body Kinematics and Applications to Extravehicular Operations

by

Timothy M. McGrath

Submitted to the Department of Aeronautics and Astronautics
on January 7, 2021, in partial fulfillment of the
requirements for the degree of
Doctor of Philosophy

Abstract

The use of body-worn inertial measurement units (IMUs) as an alternative to traditional human optical motion capture (OMC) techniques has gained increasing attention over the last twenty years. In contrast to traditional OMC, IMUs are less intrusive and allow measurements to be taken in the environment of interest—not just a contrived laboratory space. The primary goal of this work is to advance human-IMU kinematic modeling and estimation techniques through increasing the accuracy of IMU-derived human skeletal joint angles while minimizing the required calibration necessary to use an IMU-based human mocap system. A secondary goal of this work is to demonstrate practical application of an IMU-based mocap system to a specific domain of interest: space suit design and operations. In this domain, IMUs offer a tractable approach to understanding suited or unsuited human kinematics in the field. The capture of these kinematics in relevant environments allow engineers to better design and maintain space suits as well as model the operational paradigms which enable the future of human extraplanetary spaceflight.

Thesis Supervisor: Leia A. Stirling, PhD
Title: Associate Professor, Aeronautics and Astronautics

Acknowledgments

I began graduate school in August of 2015, which seems like eons ago. These past few years have been quite the journey. There have been innumerable people who affected me during this time. Sometimes it's a focused whiteboard learning session, and sometimes it's a moment that isn't as lonely. All of these people have impacted me, and I'm better for having known them.

First, to my advisor, Leia Stirling. Thank you so much for your years of patience, kindness, and guidance. You've done a wonderful job of providing me an environment to learn, explore, fail, succeed, grow and work. You played a crucial role in shaping how I approach open ended problems and interpret data. Despite this, I think the advising role you took on is perhaps the easy part—at least, it's the part you're formally trained for. What makes you such an exceptional advisor is *everything else*. From the moment I began at MIT, you emphasized self care and displayed so much empathy for your students and the larger world. You're a dedicated mother, wife, and friend. You encourage your students to be the same. At some level, it was expected that I'd receive good technical advising at MIT. But to be advised by such great human is the real privilege. Under your guidance, I got to grow as an engineer—but I also got to grow as person. I think it's easy to express gratitude for the former, but a lot harder to express gratitude for the latter. Thank you.

I've also had a stellar committee. Prof. Damian Kelty-Stephen and Prof. Nick Roy have been a pleasure to work with. Both have made time in their busy schedules to meet with me personally and answer technical questions related to my work, as well as perform the standard committee tasks. Technical capability

aside, it should be noted that both have reputations that precede them with regard to caring for students in their departments. Everyone around Prof. Kelty-Stephen knows his student-first teaching and advising philosophy. For much of my time in graduate school, Prof. Roy has been an integral part of the MIT AeroAstro Department's DI&I committee. Thank you both for your time you've given me, and also thank you for the time you've dedicated to making the world just a little bit better. Prof. Dava Newman and Dr. Matthew Miller also served as readers on this thesis. Prof. Newman has been a fixture in my graduate education well before this thesis, co-leading the Human Systems Labratory (HSL). Her steady leadership, commitment to the world, and dedication to the lab's students have been just as important as her feedback on this thesis. I've had the pleasure to work with Dr. Miller personally these past few years. He is young, energetic, and willing to push boundaries in all the right places. I believe deeply in his work and his future scientific endeavors at NASA.

Next, to the faculty and research staff within the Human Systems Laboratory: Leia, Dava, Jeff, Larry, Chuck, and Andy. Together, you've all built and maintained a laboratory that stood the test of time. It was an honor to work in that environment, get to know you and your work, and contribute to the lab myself. I've also met so many wonderful students in the lab. When I first arrived, there were many talented older students who were around to help me when needed. As I leave, there are many young students who are curious and bound to do great things. I'd especially like to acknowledge Richard and Aditi, who have been my officemates and closest lab colleagues over these years. We spent a lot of time talking about everything that wasn't research, and those conversations definitely broke the monotony. An additional thanks goes to all of those who participated in my research experiments.

Our lab and department have been supported by many great people who made

my life better. It's a long list, but I'd specifically like to thank Sally Chapman, Beata Shuster, Beth Marois, Liz Zotos, Marie Stuppard, Anthony Zolnik, Denise Phillips, Pam Fradkin, Bryt Bradley, and Joyce Light. All of these people have been instrumental in helping me through graduate school. Sometimes in official capacities, sometimes in smiles and positive thoughts. Thank you all so much for your time and kindness.

I'm fortunate to have a list of friends in Boston that are too long to list here. But graduate school wouldn't have been possible without them. Thanks to Ben and Chris for the gym group. Thanks to Kris, Chris, Toño, and Igor for the software and estimation advice. Thanks to Akil, Tony, Pem, Gerardo, and Ashwin for the camaraderie. Thanks to everyone (and those not listed) for the good times and making graduate school fun. And a special thanks to Mike and everyone at the Muddy Charles Pub. Your beer was cold, cheap, and served at just the right times in life.

I'm so thankful to my family for the love and support they've given me over the years. My parents, Tim and Cheryl, worked tirelessly to provide for our family and support my sister and I through sports, school, hardships, celebrations, and everything in between. In my immediate relatives, no one had ever gone to college. But because of my parents' values and effort, both of their children would graduate from college with multiple degrees. My younger sister, Amber, has been the face of perseverance. You inspire me in so many ways. My grandmother, Faye, and my aunt and uncle, Rosalyn and David, and have also been a constant source of love and support. I love all of you so much, thank you for making this possible.

Finally, to my fiancée Paromita—my best friend, and the love of my life. You've supported me in countless ways and I can't thank you enough. You are kind, loving, intelligent, beautiful. You're an incredible engineer and leader. You inspire

so many people—me most of all. NASA is lucky to have you. We've grown and changed significantly since we first met, and we've done it together in love. Your family—Ratna, Amal, and Amlan—have loved and encouraged me and given me a brand new family. Visiting your extended family in Bangladesh made me fall in love with you, your culture, and your values all over again. I'm so thankful to the new family I've made, and to the family I haven't met yet. One day we'll have a family of our own, and I can only hope our children have a fraction of your love, commitment, wonder, and strength. I can't wait to marry you.

"Theory attracts practice as the magnet attracts iron."

– Johann Carl Friedrich Gauss

Contents

List of Figures

List of Tables

Chapter 1

Introduction

1.1 Motivation

Assessment of human motion informs measures of human health and performance as well as suitability of systems with which a human interacts. In clinical rehabilitation, assessing the range of motion of a human joint may inform the plan of care. In baseball, how much torque a pitcher generates at the elbow drives pitch speed. In exoskeleton design, differences between the human and exoskeleton joint angle is used as a measure of system fluency. The study of human motion spans many fields, including medicine, biomechanics, kinesiology, human factors—just to name a few. Requisite to all of these fields lies a common task: measuring human motion in a way which is interpretable to end users.

Among human motion capture methods, optical motion capture (OMC) represents the current gold standard [34]. These approaches generally involve mounting a set of reflective markers to the human subject. A set of pre-positioned cameras around the capture volume then record the 3D position of each marker in space.

Many modern systems use cameras which emit an infrared light, which is reflected from a marker back into the camera lens. From the constant speed of light, the distance to the marker can be approximated. With multiple cameras measuring the same marker, the 3D position of this marker can be triangulated.

Camera-based OMC is accurate at localizing the 3D position of the reflective markers within the capture volume. However, additional modeling approaches (e.g., OpenSim [55] or the Vicon plugin gait model [52, 88, 197, 24]) are required to infer the biomechanical quantities of interest—joint angles, skeletal position, etc.—from the marker positions. This approach is financially expensive due to the equipment required to collect the data and can be cumbersome to post-process. The subject must be fitted in non-reflective clothing with markers placed precisely at anatomical landmarks. Any misplacement would manifest itself as an error in the estimation of joint angles. The infrared cameras must be calibrated and posed properly to view a necessarily-large capture volume, and suffer from marker dropout when the markers are occluded by the subject or another object. Generally, camera-based OMC must take place in a controlled laboratory environment [66]. This approach is a valuable research tool, but can be inappropriate for the clinician, sports performance expert, or engineer when measurements need to be made at low cost and in the environment of interest.

Markerless camera-based computer vision systems are an emerging alternative, however have not found widespread adoption in biomechanics applications [41] likely due to unclear accuracy and validation of these systems against more accepted methods. Multiple reviews [134, 152, 205] have covered these approaches in detail. Problem formulations generally vary in depth map representation, image segmentation methodology, and human skeletal pose parameterization, as well as solver approach. Although these approaches are promising, it is currently unclear

whether these approaches can achieve the accuracy expected in scientific study and whether these approaches can be useful in field environments [41].

Small, wearable inertial measurement units (IMUs) have garnered interest as a low-cost, in-the-field alternative to camera-based methods. These sensor packages typically measure acceleration and angular velocity, and are often augmented with local magnetic field measurements to aid in heading estimation. IMUs have classically been used for inertial navigation on aerospace and nautical systems [4, 6, 78]. Modern IMUs mounted on the human body are compact and offer motion estimation without external equipment and a line-of-sight requirement. Approaches are developed to overcome the major disadvantages of IMUs, namely system noise and drift of estimated quantities (e.g., [213, 86, 82, 83, 26, 204]). Along with developed human-body modeling approaches, IMUs have found multiple uses for human studies including clinical sciences [139, 140, 188, 28, 73], sports performance [141, 47, 38, 48, 191], activity recognition [202, 101, 36, 179, 18], occupational ergonomics [111], and even spacesuit fit evaluation [67].

Among clinical applications, IMUs have been utilized in the assessment and treatment of Parkinson's disease [120, 32, 168, 27, 177], Huntington disease [91], general gait analysis [28, 85], balance assessment [20], post-stroke rehabilitation [184, 201, 84, 27], multiple sclerosis [189] and even breathing parameters [33]. Many clinical approaches are based on ad-hoc, directly measured quantities (e.g., Jarchi et al. [85] reviews gait analysis approaches which only rely only on various interpretations of the accelerometer signal). Differences in modeling approach and expected accuracy of the system may be driven by the clinically-relevant measures the system seeks to assess. For example, assessment of progress in physical rehabilitation or diagnosis of gait disorders often necessitate accurate measurements of human joint angles [35], whereas the diagnosis and characterization of

Parkinsonian tremors may be done from direct accelerometry analysis [109, 16].

An additional application of interest is toward extravehicular operations and space suit design. Extravehicular activity (EVA) necessarily exists in field environments—i.e., the vacuum of space or the surface of other planetary bodies. In these environments, optical motion capture or camera-based systems are intractable to use. Additionally, it is well documented that there are differences in kinematics between the space suit and the human operator *inside* of the space suit [9]. However, the space suit would occlude any camera-based approach from measuring the human's kinematics. Body-worn IMUs, in contrast, can measure human motion in these extreme environments inside of the suit.

This thesis seeks to advance knowledge in IMU-based estimation of human kinematics, as well as offer operationally-relevant approaches to space suit design and evaluation. The remainder of this section presents additional introduction to IMU-based human estimation techniques (Section 1.2) and its application to operations for future spaceflight missions (Section 1.3).

1.2 IMU-Based Human Kinematics Estimation

One major consideration to be made when using IMU-based human modeling approaches is prescribing or estimating the relationship between the IMU coordinate frame on the surface of the body segment and the underlying skeletal system in which many biomechanical quantities of interest are defined, sometimes referred to as the IMU-to-segment (I2S) pose relationship. A recent review by Vitali and Perkins [192] places these methods into four distinct categories—(1) assumed alignment methods, (2) functional alignment methods, (3) model based methods, and (4) augmented data methods. Assumed alignment approaches have considered

a priori alignment of the IMU to the human skeletal system [113]. Mayagoitia et al. [122] used aligned gyroscope and accelerometer packages to track pitch angle of the shank to an error of $2.7^\circ \pm 2.8^\circ$. Favre et al. [65, 64] precisely aligns one of the axes of the IMU with the knee's major rotation axis. After determining the I2S relationship from a priori measurement and a static calibration routine [157], Kok et al. [97] formulates the problem as a maximum a posteriori (MAP) estimation problem, solved through weighted least squares optimization, including estimation of the offset vectors from neighboring segment coordinate systems to their common point-revolute joint. These methods are limited by the operator's ability to precisely align the IMU, or their ability to measure the alignment offset. Functional alignment methods have considered using static or dynamic calibrations (referred to as *functional* calibrations) which the human subject must perform in order to determine the alignment between the IMU and the skeletal system. Favre et al. [63, 62] prescribes a functional calibration set with a subsequent root mean square error (RMSE) of the knee's three major rotation angles between 4.0° and 8.1°. Many other works have also used functional calibration to aid in estimation of segment kinematics [214, 114, 145, 43, 182, 46, 190, 3]. These methods may be confounded by the subject's ability to perform the prescribed calibrations.

More recently, efforts have shifted towards overcoming these limitations of functional or static calibrations. In this work, the phrase *self-calibrating* is used to describe model-based approaches which either (a) estimate the pose relationship between the IMU and underlying bone segment coordinate system (i.e., the I2S relationship), or (b) which can derive relevant biomechanical parameters of the human skeleton (such as joint angles) without directly estimating the I2S relationship. These approaches generally exploit kinematic relationships which exist between IMUs mounted on a semi-rigid-body about a fixed-point rotating joint.

Müller et al. [137] models the elbow as a 2DOF system, and argues that the magnitude of the relative angular velocity about the joint may be decomposed into axis components through a formulated optimization problem. Seel et al. [172, 170] presents an optimization-based approach to estimating joint axis and position in the IMU frames from measured angular velocities and accelerations for the knee and ankle joints. This method is expanded on by Salehi et al. [164] with a modified measurement model of the IMU positions relative to their neighboring joints to aid in accuracy and observability. Taetz et al. [183] presents a similar problem solved via a sliding-window weighted least squares algorithm, but with the novel addition of assuming a topology on which the IMU is mounted. In that work, the authors assume a capsule-type shape, but note that other shapes can be included. Recently, Olsson et al. [146] suggests an additional subset of the self-calibrating approaches: *plug-and-play* approaches. In their work, they describe this category to be approaches which note when or whether a sufficient calibration has been obtained from otherwise arbitrary motions. Often, these works estimate or otherwise kinematically include (i.e., through a priori measurement) an I2S calibration parameter for each IMU [130, 97, 183], typically modeled as a static $SE(3)$ transformation between the underlying limb coordinate system and the coordinate system of the IMU on the limb surface. Other works [128, 131, 172, 170, 137] seek to derive relevant biomechanical states without directly estimating the underlying skeletal coordinate systems, a potentially minimal parameterization of the problem. There are two major motivations for the latter approach: first, as noted in Taetz et al. [183], to estimate both the IMU coordinate system trajectory and the skeletal coordinate system trajectory (when the I2S relationship is assumed static) is a redundant variable set. Secondly, when mathematical relationships are cast as a function of skeletal coordinate system (rather than IMU coordinate system), the resultant

noise distributions are often immeasurable. For example, as of this publication, the authors are not aware of attempts to measure the noise distribution of (a) bone connection "error" at a single rotation center (i.e., the constraint first proposed by Kok et al. [97] and used by subsequent works [183]) when the constraint is cast in the skeletal coordinate system or (b) the distribution of the aforementioned static I2S parameter in $SE(3)$, although efforts have been made [129] to investigate the sensitivity of the optimized solution to the accuracy of this parameter. This modeling dichotomy deserves continued investigation.

These works also vary in their solution methodology. Many consider general batch optimization [97, 172, 170, 137], while others have considered sliding window approaches [183], or filtering approaches [3]. Recently, Kok et al. [99] reconsiders the optimization problem [97] but with a more efficient approach to selection of search direction, using a message passing algorithm [148].

Another consideration is that magnetometers are notoriously unreliable indoors [158, 53] due to the presence of electromagnetic disturbances. While some works have considered compensation or recalibration for these disturbances [106, 37, 100, 108], many works avoid the use of magnetometers altogether [105, 97]. Without the use of magnetometers, IMUs typically do not have a heading reference, leaving the yaw degree of freedom generally unobservable in the case of traditional dead-reckoning for IMU pose trajectory. Therefore, exploiting kinematic constraints inherent to the human skeletal system (cast in local frames, i.e., between body segments) may improve observability [164], however, may not provide *absolute* observability of IMU heading angle, i.e., all solutions rotated about the global vertical axis are equivalent. Discerning the heading relationship between two IMUs flanking a joint may be possible using an approach which leverages a model of a static vector pair from the joint to the neighboring IMUs, e.g., [97], however, when

these vectors lie normal to the horizontal plane they may not provide sufficient information. Tasks such as upright gait are likely to have static vectors from the IMU to joint centers that are directed proximal or distal on the limb, which would be approximately parallel to the global upward vector. In these situations, more information is necessary to discern the heading relationship between two IMUs.

Finally, IMU-based skeletal pose estimation approaches also vary in the convention used to report joint angles. In order to maximize the operational relevance of the system to clinicians, it is highly recommended that conventions from the International Society of Biomechanics (ISB) are followed [198, 75, 199]. Deriving joint angles according to ISB convention has the explicit benefit of both allowing comparison across different methods and presenting angles in a common convention that is already accepted. In a recent review by Weygers et al. [195], only 7 of 31 reviewed methods followed ISB standards in reporting of joint angles or segment coordinate system pose.

1.3 Applications to Extravehicular Operations and Space Suit Design

Space environments offer an additional interesting use case for IMUs towards human kinematics, as the environments are largely limited in power and volume, radiation filled, and experienced through a thick space suit–all characteristics which make traditional OMC intractable. These dangerous environments typically necessitate meticulous planning of mission operations, so the missions are generally simulated on Earth beforehand. In these analog environments where motion capture is intractable, IMUs may offer a solution to monitor human motion, aiding

in mission planning for human safety and efficiency.

Space suits are designed to support human life and work goals beyond Earth environments. IMUs have found increasing usage in suit design and evaluation, namely due to the convenience of taking measurements in non-laboratory environments and the ability to place IMUs on the human skeleton *inside* of the suit. Di Capua and Akin [58] were the first to propose an IMU-based skeleton pose estimation systems for the occupant within the space suit. Bertrand et al. [21] studied the differences between joint angles as measured by IMUs on the human arm and suit arm. Anderson et al. [7] used IMUs and pressure sensors in-suit to characterize physical interaction between the suit and human. Fineman et al. [67] used IMUs on the human and suit to understand suit fit. Recently, Kim et al. has used IMUs to classify activities and postures while suited [92], as well as compare gait characteristics in gravity offload environments at the NASA Neutral Buoyancy Laboratory (NBL) and Active Response Gravity Offload System (ARGOS) facilities [93].

Additionally, spacesuit design considers task-specific operator range of motion [44, 169]. Suits are heavy and hard to move against, so suit design also considers minimizing effort required to move the suit to reduce injury risk and metabolic cost to operate [142]. The limited range of motion often causes operators to adapt different kinematic strategies than in unsuited operation [175], which also increases metabolic cost and injury risk. Understanding range of motion of tasks of interest therefore informs suit design for extravehicular operation. IMUs have often been used to assess range of motion in non-suited environments [15, 42, 119], and therefore may be applicable to suited studies.

The NASA Human Research Roadmap (HRR) is a comprehensive document which identifies the approach and research activities planned to address risks to

human exploration beyond low earth orbit. One relevant research question is posed in EVA Gap 11: "How do extravehicular activities operations in exploration environments increase the risk of crew injury and how can the risk be mitigated?" The prevalence of injuries experienced by astronauts in spaceflight operations is well-documented [167], even during training, including musculoskeletal injuries related to the shoulder [87, 8], back [166], hip [167] and even fingernails [147]. These musculoskeletal injuries are often associated with limited range of motion [72], but may also be caused by operator overexertion. If the suited motions to accomplish a task are considered high-risk for injury, EVA experts may want to redesign the task at hand, or reconsider the human's role in the task.

The literature in the occupational health and safety literature has associated postures (and joint deviations from a neutral posture) with injury risk of work-related musculoskeletal disorders (WRMSDs) [123, 143, 90]. Traditional ergonomics methods are performed through visual observation [111], which is notably error prone [59]. A human expert is intended to observe a worker performing a task and use expert judgement (within a number of possible WRMSD frameworks) to assess risk of WRMSD. A recent review [178] has synthesized these models into a composite classification of high-risk vs. low-risk of WRMSDs by repeated deviation from neutral posture. However, there is no universal operationally-relevant definition of what constitutes a *joint deviation*, although existing observational approaches may offer some inspiration.

One widely used observational model of interest is the Occupational Repetitive Action (OCRA) [143, 144] model for assessing biomechanical risks related to upper limb repetitive movements. In fact, standard ISO 11228-3 [69] suggests OCRA as the preferred method for risk assessment [40]. Colombini and Occhipinti [39] offer the following definition of concepts for OCRA: a *cycle* is a sequence of relatively

short technical actions repeated several times in the same way; a *technical action* is a set of motions involving one or more body segments to enable the cycle to be completed. In the case of cyclic motion, these technical actions would include the physical deviations of the joint. This definition is broad by nature, and allows users to provide their own operationally-relevant specific definitions.

As aforementioned IMU-based methods synthesize human joint angles, IMUs offer a potentially convenient solution to assessing risk of WRMSDs in situations where optical motion capture is intractable. According to Lim and D'Souza [111], current IMU-based ergonomics assessment typically expresses *intensity* of a motion or posture through ordinal categories based on joint angles (e.g., classifying trunk angle into an ordinal scale of MSD risk [12, 13]) or through some average/cumulative statistic (e.g., average arm acceleration). They state that further research is needed to develop valid and sensitive measurement of WRMSD risk relying on directly-measured exposure data. Taborri et al. [181] recently proposed one novel IMU-based algorithm for counting technical actions toward determining the OCRA frequency factor for risk assessment. Their approach used a time and amplitude threshold, counting the first minimum/maximum pair in a signal which meets these thresholds as a technical action. This approach was validated against an expert-created reference count of technical actions from video, where a large range of errors were reported (from nearly 0% to over 170%), depending on frequency of task and choice of threshold values. The approach of counting everything which meets a threshold as a technical action may lead to erroneous counting (e.g., noisy IMU signals may induce many erroneous local maxima and minima). Supporting a spectrum of technical actions, as occurs in EVA-relevant tasks, requires a method that captures the joint range magnitudes and timing, as opposed to the number of min-max pairings with a fixed threshold.

EVA-relevant kinematic data allows an opportunity to inform an additional aspect of space suit design and maintenance planning. IMU measurements of the human/suit kinematics offer a practical application toward informing expected suit joint motions. Modern suits, such as NASA's next-generation xEMU, utilize hard rotational bearing joints at the waist, hip, shoulder, and wrist [50, 51] in addition to traditional soft goods joints. These hard bearing joints designs are in part motivated by the desire to support operator mobility under increased suit pressure [5]. One requirement of interest for suit joints design is the expected joint cycles per hour, which have typically been established by studying historical Space Shuttle EVA. For example, the AX-5 space suit (an all-hard-bearing suit designed by NASA in the 1980s) was designed for 19.8 knee joint cycles per hour [155]. These requirements inform testing protocols to understand suit wear.

It may be possible to also consider wear of the space suit joints specifically through fatigue of the individual space suit hard joint bearings. The Lundberg-Palmgren [115] model (1947) represents the most commonly used approach to the prediction of rolling-element bearing fatigue life. The bearing's fatigue life is typically specified as its L_{10} life, or the the time that 90 percent of a group of bearings (i.e., identical geometry and loading) will exceed without failing by rolling-element fatigue. This criterion (typically specified in millions of bearing inner-race revolutions) is the basis for calculating bearing life and reliability today [209]. Human (or suit) worn IMUs provide a way to directly measure total rotation of the joint, allowing a bearing fatigue model like Lundberg-Palmgren to be leveraged with kinematically-relevant data.

Finally, in addition to operational information to minimize injury risk and expected suit joint motions, IMUs may offer insight into the operational paradigms which maximize crew productivity and performance. In any EVA, characterizing

the component tasks which comprise the mission is critical—informing fitness standards, exploration planning, and consumables sizing [2]. One EVA of interest for future Martian exploration is geological survey objectives, which can inform habitable Mars environments and address questions related to the search for life on Mars [81]. An ongoing project at NASA's Johnson Space Center (JSC) named Scientific Physical and Operations Characterization (SPOC) [132] seeks to characterize the physical, operational, and logistical requirements which enable productive fieldwork for an extraplanetary analog geological survey mission. This study includes classifying component movements, postures, and equipment interactions [193] through the use of body-worn IMUs.

1.4 Research Objectives and Specific Aims

The purpose of this work is to advance the current state-of-the-art in IMU-based skeletal pose estimation, including the modeling, algorithmic approaches, and reporting of results. In addition to broad advances in the literature, this work also provides a specific application: human kinematics during EVA and space suit bearing fatigue modeling. The research objective is to address these purposes—both the broad and specific—through the development of frameworks which are easily accessible for end users, e.g., clinicians and extravehicular operations experts. These modeling and solution frameworks should require minimal setup and system calibration to maximize overall system usability. Similarly, these frameworks should be described with the intent of maximizing system understanding—end users should remain informed of *if* and *when* an IMU-based human/suit kinematics technique is appropriate.

In order to achieve this research objective, the following research questions

must be addressed:

1. Can we develop a self-calibrating IMU approach for the human lower body which is accurate in both joint angle estimation and IMU pose estimation?

2. Can these IMU-based approaches provide operationally-relevant measurements for the design and testing of space suits?

These research questions are addressed through the following specific aims:

1. Estimate the human knee flexion/extension angle in gait through the development of a novel human-knee kinematic model for IMU-based knee pose estimation which is agnostic to placement of IMUs on the leg.

2. Develop a self-calibrating optimization-based smoothing approach to the IMU-based human lower-body pose estimation problem which models human kinematics and anthropometry, and

   (a) maintains IMU pitch/roll estimation accuracy vs. a single-IMU smoothing approach,

   (b) provides accurate estimation of knee (flexion/extension) and hip (flexion/extension, internal/external rotation, abduction/adduction) angles reported in ISB convention,

   (c) and demonstrates the reduction of relative IMU position drift between adjacent IMUs.

3. Propose and demonstrate

   (a) a metric of IMU-derived human joint deviation with application to space suit requirements specification

(b) and the use of IMU data to inform a representative model of expected suit bearing rotation and lifespan estimation,

both assessed for an unsuited analog EVA geological survey task.

1.5 Organization of Thesis

Chapter 2 will develop and validate an IMU-based estimator of knee flexion/extension axis and angle in a fast and efficient principal component analysis-based framework. Chapter 3 will expand this novel knee model into a least-squares optimization framework for the human lower-body, while including additional information about kinematics and anthropometry. Chapter 4 will leverage this IMU-based human kinematics estimator to develop an operational model of human joint deviation and suit bearing rotation. Finally, Chapter 5 will summarize results and contributions to the literature as well as offer future research directions.

Chapter 2

A Self-Calibrating Knee Flexion-Extension Axis Estimator using Principal Component Analysis with Inertial Sensors

This chapter will explore the development of a novel 1 DOF kinematic model of the human knee and solution approach which is agnostic to the placement of IMUs on the thigh and shank. A review of previous literature (Sec. 2.2) is given. Then the formulated model and PCA-based solution methodology are presented (Sec. 2.3). The proposed approach is validated in a multi-subject study (Sec. 2.4) and compared against an optical motion capture reference.

This chapter was published in *Sensors* and is reprinted here:
McGrath, T.; Fineman, R.; Stirling, L. An Auto-Calibrating Knee Flexion-Extension Axis Estimator Using Principal Component Analysis with Inertial Sensors. *Sensors* **2018**, *18*,

1882.

2.1 Abstract

Inertial measurement units (IMUs) have been demonstrated to reliably measure human joint angles–an essential quantity in the study of biomechanics. However, most previous literature propose IMU-based joint angle measurement systems which require manual alignment or prescribed calibration motions. This chapter presents a simple, physically-intuitive method for IMU-based measurement of the knee flexion/extension angle in gait without requiring alignment or discrete calibration, based on computationally-efficient and easy-to-implement Principle Component Analysis (PCA). The method is compared against an optical motion capture knee flexion/extension angle modeled through OpenSim. The method is evaluated using both measured and simulated IMU data in an observational study (n=15) with an absolute RMSE of 9.72° and a zero-mean RMSE of 3.49°. Variation in error across subjects was found, made emergent by the larger subject population than previous literature considers. Finally, the paper presents an explanatory model of RMSE on IMU mounting location. The observational data suggest that RMSE of the method is a function of thigh IMU perturbation and axis estimation quality. However, the effect size for these parameters is small in comparison to potential gains from improved IMU orientation estimations. Results also highlight the need to set relevant datums from which to interpret joint angles for both truth references and estimated data.

2.2 Introduction

Accurate measurement of human joint angles is central to the study of human biomechanics. Better biomechanical models and measurement systems enable more robust tools for interacting with and understanding human kinematics. For example, in rehabilita-

tion, understanding human motion informs the plan of care. For sports applications, understanding motion can lead to improved strategy development. To this end, an accurate measurement of human joint angles is desired. This measurement is complicated, as human motion is characteristically nonlinear, non-smooth, and uncorrelated in time [206]. Among measurement methods, optical motion capture represents the current gold standard [34], although other computer vision approaches [133] do exist. Optical motion capture is accurate in triangulating reflective marker position in space, but interpretation of these data as human joint angles requires an assumed human model. An often-used model is OpenSim [55]. From markers set on major anatomical landmarks of the body, a least-squares optimization to fit a model may be performed to estimate the joint angles of interest.

This approach is financially expensive due to the equipment required to collect the data, and is cumbersome to post-process. The subject must be fitted in non-reflective clothing with markers placed precisely at anatomical landmarks. Any misplacement would manifest itself as an error in the estimation of joint angles. The infrared cameras are expensive, must be calibrated and oriented properly to view a necessarily-large capture volume, and suffer from marker dropout when the markers are occluded by the subject or another object. This approach is a valuable research tool, but can be inappropriate for the clinician, sports performance expert, or engineer when measurements need to be made at low cost and in the environment of interest.

Small, wearable accelerometer, gyroscope, and magnetometer packages, in contrast, offer an inexpensive way to make robust measurements. Decades of research in state estimation and filtering have enabled the appropriate mathematical models and techniques to estimate orientation [161] in three-dimensional space. The modern inertial measurement unit (IMU) is a common tool of motion measurement in non-deforming bodies. Inertial sensors have become common as navigation components for ballistic missiles, rockets, and aircraft, and are widely used today [94]. IMUs have become smaller [77], although

magnetometers still, by nature, can become inaccurate in the presence of a disturbing magnetic field [158]. Applications of IMUs to human motion have also considered navigation through the environment [61]. Luinge et al. [113] first applied IMUs to the measurement of human limb orientation, albeit with limitations of only estimating tilt and requiring sensor calibration to a known position every 30 seconds. For normal upright gait, Mayagoitia et al. [122] used accelerometers and gyroscopes, precisely aligned to the body segment, to measure knee angle to an accuracy of at most 2.73 degrees RMSE (5.2% of gait task range of motion). The optical motion capture truth datum was assumed to be a rigid body angle between markers.

The knee's primary degree of freedom is flexion/extension with a range of motion (ROM) of approximately 142.5 degrees [25]. Minor degrees of freedom (DOF) of the knee include varus-valgus with $\pm$ 5 degrees ROM [210] and internal-external rotation with ROM of 10 degrees [104]. Whether all three knee angles are needed or only the major flexion/extension DOF is application-dependent. Some clinical applications, such as understanding knee stability [68] require estimation of the degrees of freedom with lower range of motion. Inertial methods exist to estimate 3D knee angles [65, 63], but evaluation of these methods in the minor degrees of freedom is difficult due to high measurement error relative to the ROM of the minor DOFs. In Favre et al. [65], for example, the RMSE of estimation of the knee varus-valgus angle was 35% of the joint's ROM. Markers on the thigh and shank are subject to millimeters of soft tissue motion [17], which may confound calculation of joint angles. These "truth" measurement errors, combined with the low range of the knee's minor degrees of freedom, lead to a low signal-to-noise ratio when estimating vargus/valgus and internal-external rotation. Thus, caution must be taken when estimating these lower-ROM DOF via either inertial or optical methods. Estimation of flexion/extension is inherently more robust due to a higher range of motion to measurement error ratio.

Inertial measurement techniques inherently require an understanding of the relation-

ship between the coordinate systems of the IMUs and the coordinate system of the joint in question. This relationship is established through a process of calibration, which primarily serves to align or measure relative orientation between the local frames of the IMUs and the joint's coordinate system (JCS) [75, 199, 200]–such that computed angles may be interpretable as the anatomical joint angle. One method of calibration is through precise manual alignment of the sensors on the leg segment. Favre et al. [65, 64] aligns the IMUs such that one of axes of each IMU is aligned with the knee's hinge axis while also employing a high-pass filter on the gyroscope data to minimize drift of the angle estimate. This mounting assumption is also seen in [113, 122].

Alternate methods seek to use a functional calibration procedure to estimate the relationship between the body-mounted IMUs and the anatomical axes of the joint. Zhu et al. [214] decouples the degrees of freedom of arm motion on a human subject in order to excite the degrees of freedom separately, which allows a novel Kalman filter to estimate limb segment orientation. Luinge et al. [114] prescribes a pre-defined arm rotation procedure to determine the definitions of local rotation axes in the arm. Cutti et al. [46] and Favre et al. [63, 62] each prescribe a functional calibration procedure for determination of leg segment-to-sensor orientation. Vitali et al. [190] uses two functional alignment motions to set the anatomical coordinate system of the thigh and shank. Cooper et al. [43] employs similar kinematic constraints of the knee hinge axis as above, but requires the knee hinge axis be provided by optical motion capture. These biomechanically-inspired methods offer powerful estimation tools over human-aligned techniques, especially in the presence of noisy sensors.

As IMU estimation of the knee joint angle has become more accurate, attention has shifted towards methods which require fewer functional calibrations and assumptions of alignments. Seel et al. [172, 170] presents a novel method for estimating the knee axis through a formulated optimization problem, leveraging a kinematic argument of hinge joint motion. From this axis, the angle can be computed. Müller [137] extends this concept to the

elbow, arguing that the relative angular velocity between two IMUs can be decomposed about the two major degrees of freedom of the elbow, and an optimization method is formulated to calculate those axes. These methods allow for less precise placement of the IMU on the body segment.

The relative angular velocity vector, as Müller implies, is a noteworthy quantity because it represents all relative motion between two IMUs. In the case of the knee, we simplify the knee to one degree of freedom and examine a method for estimating the primary flexion/extension axis. The relative angular velocity between an IMU on the shank and IMU on the thigh should generally point parallel to the direction of the knee hinge axis. This hinge axis should be well approximated by the principal component of the set of aforementioned relative angular velocity vectors. Principal Component Analysis (PCA) [80] is a general statistical technique to simplify high-dimensional data to a descriptive lower-dimensional structure. In biomechanics, it has been used to study coordination between time-series data [49]. Landry et al. [107] used PCA to study similarities in gait waveforms of knee angle between patients with osteoarthritis. Dillman et al. [60] used PCA in a similar way to study patients with Parkinson's disease. In the case of physical data, like angular velocities, PCA offers a computationally-efficient method to find a primary directionality of the data.

In this work, we examine the decomposition of relative angular velocity between a shank and thigh IMU into its primary component: rotation about the knee flexion/extension axis. PCA is used as a robust method to estimate this knee axis. Once the knee axis is estimated, a leg segment coordinate system may be defined for both the thigh and shank. The Euler angles between these two leg segment coordinate frames are then interpreted as the anatomical knee joint angles. For estimation of the knee's hinge axis, PCA is more computationally-efficient than previously-proposed nonlinear least-squares optimization methods and is robust to the dual-direction representation of an axis. The method requires no assumption of mounting orientation on the body of the IMUs and requires no calibra-

tion to estimate the knee flexion/extension axis, any motion of the knee will suffice. A subset of this analysis, IMU-estimated knee angle for subjects 1 and 2, was previously presented [126]. This work extends the previous work through analysis of additional subjects, developing an explanatory model of the error, and comparison of the method with ideal simulated IMU data and the method of Seet el al. [170].

To evaluate the proposed method, the knee flexion/extension axis was estimated during a timed-up-and-go (TUG) task, which is commonly associated with increased fall risk in older adults [89]. Truth data were estimated using OpenSim modeling of optical motion capture data. We hypothesize (1) that the estimated knee joint angle from the proposed IMU method will be of similar error performance to other IMU-based measurement systems. (2) Accuracy of the method may be influenced by placement of the IMUs on the leg and soft-tissue noise; these factors are formalized and investigated further.

2.3 Problem Formulation

The human knee joint is commonly simplified as a single degree-of-freedom (DOF) hinge joint. We refer to this major rotation of the knee as flexion/extension. Other rotations of the knee include internal-external rotation and varus-valgus. These rotations are generally considered small, enabling the simplification of the knee as a hinge joint.

An IMU can be placed both distal and proximal to the knee joint, such that all relative motions between the IMUs are assumed to be due to knee flexion/extension at the joint. Small errors due to other motion of the knee or skin tissue artifacts are not modeled in this work. No assumption of alignment of the IMUs are made; the IMUs are free to be placed in any orientation on the thigh and shank, simply provided that one is distal and one is proximal to the knee joint.

The coordinate frame of the IMU on the thigh will be referred to as frame **A**, and likewise, the frame of the IMU on the shank will be referred to as frame **B**. The flex-

ion/extension axis of the knee will be referred to as axis $\vec{\mathbf{a}}$. As such, the anatomical axis $\vec{\mathbf{a}}$ expressed in frame $\mathbf{B}$ will be noted as $\vec{\mathbf{a}}^{\mathbf{B}}$. It can likewise be expressed in frame $\mathbf{A}$ as $\vec{\mathbf{a}}^{\mathbf{A}}$.

The relative angular velocity between the two IMUs can be expressed in frame $\mathbf{B}$ as:

$$\vec{\omega}^{\mathbf{B}}_{rel} = -\vec{\omega}^{\mathbf{B}}_{thigh} + \vec{\omega}^{\mathbf{B}}_{shank} = -\mathbf{D}^{\mathbf{B}}_{\mathbf{A}}\vec{\omega}^{\mathbf{A}}_{thigh} + \vec{\omega}^{\mathbf{B}}_{shank} \tag{2.1}$$

The rotation matrix $\mathbf{D}^{\mathbf{B}}_{\mathbf{A}}$ can be computed for every sample measurement k via simple rotation mathematics from the filtered orientation estimates of the individual IMUs. Multiple state estimators exist for the IMU sensor fusion for orientation problem [161, 162, 118, 207]. In this work, an unscented Kalman filter, as implemented by the manufacturer of the IMU, was used to estimate IMU orientation.

In the case of a simple 1DOF hinge system with IMUs on either side of the joint, and a low-error measurement system (e.g., low-error gyroscopes and low-error state estimates of the IMU orientations, $\mathbf{D}^{\mathbf{Global}}_{\mathbf{A}}$ and $\mathbf{D}^{\mathbf{Global}}_{\mathbf{B}}$), the relative angular velocity vector between two IMUs, $\vec{\omega}^{\mathbf{B}}_{rel}$, will point in the direction of the hinge axis of rotation. In practice, this remains true, with some (ideally small) errors in the direction of $\vec{\omega}^{\mathbf{B}}_{rel}$ due to imperfect IMU orientation estimations and small perturbations of the IMUs on the skin surface due to deformable skin tissue artifacts. We assume that the knee anatomical axis is time-invariant, being fixed in time in both IMU coordinate systems. This assumption is consistent with biomechanical modeling techniques such as OpenSim. This assumption can be violated by off-axis rotations. In practice, these off-axis rotations can be considered a combination of unmodeled knee rotations (varus-valgus and internal-external rotation) and errors, namely IMU perturbations due to skin tissue artifacts.

A robust and computationally-efficient method to produce a best single estimate of the axis of rotation, $\vec{\mathbf{a}}^{\mathbf{B}}$ is through PCA. Operationally, the principle component of a PCA on a set of vectors will find the axis which minimizes the sum of the square errors of the orthogonal distances of individual vector measurements to the estimated principle axis. Since the set of vectors $\vec{\omega}^{\mathbf{B}}_{rel}$ will generally point in the direction of the knee hinge axis (with

some noise), PCA may yield a robust estimate of the anatomical knee hinge axis $\vec{\mathbf{a}}^{\mathbf{B}}$.

Note that this method could also be expressed in terms of frame **A**. Equation 2.1 could be written in terms of frame **A** to yield $\vec{\omega}_{rel}^{\mathbf{A}}$, and PCA performed on $\vec{\omega}_{rel}^{\mathbf{A}}$ to yield an estimate of the knee hinge axis in terms of frame **A**, $\vec{\mathbf{a}}^{\mathbf{A}}$. This approach is equivalent—the axes are related by the relative orientation as $\vec{\mathbf{a}}^{\mathbf{A}} = \mathbf{D}_{\mathbf{B}}^{\mathbf{A}}\vec{\mathbf{a}}^{\mathbf{B}}$. This work will estimate the knee axis and angle in frame **B**.

A further advantage of PCA to solve this axis estimation problem is the robustness to sign ambiguity of relative angular velocity, which yields a sign ambiguity of the knee hinge axis. In flexion, the relative angular velocity $\vec{\omega}_{rel}^{\mathbf{B}}$ will point in one direction, and in extension, $\vec{\omega}_{rel}^{\mathbf{B}}$ will point in the opposite direction. Optimization or axis search methods may be confounded by this axis sign ambiguity. Since PCA only seeks to minimize the orthogonal distances of the measurements $\vec{\omega}_{rel}^{\mathbf{B}}$ to a line estimate, it does not suffer from sign ambiguity.

Once the knee hinge axis $\vec{\mathbf{a}}$ has been estimated via PCA, the knee's anatomical angles must be computed. This work implements an angle calculation method functionally similar to Laidig et al. [106] and Seel et al. [170]. A local leg segment coordinate system is defined as $\mathbf{S_1}$ and $\mathbf{S_2}$ for the thigh and shank leg segments. These coordinate systems are the IMU frames **A** and **B** rotated such that the z-axis aligns with the estimated knee hinge axis $\vec{\mathbf{a}}^{\mathbf{A}}$ or $\vec{\mathbf{a}}^{\mathbf{B}}$. For the purposes of flexion/extension calculation *only*, this segment frame can be related to the local IMU frame as a function of only estimated knee hinge axis as:

$$\mathbf{D}_{\mathbf{S_1}}^{\mathbf{A}} = [a \quad b \quad c] \quad \text{where column vectors} \quad c = \vec{\mathbf{a}}^{\mathbf{A}}, \quad b = \frac{\vec{\mathbf{a}}^{\mathbf{A}} \times [1\ 0\ 0]^T}{\left\| \vec{\mathbf{a}}^{\mathbf{A}} \times [1\ 0\ 0]^T \right\|_2}, \quad a = (b \times c) \tag{2.2}$$

for the thigh segment, and similarly for the shank segment. This relationship can be deduced by setting the z-axis to $\vec{\mathbf{a}}^{\mathbf{A}}$, the initial x-axis to [1 0 0], and then constructing an orthonormal y and x axis. The relative orientation between these new frames $\mathbf{S_1}$ and $\mathbf{S_2}$

can then be calculated as:

$$\mathbf{D}_{\mathbf{S_1}}^{\mathbf{S_2}} = \left(\mathbf{D}_{\mathbf{S_2}}^{\mathbf{B}}\right)^{-1} \mathbf{D}_{\mathbf{G}}^{\mathbf{B}} \left(\mathbf{D}_{\mathbf{G}}^{\mathbf{A}}\right)^{-1} \mathbf{D}_{\mathbf{S_1}}^{\mathbf{A}} \tag{2.3}$$

where **G** is the common global frame. Finally the relative orientation $\mathbf{D}_{\mathbf{S_1}}^{\mathbf{S_2}}$ is then decomposed into Z-X-Y Euler angles. The first Euler angle, about the Z-axis, is the knee flexion/extension angle, consistent with ISB JCS recommendations [75].

2.4 Materials and Methods

2.4.1 Participants

15 subjects (7 male, 8 female, age=20.7 $\pm$ 1.79 years) participated in the study. The protocol was approved by the Committee on the Use of Humans as Experimental Subjects at MIT. Exclusion criteria included (1) atypical neurological, heart, lung, or blood conditions, (2) surgeries performed within the previous six months, and (3) physical limitations which would require an assistive device.

2.4.2 Study Protocol

Each participant in the study completed three motion tasks: a 10-meter-walking task (10MWT), a Standing Balance task (SBT), and a Timed-Up-And-Go task (TUGT). Only the data from the TUGT was considered for this analysis. The TUGT began with the subject sitting on a stool. Then, the subject walked 3 meters to a marker, turning around it, walking back to and sitting on the stool. Each participant completed 15 TUGT trials. The first five were practice trials, meant to teach the task, and the results were not processed for this analysis. The data from the final 10 TUGT trials that each participant completed were used for analysis. Each of the 15 subjects completed these 10 full trials, for 150 trials total. Four

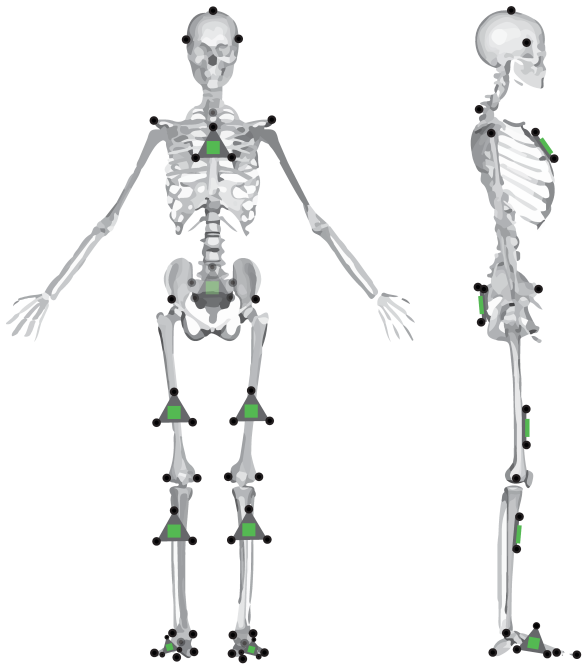

Figure 2-1: Placement of the reflective markers (black circles) and IMUs (green) on the subject. IMUs on the thigh and shank were not placed precisely, and location varied in the transverse plane.

of the recorded trials were excluded due to missing or incomplete IMU data. Three trials were excluded due to poor/diverging IMU orientation estimates from the manufacturer's onboard filter. This left 143 trials for analysis. The existence of poor IMU orientation estimates motivated the additional creation of a "simulated" set of IMU data from marker triads which had been placed on the IMUs.

Each subject was outfitted with a set of reflective motion capture markers and strap-on IMUs (Opal IMU, APDM, Inc. Portland, OR, USA). The position of these reflective markers and IMUs can be seen in Figure 2-1. As can be seen in the figure, some markers are placed on anatomical landmarks, independent of IMU positioning. These primary markers are placed according to a modified Cleveland Clinic lower body marker set for use in OpenSim inverse kinematic modeling. The position of the reflective markers was captured using

a 14-camera Vicon motion capture system (Vicon Motion Systems, Inc., Los Angeles, CA, USA) at a sampling rate of 100 Hz.

2.4.3 Data Processing

The IMU contains dual 3-axis accelerometers ($\pm$ 16g, $\pm$ 200g), a 3-axis gyroscope ($\pm$ 2000 deg/s), and a 3-axis magnetometer ($\pm$ 8 Gauss). The raw data from those sensors were fused for orientation using an unscented Kalman filter, as implemented by the manufacturer. The orientations from the two respective IMUs to a common global frame were used with the PCA method as described in Section 2.3 to estimate the knee hinge axis $\vec{\mathbf{a}}$ in each IMU frame. Then, the segment frames $\mathbf{S_1}$ and $\mathbf{S_2}$ were constructed from Eq. 2.2. Finally, the relative segment frame orientation $\mathbf{D}_{\mathbf{S_1}}^{\mathbf{S_2}}$ is computed from Eq. 2.3, which encodes the estimated knee flexion/extension angle.

The optical motion capture marker data were low-pass filtered with a 30 Hz, 6th order Butterworth filter and then processed in OpenSim, with inverse kinematics computed via OpenSim's gait 2392 model [56]. This solver minimizes error between the assumed placement of markers relative to an ideal biomechanical model (scaled for each subject) and the measured marker position from optical motion capture. The OpenSim subject model was acquired by scaling the generic OpenSim model for each subject, according to anthropometric measurements derived from the subjects' marker data while static.

The IMU data were collected at 128 Hz, while the Vicon data were collected at 100 Hz. For discrete comparison of the datasets, the IMU-based knee angle estimates were downsampled to 100 Hz. The root-mean-square-error (RMSE) of the knee angle was calculated between the OpenSim-estimated truth data and the proposed method as:

$$\delta = \theta_{OpenSim,k} - \theta_{estimated,k} \tag{2.4a}$$

$$RMSE_{absolute} = \sqrt{\frac{1}{N}\sum_{k=1}^{N}\delta^2} \tag{2.4b}$$

$$RMSE_{zero-mean} = \sqrt{\frac{1}{N}\sum_{k=1}^{N}(\delta - mean(\delta))^2} \tag{2.4c}$$

where N is the number of data points included in the calculation. The absolute RMSE, Eq. 2.4b, is the traditional calculation of RMSE. Any static offsets between the data being compared would manifest itself in absolute RMSE. However, it was found in the present study that there were static offsets between the OpenSim knee angle and the estimated knee angle from the IMUs. There are two primary sources of this static offset error: (1) human error in marker placement on anatomical landmarks and (2) the thigh and shank IMUs not lying in a plane perfectly parallel to the underlying OpenSim model bone segments. For the former, error in marker placement of the ASIS/PSIS, knee, and ankle markers would set a different angle datum when the rigid body angle between the markers is calculated and could influence the optimized OpenSim inverse kinematics solution. The latter source of error is due to the IMU not lying "flat" on the leg segment. If the thigh IMU is canted, for example, due to the shape of the quadriceps, the rigid body angle datum between the IMUs would be affected and would create a static offset from the assumed biomechanics model. In order to better understand the error of the proposed method without being confounded by the two aforementioned sources of static offset error, we also present zero-mean RMSE in Eq. 2.4c. This equation is similar to normal RMSE but the static offset between signals has been removed by subtracting the mean of the residuals from the residual data. This formulation permits a better comparison between the underlying waveforms.

For each trial, time-series measurements were compared: the ground-truth knee flexion/extension angle according to OpenSim inverse kinematics and the proposed method formulated in frame **B**. An example of these data can be seen in Figure 2-2. The IMUs and Vicon system were synchronized in time using an external trigger for subjects 9 and 11-15.

For all other subjects, the IMU-estimated knee angle and OpenSim-modeled knee angle were synchronized in time via cross-correlation. For purposes of bounding the beginning and end of the trial for IMU data, the trial was defined to begin when the marker on top of the subject's head first reached 300 mm/s vertical velocity, indicating that the subject was in the process of standing. Likewise, the trial was defined to end when the subject finally attained 300 mm/s of downward velocity for the same marker, indicating that the subject was in the process of sitting. This parameter was found from empirical tuning to work for all subjects, and included very minimal non-gait motion.

Finally, it is noted that IMU orientation estimate is imperfect, especially in indoor settings. Erroneous orientation estimates of the IMU will induce error into the IMU-estimated knee angle—an error which is not due to the proposed method. In order to control for this error, IMU data was also simulated using the marker triads on the IMUs shown in Figure 2-1. As the proposed method is agnostic to the alignment of the coordinate systems to the leg segment, the simulated IMU coordinate system can be constructed from the marker triad in any orientation. The relative orientation between the marker triad coordinate system and the Vicon global frame can then be determined. From the simulated IMU orientation and the Vicon sampling rate, the discrete angular velocity was determined. This orientation and angular velocity was then used in the proposed method just as measured IMU angular velocity and estimated orientation would be. An example of the knee angle from this simulated IMU data with the proposed method is also included in Figure 2-2.

2.4.4 Measures Collected

It was previously hypothesized in Section 2.2 hypothesis 2 that IMU location and soft tissue noise may affect the accuracy of the method. This is motivated by the amount of soft tissue artifacts–fat tissue and muscle contraction–of the leg seeming to vary across the lateral-to-anterior surface. Due to the contraction of the quadriceps, we postulate that an

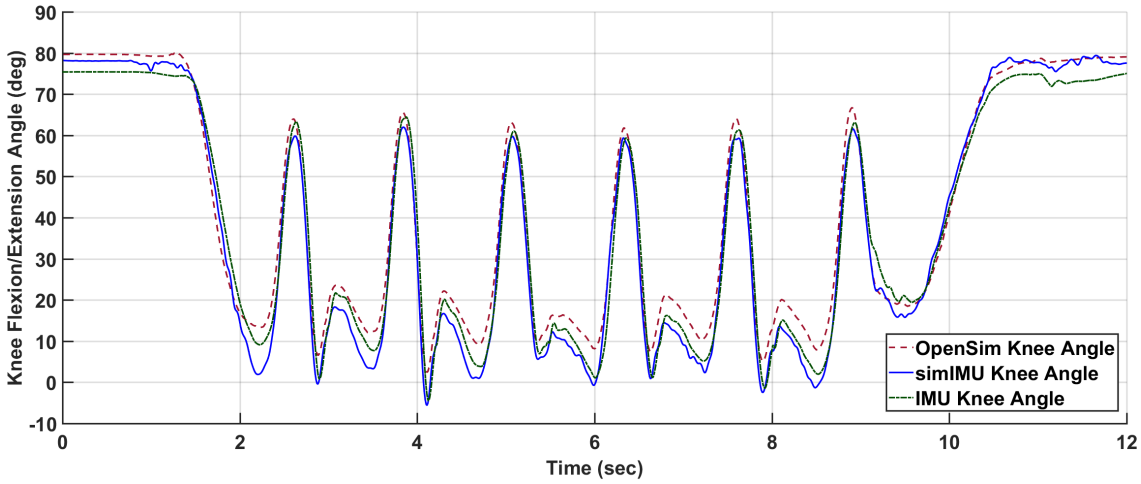

Figure 2-2: Example absolute knee angle data, shown for subject Y2, TUGT trial 6. Shown are the measured IMU data (IMU, absolute RMSE=3.93°, zero-mean RMSE=2.72°) and simulated IMU data from the marker triads (simIMU, absolute RMSE=5.87°, zero-mean RMSE=2.97°) against the OpenSim knee angle truth.

IMU on the anterior surface would experience more perturbation relative to the underlying bone structure than an IMU on the lateral surface of the thigh. This relative motion violates the rigid body assumption of the method.

In order to analyze this hypothesis, the circumferential placement of the IMU was defined as the angle between the IMU normal vector and the lateral direction of the leg segment, measured in the transverse plane normal to the body segment (Figure 2-3). The transverse plane of the body segment is defined as mutually orthogonal to the sagittal and coronal planes. The coronal plane of the thigh is defined as the plane which contains the medial and lateral knee markers and the hip joint center, calculated by relationships to pelvic anthropometry as suggested by Seidel et al. [173]. The coronal plane of the shank contains the two knee markers and the centerpoint of the medial and lateral ankle markers. The sagittal planes of both leg segments are defined as the plane whose normal runs through both knee markers. The circumferential angle α of the IMU is then defined as the angle between the lateral-pointing vector of the body segment in the transverse plane,

and the IMU normal vector projected into the transverse plane. The circumferential angle for the thigh IMU would be calculated as:

$$\alpha_T = \texttt{atan2}(\|\vec{\mathbf{a}}^{\mathbf{A}} \times \vec{A}\|, \vec{\mathbf{a}}^{\mathbf{A}} \cdot \vec{A}) \tag{2.5}$$

and similarly for the shank IMU, where $\vec{A}$ represents the projection of the thigh IMU normal vector into the transverse plane. For example, an IMU placed perfectly on the lateral surface of a body segment would be at $\alpha = 0°$, whereas an IMU placed perfectly on the anterior surface of the thigh or shank would be at $\alpha = 90°$. Note that for the calculation of α in this study, the IMU marker triads were used to define the IMU normal vector, and the knee hinge axis $\vec{\mathbf{a}}$ was determined from the medial and lateral knee markers.

The circumferential angle was computed as a function of time for every trial. It was found that the angle varied significantly over the course of the trial (Figure 2-4). The general position of the IMUs on the leg segment were quantified as the mean of the circumferential angle over time, and the standard deviation is used as an analog for the amount of motion relative to the rigid body bone structure that the IMU experienced. The mean and standard deviation of the circumferential angle will be denoted as $\overline{\alpha_T}$ and σ_{α_T}, respectively, for the thigh. Likewise, the circumferential angle measures for the shank are denoted as $\overline{\alpha_S}$ and σ_{α_S}.

It was further hypothesized that subjects with more fatty tissue would induce more perturbations to the IMU, and thus more error. While measures of subject BMI were not collected in this study, the ratio of a subject's thigh width-to-length was used as a surrogate measure. For each subject, this measure will be denoted as W/L_{thigh}.

Finally, it was hypothesized that with poor knee axis estimation comes poor knee angle estimation. Within a trial, the simulated IMU-estimated knee axis was compared with the knee axis as defined by the medial and lateral knee markers. The median of this axis estimation error was also used as a predictor for knee angle error, denoted as ϵ_{axis}.

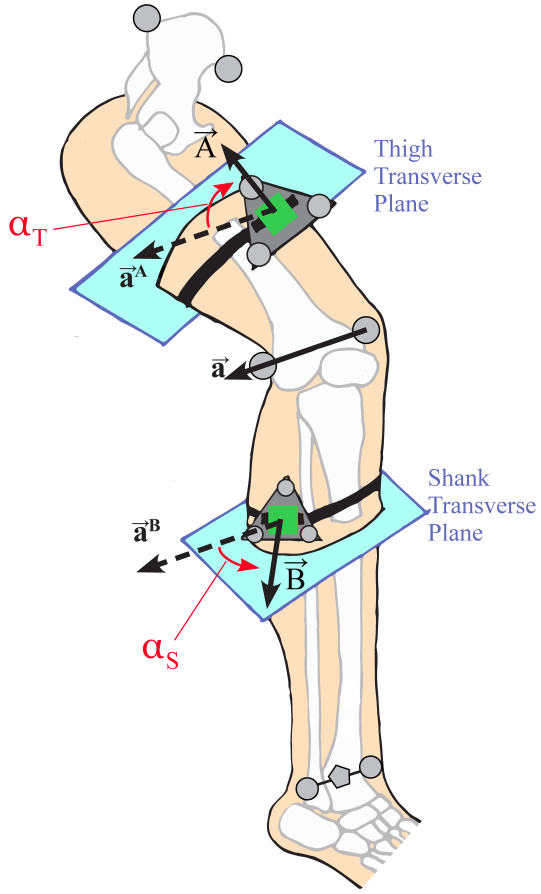

Figure 2-3: Illustration of the circumferential angle of the IMU (green) on the thigh (α_T) and shank (α_S). The knee axis $\vec{\mathbf{a}}$ and its representation in the transverse planes of the thigh and shank are also shown. The pentagonal markers between the medial/lateral ankle markers and ASIS/PSIS markers represent the virtual marker which was used with the two knee markers to define the coronal plane of each leg segment. $\vec{\mathbf{A}}$ and $\vec{\mathbf{B}}$ represent the projection of the IMU normal vectors into the transverse planes of the thigh and shank, respectively.

2.4.5 Statistical Analysis

Data were analyzed for global results via the Bland-Altman method [138, 23], a statistical method to evaluate the agreement of two multi-sample measurements. Beyond

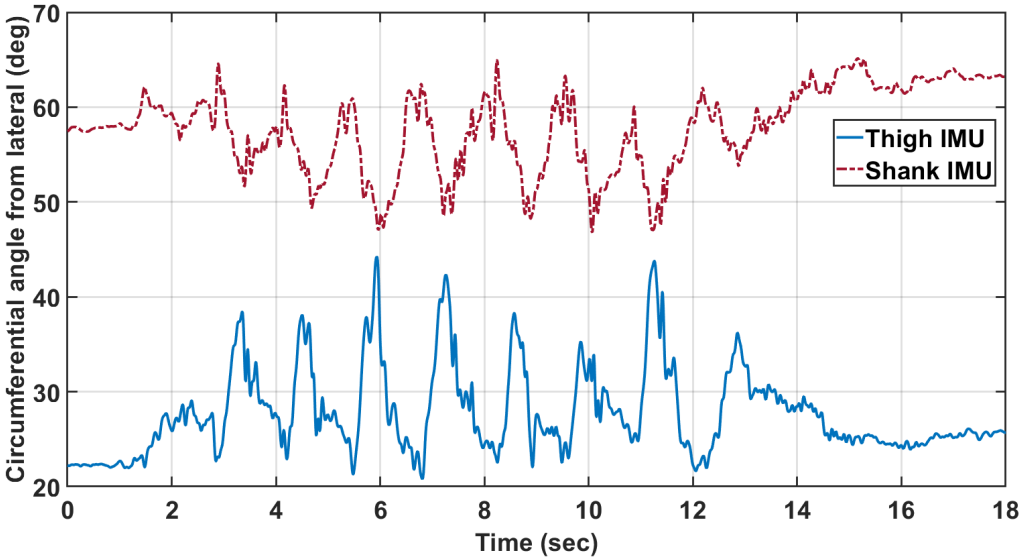

Figure 2-4: The circumferential angles of the IMU placement on the thigh ($\overline{\alpha_T} = 26.6°$, $\sigma_{\alpha_T} = 4.6°$) and shank ($\overline{\alpha_S} = 57.8°$, $\sigma_{\alpha_S} = 4.3°$) for Subject Y1 TUGT trial 6

the overall estimation of error RMSE, Bland-Altman analysis can enable inferences about the linearity of the residuals over the measurement domain. Bland-Altman analysis is usually represented in two plots, the first of the two plots will show a linear regression of the simulated IMU-estimated knee angle vs. the OpenSim-modeled motion capture knee angle. These would be ideally linearly correlated with a unity slope. The second plot will show the difference between measurements on the vertical axis and the average of the two measurements on the horizontal axis. These deviations would ideally have zero mean and a low variance.

All of the knee angles according to OpenSim and the proposed method with simulated IMU data were concatenated for error calculation and Bland-Altman analysis to create a composite assessment of all subjects. Measurement error over the entire study will be reported in terms of overall RMSE, r^2 linearity coefficient, static bias of the measurement error with probability of that bias being non-zero, and 95% confidence interval of the error.

A post-hoc linear mixed effects model was constructed to investigate factors which contribute to RMSE, here we specifically consider the zero-mean RMSE of the simulated IMU method as this model would highlight the effects of the factors on the PCA methodology. RMSE per trial was modeled as a linear function of the aforementioned fixed-effect factors: circumferential angle mean and standard deviation for the thigh and shank, thigh-width-to-length ratio, and estimated axis error, along with relevant interaction effects. As the trials within a subject are not independent, subject is included as a random effect, modeled as a random intercept. Factors which did not have a nearly-significant main effect or interaction effect were then removed from the model. This reduced model is presented in the results section. When fitting the model, fixed factors were removed from the model if the estimated slopes of the interaction and main effect were not significant at $\alpha = 0.1$; however, for interpretation, we consider significance as $\alpha = 0.05$. These factors were removed to prevent overfitting of the model.

2.5 Results and Discussion

2.5.1 Overall Performance

Analysis of the simulated IMU data through the proposed method formulated in frame **B** showed an absolute RMSE of 9.72° and a zero-mean RMSE of 3.49°. Bland-Altman analysis of the total experiment (using the absolute simulated IMU data) in Figure 2-5a shows a linearity of r^2=0.80 to the best-fit model $y = 1.04x - 0.32$, a 95% confidence interval of the error on [+20,-18] degrees, and an average static bias offset of 0.63° ($p < 0.001$). There was high variability between subjects, for example subject Y2 in 2-5b with r^2=0.98, [+2.5°,-10°] confidence interval, -3.8° average offset ($p < 0.001$), and subject Y4 in 2-5c with r^2=0.88, [+9.7°,-16°] confidence interval, and -3.0° average offset ($p < 0.001$).

For comparison, the Seel et al. [170] axis estimation method was also implemented with

the angle calculation approach described in Section 2.3. The RMSE of the proposed method by subject is shown in Table 2.1. The difference in results between the proposed method on the simulated IMU data and the measured IMU data with the manufacturer's onboard orientation estimator shows that there was significant error in the IMU's orientation estimation in the lab environment. Likewise, the difference between the absolute RMSE and the zero-mean RMSE of the proposed method on the simulated IMU data suggests some disagreement between the knee angle datums of the OpenSim-estimated knee angle and the IMU-based knee angle. These analyses suggest a good level of agreement between the proposed method and the OpenSim-modeled optical motion capture measurement method. As compared to a traditional motion capture system, this method can be implemented in the field, rather than being constrained to a laboratory environment. Likewise, as compared to traditional IMU-based joint angle measurement approaches, this method assumes no alignment of the IMU to a limb segment. As a result, this method would be easier and faster to implement for both researchers and non-experts alike. The accuracy of the proposed system is similar to that of previous literature [65, 122], without the need to align the system to body segments or perform a prior calibration. There was some variation in the quality of this knee angle estimation between subjects, as illustrated in Figure 2-5 and Table 2.1.

Bland-Altman analysis on some individual subjects may also suggest a nonlinearity at the low end of the measurement domain, corresponding to near-full extension of the knee. It seemed that the measurement system captured the knee angle well throughout much of gait, but at full extension the "true" measurement and the IMU measurement do not agree well (see Figure 2-5b,2-5c). Generally, error in knee angle estimation can be attributed to the violation of the method's basic assumption: that the knee hinge axis is time-invariant and can be represented statically in both IMU frames. A few different factors may contribute the violation of this assumption, namely, (1) that the knee flexion/extension axis is not a perfectly time-invariant hinge, and (2) perturbations to the IMUs can cause artificial

Subject	$RMSE_0$**(simIMU)**	$RMSE_0$**(IMU)**	$RMSE_0$**(simSeel)**	absolute $RMSE$**(simIMU)**
1	2.33	4.06	2.96	16.8
2	2.99	2.60	3.68	4.96
3	2.91	6.00	7.23	6.45
4	4.86	3.60	5.20	7.14
5	4.75	8.63	6.56	9.04
6	2.90	2.74	6.02	3.40
7	2.48	5.67	6.44	14.36
8	2.77	13.1	7.70	7.31
9	3.56	6.37	9.88	11.75
10	3.39	9.94	4.50	16.06
11	3.79	11.24	6.65	4.07
12	3.89	17.02	7.52	7.70
13	3.46	13.74	7.04	5.68
14	3.58	5.78	4.48	8.52
15	4.27	14.78	8.00	6.10
Total	3.49	9.21	6.43	9.72

Table 2.1: RMSE in degrees by subject for selected analyses: zero-mean RMSE of the simulated IMU knee angle with the proposed method, zero-mean RMSE of the actual IMU data with the proposed method, zero-mean RMSE of the Seel et al. method [170] on the simulated IMU data, and absolute RMSE of the simulated IMU data with the proposed method.

movement of the IMU frame, thus causing the static estimate of the knee axis to deviate from the true axis. These perturbations of the IMUs could be due, for example, to soft tissue artifacts on the leg. Near full-extension of the knee, the quadriceps contract and cause the anterior surface of the thigh to expand. An IMU on the surface of the thigh would likewise bulge. Furthermore, near full-extension of the knee the foot contacts the ground in gait, possibly causing vibrations in the tissue of the leg which would transfer to the IMU. The following section investigates the effect of IMU perturbation, axis estimation accuracy, and subject anthropometry on the knee angle estimation error.

The Favre et al. [63] IMU measurement system estimated knee flexion/extension angle to an accuracy of 1.5° mean RMSE after a calibration procedure including a static pose and prescribed hip abduction motion. The Seel et al. [170] auto-calibrating IMU measurement system reported an error of 3.3° RMSE for a single subject performing six gait trials. The present findings suggest that evaluation of wearable IMU methods on larger subject populations is important for method characterization. This work extends the existing literature by evaluating an auto-calibrating knee IMU-based measurement system on a larger subject set, studying the operational predictors to error in an auto-calibrating measurement system, and the proposal and implementation of a computationally-inexpensive algorithm which is robust to sign-ambiguity problems common to most axis estimation approaches. The variability in error across subjects underscores the importance of testing wearable IMU methods with larger subject populations.

2.5.2 Explanatory Model

Measures collected to test the hypothesis 2 of Section 2.2 are described in Section 2.4.4. These measures were used as fixed-effects in a linear mixed effects model to predict zero-mean RMSE of the simulated IMU data with the proposed method within a trial. Appropriate two-way interaction terms were included. Subject was also included as a random effect. The results of the reduced linear model are shown in Table 2.2. The overall

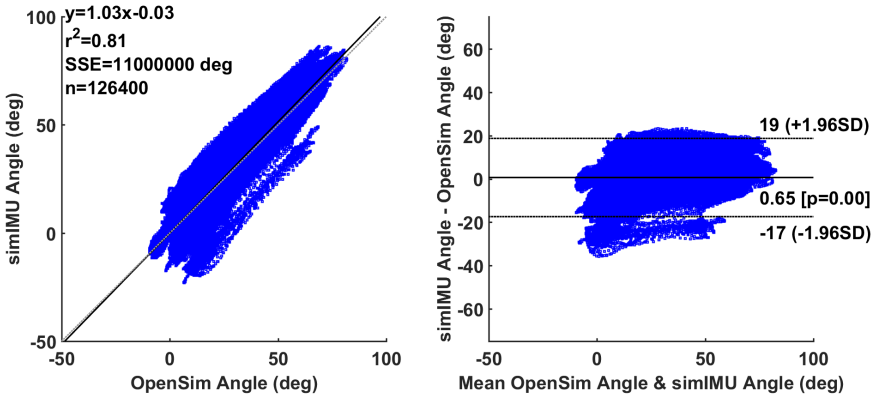

(a) Total experiment, all subjects

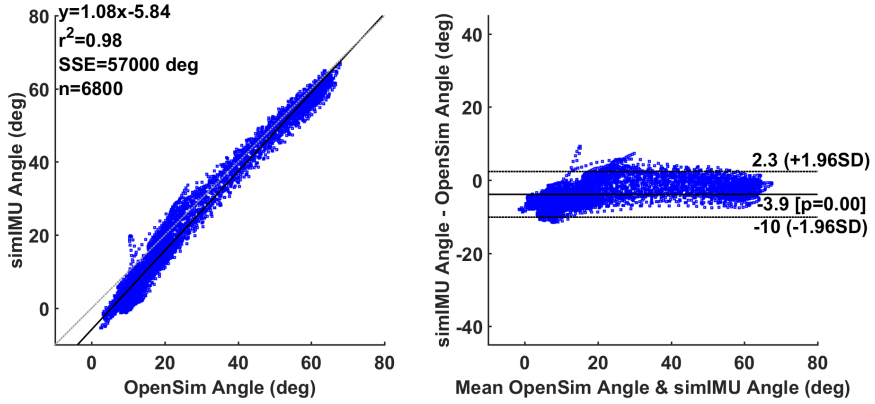

(b) Subject 2

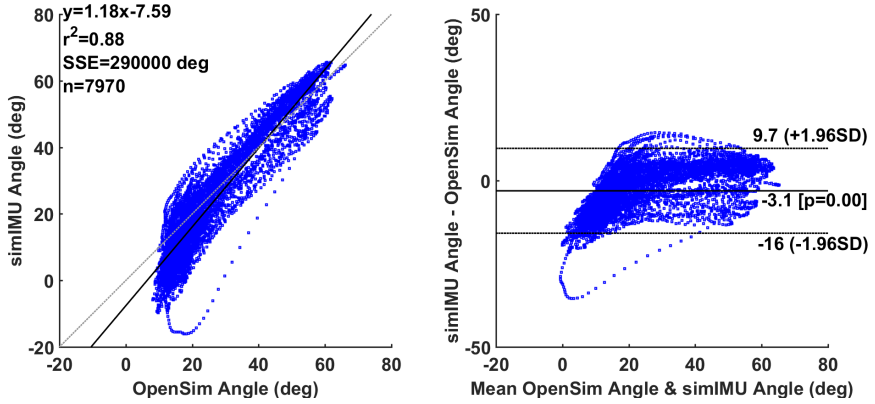

(c) Subject 4

Figure 2-5: Selected Bland-Altman analyses; linear model given by $y(x)$ with associated squared correlation coefficient r^2, including sum of squared error (SSE) over n data points. Estimated data is the knee angle according to the proposed method on the simulated IMU data.

Term	Estimate	SE	t	p
Constant	4.723	0.546	8.651	< 0.001
σ_{α_T}	-0.235	0.083	-2.830	0.005
ϵ_{axis}	-0.126	0.042	-3.040	0.002
$\sigma_{\alpha_T} \times \epsilon_{axis}$	0.023	0.007	3.472	< 0.001

Table 2.2: All terms in the reduced linear model. Significant parameters included thigh circumferential angle standard deviation (σ_{α_T}), median axis estimation error (ϵ_{axis}), and the interaction between the two. Estimate is the estimated coefficient for the predictor variable (intercept or slope coefficient), SE is the standard error of the estimate, t is the associated t-statistic of the coefficient against the null hypothesis of a zero value, p is the p-value associated with the t-statistic. Significance was set as $p < 0.05$.

model adjusted $R^2 = 0.85$ suggests a good linear fit, to a total significance of $p = 0.004$ ($F(3, 139) = 4.62$).

While the main effects of the model suggest a significance of σ_{α_T} and ϵ_{axis} to the linear model predicting zero-mean RMSE of the proposed method on the simulated IMU data, the interaction effect dominates the main effect. The interaction of σ_{α_T} to ϵ_{axis} lends that there is a larger increase in RMSE with more σ_{α_T} when the axis is poorly estimated, i.e., good axis estimation makes the method more robust to increased σ_{α_T}. However, the effect size is clearly small. Researchers can probably gain more in the way of method accuracy through improving IMU orientation estimation rather than specific sensor placement. These results corroborate those of Graurock et al. [74] who found little operational difference between sensor placements on the thigh. However, they do still recommend placing the sensors on the lateral side of the thigh. The model is shown in Figure 2-6.

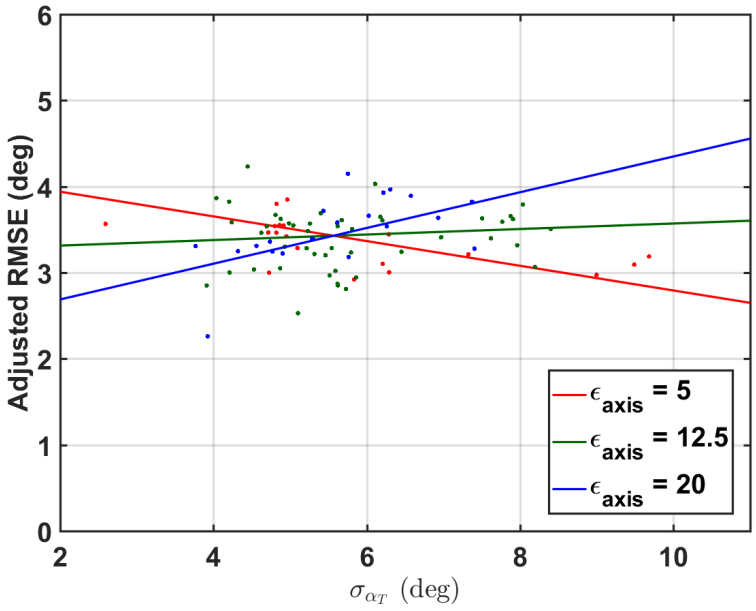

Figure 2-6: The linear model, plotted as a function of σ_{α_T} and ϵ_{axis}. The points selected have been adjusted by the estimated subject intercept (random effect) so that multiple subjects can be presented with the same linear regression lines (plotted using only the fixed effects and Constant). The points selected for each line were those that had $\epsilon_{axis} \pm 2.5^\circ$ about the selected value.

2.5.3 Future Work and Limitations

Future work will seek to implement a filter-based estimator for the knee hinge axis and angle, allowing the axis to be estimated over time in a statistically-robust manner. Furthermore, as the estimated knee angle seems to deviate from truth near the extremes of the knee flexion/extension domain, the measurement error may be able to be reduced by modeling the error as a possibly nonlinear function of measured knee angle. Finally, the knee hinge axis is not perfectly fixed; relaxing this assumption to estimate the time-variant knee hinge axis may also reduce measurement error.

The predictors of the linear model were not varied as factors in the observational experiment; rather, they were measured post-hoc to build the explanatory model, leading

to a limited region of the parameter space for which the model is appropriate. While this analysis considers a reasonable domain, follow-on factorial studies could explore error dependence over a wider parameter space. A future experiment could experimentally vary these factors and take proper body fat measures to more robustly understand the factors affecting the error of the proposed method. Furthermore, in this model axis error was quantified as the difference between method-estimated knee hinge axis and the knee axis as defined by the medial and lateral knee markers. There is the potential for small shifts in marker placement, which would affect these results.

It should be noted that the proposed method requires orientation estimation of two IMUs to a common global frame. In practice, there are always some errors associated with orientation estimation. Some errors in this process could be due to estimating IMU orientation relative to slightly different world frames. Methods have been proposed to remedy this problem [190, 106]. The Seel et al. [170] method does not require orientation estimation to estimate the knee hinge axis or flexion/extension angle, which could prove advantageous in high-orientation-estimation error situations. While this work relied on the onboard orientation estimation algorithm from the manufacturer, this method could be employed with any orientation estimation technique. Further estimation methods have been proposed [171] to aid in the general problem of magnetometer fusion in the presence of variable magnetic fields (i.e., many indoor scenarios). The proposed PCA method shows promise with accurate IMU orientation estimation. Finally, the presented angle decomposition method is only appropriate for calculation of knee flexion/extension angle due to selection of an arbitrary x-axis. Interpretation of the other rotations as meaningful knee angles would require estimation of the other rotation axes of the knee.

Comparison of this method to an OpenSim truth also required understanding of the biomechanical datum for knee flexion/extension angle present in both the OpenSim knee angle and the IMU-estimated knee angle. These datums may be different due to small shifts in marker placement on the subject or IMU placement such that the IMUs do not align with

the underlying biomechanical model of the leg segment. This limitation motivated the reporting of RMSE as both the absolute RMSE and zero-mean RMSE. The zero-mean RMSE is a better comparison of the difference between true and estimated knee angle waveforms, while the absolute RMSE would include this difference and also static offset errors due to different datums between the OpenSim knee angle and estimated knee angle.

2.6 Conclusion

A method has been developed for the estimation of the knee flexion/extension angle using inertial sensors. This method allows for estimation of the angle without cumbersome alignments of the IMUs to the leg segments, as the system calibrates itself from any general hinge motion of the knee. The knee's major rotation axis is estimated through the use of PCA, a computationally-efficient and simple algorithm that can be implemented online which is robust to the positive/negative sign ambiguity of the estimated knee axis. When pooling all subjects, the method performed with absolute RMSE of 9.72° and a zero-mean RMSE of 3.49° as compared to an optical motion capture gold standard, although subjects ranged between 2.33° and 4.86° zero-mean RMSE. Unlike previous literature, the method is evaluated over a larger population (15 subjects), and variability in RMSE across subjects was found.

In addition, an explanatory model of the error has been presented. The model suggests that method error is a function of thigh IMU circumferential motion and quality of knee flexion/extension hinge axis estimation—highlighting the importance of axis estimation to calculation of knee angle. However, the effect size for these parameters is small in comparison to potential gains from improved IMU orientation estimations. Furthermore, the results underscore the importance of understanding and setting appropriate datums when comparing two differently-measured data series.

Chapter 3

Body-Worn IMU Human Skeletal Pose Estimation using a Factor Graph Based Optimization Framework

This chapter presents a 7-IMU lower body kinematics estimation system which makes no assumption of placement of the IMUs on each limb segment. Chapter 2 detailed the development (Sec. 2.3) of a novel kinematic model of the human knee. While in Chapter 2 the knee axis estimation problem was cast for solution via PCA, in this chapter the model is cast for least-squares optimization. Additionally, this chapter includes a number of other novel kinematic model aspects, including various aspects of human anthropometry. This problem is formulated without the use of magnetometers as an IMU heading reference. A review of relevant literature is presented (Sec. 3.2). Then the problem is formalized as a maximum a posteriori estimation problem (Sec. 3.3). The proposed approach is validated in a multi-subject experiment (Sec. 3.4) for a treadmill walking and calibration task. Hypotheses related to (a) hip and knee angle accuracy, (b) IMU orientation estimation accuracy, and (c) IMU position estimation accuracy are evaluated.

A subset of these results and modified version of the model was published in *Sensors*: McGrath, T.; Stirling, L. Body-Worn IMU Human Skeletal Pose Estimation Using a Factor Graph-Based Optimization Framework. *Sensors* **2020**, *20*, 6887.

In the current presentation of the model and results (unlike the journal publication) an additional constraint was added to fix the joint centers at a constant point in the navigation frame *only* during calibration task processing (detailed in Sec. *Human Calibration Data Processing*). It was found that this constraint is strictly not necessary, however, it is published in this work to show original method performance.

3.1 Abstract

Traditionally, IMU-based human joint angle estimation requires a priori knowledge about sensor alignment or specific calibration motions. Further, magnetometer measurements can become unreliable indoors. Without magnetometers, however, IMUs lack a heading reference—which leads to unobservability issues. This chapter proposes a magnetometer-free estimation method, which provides desirable observability qualities while requiring no calibration under sufficient joint kinematics. In the case of insufficient kinematics (e.g., only walking), a simple calibration is used to augment the task. The proposed lower body model expands on the current self-calibrating human-IMU estimation literature and demonstrates a novel knee hinge model, inclusion of segment length anthropometry, segment cross-leg length discrepancy, and the relationship between the knee axis and femur/tibia segment. The maximum a posteriori problem is formulated as a factor graph and inference is performed via post-hoc, on-manifold global optimization. The method is evaluated (N=12) for a 30-minute treadmill walking and calibration task. Accuracy of derived joint angles without magnetometers for knee flexion/extension, hip flexion/extension, and hip abduction/adduction are similar to current state-of-the-art with magnetometer use (RMSE 3°–7°). Hip internal/external rotation accuracy is task-

dependent and subject to unobservability for certain tasks. The developed framework can be expanded for modeling additional joints and constraints.

3.2 Introduction

Estimation of the human skeletal pose is a well-studied problem [76, 112, 187]. The class of techniques referred to as human motion capture, or *mocap* for short, has been approached through different measurement technologies. While computer vision systems exist [165], the most common approach today is marker-based optical motion capture (OMC) [34]. These techniques generally involve the mounting of reflective markers on the human body which are triangulated in space using a set of specially-equipped cameras. While this approach is very accurate at localizing the position of each marker in the capture volume, additional modeling approaches (for example, OpenSim [55] or the Vicon plugin gait model [52, 88, 197, 24]) are required to infer the biomechanical quantities of interest—joint angles, skeletal position, etc. Furthermore, marker-based mocap has measurement limitations. Markers may be occluded or fall off the subject, and the measurement typically must take place in a controlled laboratory environment [66].

Small, wearable inertial measurement units (IMUs) have garnered interest as a low-cost, in-the-field alternative to OMC. These sensor packages typically measure acceleration and angular velocity, and are often augmented with local magnetic field measurements to aid in heading estimation. IMUs have classically been used for inertial navigation on aerospace and nautical systems [4, 6, 78]. Modern IMUs mounted on the human body are compact and offer motion estimation without external equipment and a line-of-sight requirement. Approaches are developed to overcome the major disadvantages of IMUs, namely system noise and drift of estimated quantities (e.g., [213, 86, 82, 83, 26, 204]). Along with developed human-body modeling approaches, IMUs have found multiple uses for human studies, including clinical sciences [139, 140, 188, 28, 73], sports performance

[141, 47, 38, 48, 191], activity recognition [202, 101, 36, 179, 18], occupational ergonomics [111], and even spacesuit fit evaluation [67].

One major consideration to be made when using IMU-based human modeling approaches is prescribing or estimating the relationship between the IMU coordinate frame on the surface of the body segment and the underlying skeletal system in which many biomechanical quantities of interest are defined, sometimes referred to as the IMU-to-segment (I2S) pose relationship. A recent review by Vitali and Perkins [192] places these methods into four distinct categories—(1) assumed alignment methods, (2) functional alignment methods, (3) model based methods, and (4) augmented data methods. Assumed alignment approaches have considered a priori alignment of the IMU to the human skeletal system [113]. Mayagoitia et al. [122] used aligned gyroscope and accelerometer packages to track pitch angle of the shank to an error of $2.7^\circ \pm 2.8^\circ$. Favre et al. [65, 64] precisely aligns one of the axes of the IMU with the knee's major rotation axis. Kok et al. [97] formulates the problem as a maximum a posteriori (MAP) estimation problem, solved through weighted least squares optimization, including estimation of the offset vectors from neighboring segment coordinate systems to their common point-revolute joint, after determining the I2S relationship from a priori measurement and a static calibration routine [157]. These methods are limited by the operator's ability to precisely align the IMU, or their ability to measure the alignment offset. Functional alignment methods have considered using static or dynamic calibrations (referred to as *functional* calibrations) which the human subject must perform in order to determine the alignment between the IMU and the skeletal system. Favre et al. [63, 62] prescribes a functional calibration set with a subsequent root mean square error (RMSE) of the knee's three major rotation angles between 4.0° and 8.1°. Many other works have also used functional calibration to aid in estimation of segment kinematics [214, 114, 145, 43, 182, 46, 190, 3]. These methods may be confounded by the subject's ability to perform the prescribed calibrations.

More recently, efforts have shifted towards overcoming these limitations of functional

or static calibrations. In this work, the phrase *self-calibrating* is used to describe model-based approaches which either (a) estimate the pose relationship between the IMU and underlying bone segment coordinate system (i.e., the I2S relationship), or (b) which can derive relevant biomechanical parameters of the human skeleton (such as joint angles) without directly estimating the I2S relationship. These approaches generally exploit kinematic relationships which exist between IMUs mounted on a semi-rigid-body about a fixed-point rotating joint. Müller et al. [137] models the elbow as a 2DOF system, and argues that the magnitude of the relative angular velocity about the joint may be decomposed into axis components through a formulated optimization problem. McGrath et al. [125] extends this argument to the 1DOF knee hinge joint, offering a computationally-efficient axis estimator based on principal component analysis (PCA). Seel et al. [172, 170] presents an optimization-based approach to estimating joint axis and position in the IMU frames from measured angular velocities and accelerations for the knee and ankle joints. This method is expanded on by Salehi et al. [164] with a modified measurement model of the IMU positions relative to their neighboring joints to aid in accuracy and observability. Taetz et al. [183] presents a similar problem solved via a sliding-window weighted least squares algorithm, but with the novel addition of assuming a topology on which the IMU is mounted. In that work, the authors assume a capsule-type shape, but note that other shapes can be included. Often, these works estimate or otherwise kinematically include (i.e., through a priori measurement) an I2S calibration parameter for each IMU [130, 97, 183], typically modeled as a static $SE(3)$ transformation between the underlying limb coordinate system and the coordinate system of the IMU on the limb surface. Other works [128, 131, 172, 170, 125, 137] seek to derive relevant biomechanical states without directly estimating the underlying skeletal coordinate systems, a potentially minimal parameterization of the problem. The current work falls in the latter category. There are two major motivations for this approach: first, as noted in Taetz et al. [183], to estimate both the IMU coordinate system trajectory and the skeletal coordinate system trajectory

(when the I2S relationship is assumed static) is a redundant variable set. Secondly, when mathematical relationships are cast as a function of skeletal coordinate system (rather than IMU coordinate system), the resultant noise distributions are often immeasurable. For example, as of this publication, the authors are not aware of attempts to measure the noise distribution of (a) bone connection "error" at a single rotation center (i.e., the constraint first proposed by Kok et al. [97] (Eq. 3) and used by subsequent works [183]) when the constraint is cast in the skeletal coordinate system or (b) the distribution of the aforementioned static I2S parameter in $SE(3)$, although efforts have been made [129] to investigate the sensitivity of the optimized solution to the accuracy of this parameter. This modeling dichotomy deserves continued investigation.

These works also vary in their solution methodology. Many consider general batch optimization [97, 172, 170, 137], while others have considered sliding window approaches [183], filtering approaches [3] or even PCA-based approaches [125]. Recently, Kok et al. [99] reconsiders the optimization problem [97] but with a more efficient approach to selection of search direction, using a message passing algorithm [148].

Performing batch optimization for this class of problems is expensive due to high-frequency data measured from multiple IMUs. Indeed, filtering-based methods exist [136] for the inertial navigation problem, however, filtering methods (e.g., the extended Kalman filter) may suffer in accuracy for highly-nonlinear problems due to the choice of linearization point. Meanwhile, it has been proposed to use *keyframes* [110] to reduce the size of the optimization problem, i.e., to select only a relevant subset of the full state trajectory for MAP inference. Depending on the application, this keyframe approach can also yield faster solutions without loss in accuracy or operational decision making ability. For example, human walking can be captured with a slower keyframe rate than sprinting, and likely neither require estimated states at the same rate as a high frequency IMU samples. Lupton and Sukkarieh [117] first proposed an implementation for inertial sensors as *preintegrated IMU measurements*. The current work relies on the implementation by Carlone

et al. [30] and Forster et al. [70]. Their IMU preintegration work develops a relative motion constraint *between* keyframes which robustly handles IMU bias propagation. Moreover, the IMU model variables, as with all relevant variables in this work, are implemented on-manifold for efficient computation (for a background on differential manifolds, Lie groups, and applications to visual/inertial/human navigation problems, the reader is referred to [194, 22, 98]). The GTSAM 4.0 library [54], which uses *factor graphs* [103] as the underlying computational framework, is a commonly-used library for on-manifold optimization and includes the IMU preintegration work.

Another consideration is that magnetometers are notoriously unreliable indoors [158, 53] due to the presence of electromagnetic disturbances. While some works have considered compensation or recalibration for these disturbances [106, 37, 100, 108], many works, including this one, avoid the use of magnetometers altogether [105, 97]. Without the use of magnetometers, IMUs typically do not have a heading reference, leaving the yaw degree of freedom generally unobservable in the case of traditional dead-reckoning for IMU pose trajectory. Therefore, exploiting kinematic constraints inherent to the human skeletal system (cast in local frames, i.e., between body segments) may improve observability [164], however, may not provide *absolute* observability of IMU heading angle, i.e., all solutions rotated about the global vertical axis are equivalent. Discerning the heading relationship between two IMUs flanking a joint may be possible using an approach which leverages a model of a static vector pair from the joint to the neighboring IMUs, e.g., [97], however, when these vectors lie normal to the horizontal plane they may not provide sufficient information. Tasks such as upright gait are likely to have static vectors from the IMU to joint centers that are directed proximal or distal on the limb, which would be approximately parallel to the global upward vector. In these situations, more information is necessary to discern the heading relationship between two IMUs. The current work presents a novel knee kinematic model for least-squares optimization which leverages the kinematic relationship between the pair of IMUs' orientations and angular velocities in

order to estimate a static rotation axis in each IMUs' local frame. In the case of upright gait and an appropriately-behaved kinematic hinge (such as the human knee), the proposed model would provide enough information to discern the heading relationship between the two IMUs flanking the joint center. The direct estimation of the hinge axis, which points medial/lateral in the skeletal frames, permits the definition of segment coordinate systems consistent with International Society of Biomechanics (ISB) recommendations [198, 75, 199]. Deriving joint angles according to ISB convention has the explicit benefit of both allowing comparison across different methods and presenting angles in a common convention that is already accepted.

In this work, we consider the problem of estimating lower body skeletal kinematics from a set of 7 IMUs mounted on the subject (on the lower back, thighs, shanks, and feet) for a standard gait task without a heading reference. It is assumed that we understand which IMU is mounted on which limb segment (although automated approaches to this problem have been considered, see [215]), but no assumption of where the IMU is mounted on the limb segment is made. The proposed optimization-based approach uses accelerometer and gyroscope measurements to estimate IMU pose trajectories, knee hinge axes statically represented in the thigh and shank IMU local frames, and the assumed-static relationship between the IMU frame and its neighboring joint center(s) subject to a number of kinematic constraints. These estimated parameters allow for post-hoc derivation of the underlying femur, tibial, and pelvic coordinate systems, and as a result, the skeletal joint angles for the knee and hip. Performance of the proposed approach is evaluated for 12 subjects, each performing a 30-minute-long walking task on a treadmill in an indoor laboratory. Additionally, the subject is outfitted with optical motion capture tracking as a truth datum. When appropriate, the proposed method is compared against a control IMU algorithm: considering each of the 7 IMUs individually as a dead-reckoning problem in an optimization-based smoothing framework.

We hypothesize (1) the proposed model will not significantly affect error of estimated

IMU orientations for the traditionally-observable orientation degrees of freedom (pitch and roll) and (2) that the derived joint angles of the human will fall within 5 degrees RMSE when compared to an optical motion capture truth datum. Additionally, this work will characterize IMU position estimation accuracy.

This work extends the literature for estimation of human limb pose estimation from body-worn IMUs in three key ways. (1) This work presents a novel knee kinematic model similar to McGrath et al. [125] but reformulated for least-squares optimization, additionally exploiting kinematic information about the relationship between the knee's rotation axis and the femur and tibia proximal direction [79]. (2) This work demonstrates inclusion of population anthropometric information as a probabilistic constraint, namely length of the femur, tibia, and femoral head separation as well as femur and tibia length discrepancy. (3) This work leverages IMU preintegration theory [30, 70] to reduce problem size and complexity without loss in accuracy or relevant estimated information. In addition to these contributions, the MAP estimation problem is presented in factor graph form, an expressive modeling framework which allows for flexible inclusion of priors and advanced inference techniques. While in the presented problem the kinematic constraints are included at each keyframe, one could easily only include the kinematic constraints at a subset of keyframes or constrain across nonconsecutive keyframes if such information existed. This work adopts recommended conventions by the ISB for reporting knee [75] and hip [199] angles to increase operational interpretation for end users, which is made possible through the estimation of the knee's rotation axis. The method is tested in a multi-subject study with differences between subjects considered.

3.3 Problem Formulation

The method requires a human subject is outfitted with IMUs on the lower back, thighs, shanks, and feet. The assignment of IMU to limb segment is known; however, the place-

ment (i.e., orientation and position) of the IMU on the segment is unknown. It is desired to estimate the time-series pose trajectories of each IMU along with a static biomechanical map which relates these IMUs to the underlying skeletal system to which they are jointly attached. No reference of position or heading angle is assumed to be known—only measurements of the accelerometer and gyroscope of each IMU are taken. A visual representation of this system is shown in Fig. 3-1.

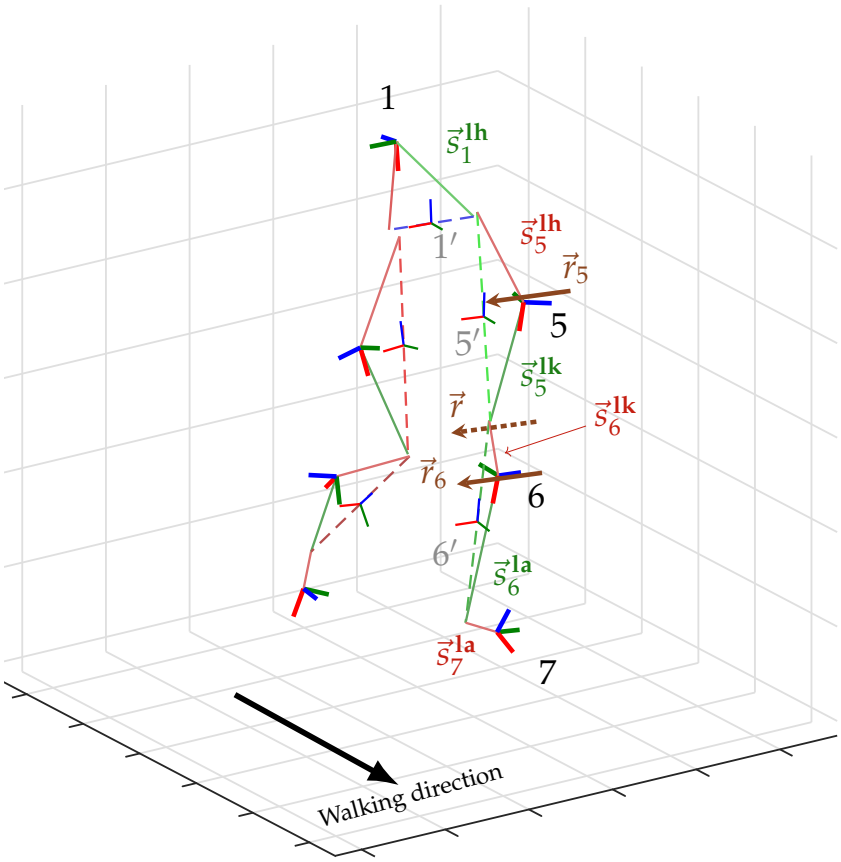

Figure 3-1: The human-IMU kinematic system, with the subject mid-stride. Image is an excerpt frame from a 3D animation of the results of this proposed method. The subject's left leg is labeled with coordinate systems of the IMUs (bold RGB triplets with black text label) and anatomical segments (thin RGB triplets with gray text label), the static vectors from the IMUs to neighboring joint centers (red and green), and the knee's hinge axis (dotted brown) with their static representations in the thigh and shank IMU frames (solid brown). Notation of variables is detailed in Sec. 3.3.1.

3.3.1 Estimated Variables, Derived Quantities, and Notation

The local coordinate frames of the IMUs mounted on the lumbar, right thigh, right shank, right foot, left thigh, left shank, and left foot are denoted as 1, 2, 3, 4, 5, 6, 7 respectively. The coordinate frames of the underlying pelvis, right femur, right tibia, right calcaneus, left femur, left tibia, and left calcaneus anatomical segments are denoted with a prime symbol ($'$) above their associated IMU frame: $1'$, $2'$, $3'$, $4'$, $5'$, $6'$, $7'$, respectively. The shared navigation frame is denoted as $\mathbf{N}$. Denote a numbered *keyframe* $k = 1...M$, within the set of all keyframes $\mathcal{K}$. Let $i, j \in \mathcal{K}$ denote any two consecutive keyframes. The set of all IMU measurements (gyroscope and accelerometer) between keyframes i and j is denoted $\mathcal{I}_{(i,j)}$. As explained later (Sec. 3.3.2), the IMU states are not estimated at each measurement, but rather at a lower rate for computational efficiency.

The following variables are estimated in the model:

- Discrete time-series pose trajectory of each IMU: $\mathcal{X}_{1,k}^{\mathbf{N}}$, $\mathcal{X}_{2,k}^{\mathbf{N}}$, $\mathcal{X}_{3,k}^{\mathbf{N}}$, $\mathcal{X}_{4,k}^{\mathbf{N}}$, $\mathcal{X}_{5,k}^{\mathbf{N}}$, $\mathcal{X}_{6,k}^{\mathbf{N}}$, $\mathcal{X}_{7,k}^{\mathbf{N}}$ $\in SE(3)$ for $k = 1...M$. It should be noted that a pose from frame A to the navigation frame, $\mathcal{X}_{A}^{\mathbf{N}} \in SE(3)$ may equivalently be expressed in terms of its orientation $R_{A}^{\mathbf{N}} \in SO(3)$ and position $p^{A} \in \mathbb{R}^3$ components.

- Discrete time-series velocities of each IMU: $\vec{v}_{1,k}$, $\vec{v}_{2,k}$, $\vec{v}_{3,k}$, $\vec{v}_{4,k}$, $\vec{v}_{5,k}$, $\vec{v}_{6,k}$, $\vec{v}_{7,k} \in \mathbb{R}^3$ for $k = 1...M$

- Discrete time-series angular velocities of each IMU: $\widehat{\omega}_{k}^{1}$, $\widehat{\omega}_{k}^{2}$, $\widehat{\omega}_{k}^{3}$, $\widehat{\omega}_{k}^{4}$, $\widehat{\omega}_{k}^{5}$, $\widehat{\omega}_{k}^{6}$, $\widehat{\omega}_{k}^{7} \in \mathbb{R}^3$ for $k = 1...M$

- Discrete time-series accelerometer and gyroscope biases for each IMU: $\vec{b}_{1,k}$, $\vec{b}_{2,k}$, $\vec{b}_{3,k}$, $\vec{b}_{4,k}$, $\vec{b}_{5,k}$, $\vec{b}_{6,k}$, $\vec{b}_{7,k} \in \mathbb{R}^6$ for $k = 1...M$

- The (static) hinge axis of the right knee, expressed in the right thigh and right shank IMU frame, respectively: $\vec{r}_2, \vec{r}_3 \in \mathbb{S}^2$, and similar for the (static) axis of the left knee expressed in its respective thigh and shank frame: $\vec{r}_5, \vec{r}_6 \in \mathbb{S}^2$

- The (static) vector from the IMU frame to each adjacent joint center, i.e., the vector from the
  - lumbar IMU frame to the right hip rotation center: $\vec{s}_1^{\mathbf{rh}} \in \mathbb{R}^3$,
  - right thigh IMU to the right hip center: $\vec{s}_2^{\mathbf{rh}} \in \mathbb{R}^3$,
  - right thigh IMU to the right knee center: $\vec{s}_2^{\mathbf{rk}} \in \mathbb{R}^3$,
  - right shank IMU to the right knee center: $\vec{s}_3^{\mathbf{rk}} \in \mathbb{R}^3$,
  - right shank IMU to the right ankle center: $\vec{s}_3^{\mathbf{ra}} \in \mathbb{R}^3$,
  - right foot IMU to the right ankle center: $\vec{s}_4^{\mathbf{ra}} \in \mathbb{R}^3$
  - lumbar IMU frame to the left hip rotation center: $\vec{s}_1^{\mathbf{lh}} \in \mathbb{R}^3$,
  - left thigh IMU to the left hip center: $\vec{s}_5^{\mathbf{lh}} \in \mathbb{R}^3$,
  - left thigh IMU to the left knee center: $\vec{s}_5^{\mathbf{lk}} \in \mathbb{R}^3$,
  - left shank IMU to the left knee center: $\vec{s}_6^{\mathbf{lk}} \in \mathbb{R}^3$,
  - left shank IMU to the left ankle center: $\vec{s}_6^{\mathbf{la}} \in \mathbb{R}^3$,
  - left foot IMU to the left ankle center: $\vec{s}_7^{\mathbf{la}} \in \mathbb{R}^3$

The following quantities are not estimated, but rather derived from estimated variables in the model:

- Discrete time-series orientations of the anatomical pelvic, right femur, right tibial, left femur, and left tibial segments: $R^{\mathbf{N}}_{1',k}$, $R^{\mathbf{N}}_{2',k}$, $R^{\mathbf{N}}_{3',k}$, $R^{\mathbf{N}}_{5',k}$, $R^{\mathbf{N}}_{6',k} \in SO(3)$ for $k = 1...M$
- The time-series flexion/extension, internal/external rotation, and abduction/adduction joint angles of the knee and hip

The coordinate systems of the pelvis, femur and tibia segments are assumed to be statically related to the coordinate systems of the IMU mounted on the surface of the associated limb segment. These anatomical coordinate systems are defined according to the recommendations of the International Society of Biomechanics ([75]):

z: positive in the proximal direction

y: positive in the anterior direction

x: positive to the subject's right

This choice of anatomical coordinate system is motivated by the desire to derive joint angle definitions which are meaningful to end-users.

3.3.2 Model

The following sections detail the proposed model of this work. Sec 3.3.2 describes the time-series IMU dynamics, Secs. 3.3.2-3.3.2 describe the biomechanical and anthropometric constraints: knee pseudo-hinge kinematics (Sec. 3.3.2), the relationship between the knee's hinge axis and the femur/tibia proximal direction (Sec. 3.3.2), constrained joint center of rotation between adjacent IMUs (Sec. 3.3.2), anthropometry of femur length, tibia length, and pelvic width (Sec. 3.3.2), maximum/minimum allowable anthropometric lengths (Sec. 3.3.2), and femur and tibia length discrepancy (Sec. 3.3.2). Sec. 3.3.2 presents this model within a MAP estimation framework. Finally, Sec. 3.3.2 presents noteworthy model unobservability conditions.

IMU Dynamics Model

The following IMU dynamics model is due to Forster et al. [70] and summarized here. An IMU takes measurements in the local body frame B; specifically, rotation rate about the local body axes, $\tilde{\omega}$, and body acceleration in the local frame $\tilde{a}$. These measurements are imperfect, corrupted by slowly-varying biases $\vec{b}^{\omega}$ and $\vec{b}^{a}$ and additive zero-mean white noise $\mathbf{v}_{\omega} \sim \mathcal{N}(0, \sigma_{\omega}^2)$ and $\mathbf{v}_{a} \sim \mathcal{N}(0, \sigma_{a}^2)$.

$$\widetilde{\omega}(t) = \omega(t) + \vec{b}^{\omega}(t) + \mathbf{v}_{\omega}(t) \tag{3.1a}$$

$$\widetilde{a}(t) = (R_B^{\mathbf{N}})^{-1}(a_{\mathbf{N}}(t) - \mathbf{g}) + \vec{b}^{a}(t) + \mathbf{v}_{a}(t) \tag{3.1b}$$

where $\mathbf{g}$ is the acceleration due to gravity constant, expressed in the navigation frame. Using a kinematic model

$$\frac{dR_B^{\mathbf{N}}(t)}{dt} = R_B^{\mathbf{N}}(t)\left[\omega(t)\right]_\times, \frac{d\vec{v}(t)}{dt} = a_{\mathbf{N}}(t), \frac{dp(t)}{dt} = \vec{v}(t) \tag{3.2}$$

and integrating over the interval $[t, t+\Delta t]$, the kinematic model as a function of the IMU measurements $\widetilde{\omega}$ and $\widetilde{a}$ is written:

$$R_B^{\mathbf{N}}(t+\Delta t) = R_B^{\mathbf{N}}(t)\exp((\widetilde{\omega}(t) - \vec{b}^{\omega}(t) - \mathbf{v}_\omega^d(t))\Delta t) \tag{3.3a}$$

$$\vec{v}(t+\Delta t) = \vec{v}(t) + \mathbf{g}\Delta t + R_B^{\mathbf{N}}(t)(\widetilde{a}(t) - \vec{b}^{a}(t) - \mathbf{v}_a^d(t))\Delta t \tag{3.3b}$$

$$p(t+\Delta t) = p(t) + \vec{v}(t)\Delta t + \frac{1}{2}\mathbf{g}\Delta t^2 + \frac{1}{2}R_B^{\mathbf{N}}(t)(\widetilde{a}(t) - \vec{b}^{a}(t) - \mathbf{v}_a^d(t))\Delta t^2 \tag{3.3c}$$

where $\mathbf{v}_a^d(t)$ is the discrete-time noise, related to the continuous-time spectral noise through $Cov(\mathbf{v}_a^d(t)) = \frac{1}{\Delta t}Cov(\mathbf{v}_a(t))$, and similarly for $\mathbf{v}_\omega^d(t)$.

Eqs. 3.3 represent a valid set of constraints that could be incorporated in an inference problem to model IMU dynamics and estimate the state trajectory of an IMU $\{R(t), p(t), \vec{v}(t), \vec{b}^a(t), \vec{b}^\omega(t)\}$. However, typically these equations are discretized at the the same rate as the IMU measurements (i.e., $\frac{1}{\Delta t}$) which is often more frequent than necessary for most biomechanics applications. Forster et al. [70] develops a suitable model for IMU preintegration on-manifold which enables the summary of all IMU accelerometer and gyroscope measurements between two keyframes $k = i$ and $k = j$, denoted by $\mathcal{I}_{(i,j)}$, into a single compound probabilistic constraint. Given $\mathcal{I}_{(i,j)}$, the residual error model $r_{\mathcal{I}_{i,j}} \in \mathbb{R}^9$ and the error model of slowly-time-varying measurement bias $r_{\mathbf{b}_{i,j}} \in \mathbb{R}^6$ are given in Eqs. (37) and (40) in Forster et al. [70]. This model of IMU dynamics evolution is used for each IMU in the current work.

Additionally, the instantaneous angular velocity of the IMU at keyframe k is also estimated. The estimated angular velocity $\widehat{\omega}$ is simply related to the gyroscope measurement

$\widetilde{\omega}$ which coincides with keyframe k as

$$e_k = f_\omega(\widehat{\omega}_k, \vec{b}_k^{\omega}, \widetilde{\omega}_k) = \widehat{\omega}_k + \vec{b}_k^{\omega} - \widetilde{\omega}_k, \quad e_k \sim \mathcal{N}(0, \Sigma_g) \quad \forall\, k \tag{3.4}$$

Knee Pseudo-hinge Kinematics

The human knee is assumed to act as a pseudo-hinge with a single point of rotation. Moreover, the major hinge axis $\vec{r}$ is assumed to be statically representable in both the thigh IMU and shank IMU coordinate frames. For a perfect point-rotation hinge joint, the relative angular velocity across the joint will point normal to the plane of rotation (*see* McGrath et al. [125]). At every estimated IMU state keyframe, this relative angular velocity $\vec{m}_k$ (Fig. 3-2) may be computed. Due to soft tissue artifacts and the imperfect hinge kinematics of the joint, these vectors will not all point exactly in the same direction.

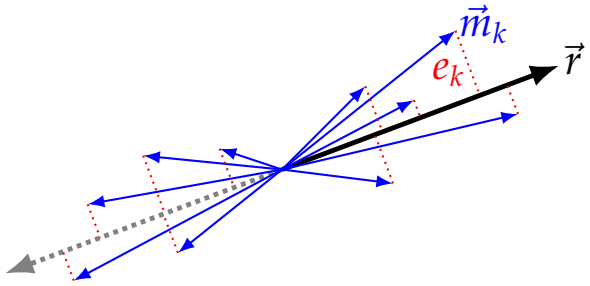

Figure 3-2: The set of relative angular velocity vectors $\vec{m}_k$ projected onto knee axis $\vec{r}$ with resulting residuals e_k. Note that for a perfect hinge $m_k \parallel \vec{r}\, \forall\, k$; however, due to imperfect hinge kinematics of the human knee and soft tissue perturbation of the gyroscopes mounted to the skin of the leg, the set of vectors $\vec{m}_k$ takes this characteristic double cone shape.

A point estimate of the hinge axis $\vec{r}$ may be found by minimizing the projection of $\vec{m}_k$ onto $\vec{r}$, as given by:

$$\frac{(\vec{m}_k \cdot \vec{r})\vec{r}}{\|\vec{r}\|_2^2} \quad \forall\, k$$

Since $\vec{r}$ is always a unit axis, $\|\vec{r}\|_2^2 = 1$. Hence, the line segment between $\vec{m}_k$ and the

projection of $\vec{m}_k$ onto $\vec{r}$ is simplified to $\vec{m}_k - (\vec{m}_k \cdot \vec{r})\vec{r}$. The error model is then given by:

$$e_k = \vec{m}_k - (\vec{m}_k \cdot \vec{r})\vec{r}, \quad e_k \sim \mathcal{N}(0, \Sigma_k) \quad \forall\, k \tag{3.5}$$

Consider a hinge joint flanked by an IMU proximal and distal to the joint, A and B respectively. Then for each keyframe k, the relative angular velocity across the joint may be computed in frame A as

$$m_k = \vec{\omega}^A_{B-A} = (R^{\mathbf{N}}_{A,k})^{-1} R^{\mathbf{N}}_{B,k}\, \widehat{\omega}_{B,k} - \widehat{\omega}_{A,k} \quad \forall\, k \tag{3.6}$$

Combining Eq. 3.5 and 3.6, the full error model for the hinge axis expressed statically in frame A may be rewritten as

$$\begin{aligned} e_k &= f_K(\vec{r}_A, R^{\mathbf{N}}_{A,k}, R^{\mathbf{N}}_{B,k}, \widehat{\omega}_{A,k}, \widehat{\omega}_{B,k}) = \\ {R^{\mathbf{N}}_{A,k}}^{-1} R^{\mathbf{N}}_{B,k} \widehat{\omega}_{B,k} - \widehat{\omega}_{A,k} - ({R^{\mathbf{N}}_{A,k}}^{-1} R^{\mathbf{N}}_{B,k} \widehat{\omega}_{B,k} - \widehat{\omega}_{A,k} \cdot \vec{r}_A)\vec{r}_A \qquad & e_k \sim \mathcal{N}(0, \Sigma_K) \quad \forall\, k \end{aligned} \tag{3.7}$$

This kinematic relationship can also be exploited for the hinge axis in the distal IMU frame by simply rearranging the arguments of Eq. 3.7,

$$e_k = f_K(\vec{r}_B, R^{\mathbf{N}}_{B,k}, R^{\mathbf{N}}_{A,k}, \widehat{\omega}_{B,k}, \widehat{\omega}_{A,k}) \quad \forall\, k \tag{3.8}$$

Constrained Joint Centers of Rotation

Originally proposed by Kok et al. [97] and commonly adapted across other implementations, the pose relationship between IMUs can be exploited. For any two IMUs mounted on either side of a 3DOF point-rotation joint, it is assumed that there is a vector which is static in each IMU frame which points to the center of rotation of the common joint. In the navigation frame, these vectors, composed with their associated IMU poses, should represent the same point—the joint's center.

For any IMUs A and B flanking joint rotation center $\mathbf{j}$, there exist static vectors in each

IMU frame ($\vec{s}_A^{\,\mathbf{j}}$ and $\vec{s}_B^{\,\mathbf{j}}$ respectively), such that the following relationship holds.

$$e_k = f_J(\mathcal{X}_{A,k}^{\mathbf{N}}, \vec{s}_A^{\,\mathbf{j}}, \mathcal{X}_{B,k}^{\mathbf{N}}, \vec{s}_B^{\,\mathbf{j}}) = \mathcal{X}_{A,k}^{\mathbf{N}} \vec{s}_A^{\,\mathbf{j}} - \mathcal{X}_{B,k}^{\mathbf{N}} \vec{s}_B^{\,\mathbf{j}}, \quad e_k \sim \mathcal{N}(0, \Sigma_{\mathbf{j}}) \quad \forall\, k \tag{3.9}$$

Angle Between the Knee Rotation Axis and Femur/Tibia Proximal

There exists an anthropometric relationship between the knee's primary axis of rotation and the femur/tibia segment length. Hollister et al. [79] measured this angular distribution between the knee's (lateral-pointing) rotation axis and the femur and tibia segments through the range of knee flexion/extension, and this relationship is not necessarily orthogonal. Such a model is useful in aiding model identifiability, discussed in detail in Sec. 3.3.2. A probabilistic constraint can be formulated to model this relationship. The angle between an axis $a \in \mathbb{R}^3$ and a segment s, both expressed in a common frame, can be written as:

$$\theta = \arccos\left(\frac{a \cdot s}{(\|a\|_2 \, \|s\|_2)}\right) \tag{3.10}$$

where it is noted that for a unit axis, $\|a\|_2 = 1$. This motivates the following error model for the right thigh:

$$e = f_o(\vec{r}_2, \vec{s}_2^{\,\mathbf{rh}}, \vec{s}_2^{\,\mathbf{rk}}) = \mu - \arccos\left(\frac{\vec{r}_2 \cdot (\vec{s}_2^{\,\mathbf{rh}} - \vec{s}_2^{\,\mathbf{rk}})}{\left\|\vec{s}_2^{\,\mathbf{rh}} - \vec{s}_2^{\,\mathbf{rk}}\right\|_2}\right), \quad e \sim \mathcal{N}(0, \sigma_o^2) \tag{3.11}$$

and similarly for other segments, where μ and σ are the expected mean and standard deviation of the angle between the knee's rotation axis and the segment proximal vector. In Hollister et al. [79], the values for μ are given for the *interior* angle between the medial-pointing knee rotation axis and femur and tibia. However, in this model, the knee's rotation axis is assumed to point to the subject's right per ISB conventions [75]. Therefore, the adjusted values for μ and σ can be found in Table 3.1.

Table 3.1: Distribution of angle between the knee's rotation axis and the leg segments according to Hollister et al. [79] for use in Eq. 3.11, adapted for a right-pointing knee axis and proximal-pointing segment definition

Segment	μ	σ
Right femur	180°-84°	2.4°
Right tibia	88°	1.2°
Left femur	84°	2.4°
Left tibia	180°-88°	1.2°

Femur Length, Tibia Length, and Pelvic Width From Anthropometry

For any IMU which is between *two* neighboring joint centers, i.e., the thigh and shank IMUs, there exists an anthropometric relationship between these two joint centers which has likely been tabulated in an anthropometric database. This relationship more precisely specifies the kinematic model of the human, especially under insufficient kinematics to identify model parameters or significant measurement noise. For an IMU A between two joints centers j_1 and j_2, the static vectors from the IMU frame to the neighboring joint frame would be denoted $\vec{s}_A^{\mathbf{j_1}}$ and $\vec{s}_A^{\mathbf{j_2}}$. Let the distance between these joint centers be denoted L, where an approximately-normal distribution from anthropometric measurements exists as $L \sim \mathcal{N}(\mu_L, \sigma_L^2)$. Then the distance between joint centers j_1 and j_2 may be constrained using this prior information.

$$e = f_L(\vec{s}_A^{\mathbf{j_1}}, \vec{s}_A^{\mathbf{j_2}}; \mu_L) = \left\| \vec{s}_A^{\mathbf{j_1}} - \vec{s}_A^{\mathbf{j_2}} \right\|_2 - \mu_L, \quad e \sim \mathcal{N}(0, \sigma_L^2) \tag{3.12}$$

Maximum/Minimum Anthropometric Lengths

In addition to the probabilistic encoding of subject anthropometry in Eq. 3.12, it is sometimes also useful to encode a hard maximum and/or minimum anthropometric length, which practically limits the solution space to reasonable values of segment lengths.

This constraint is specifically relevant when using generic population measures for anthropometry (as is done in this work) rather than specifically calibrated anthropometric lengths. For a given state variable x for which minimum x_{min} and maximum x_{max} are desired, a continuously differentiable function may be defined which models zero error on the interval $[x_{min}, x_{max}]$, with increasing error otherwise.

$$f_M(x; x_{min}, x_{max}, a) = \begin{cases} (x - x_{max})(\tanh(a(x - x_{max})))^2 & x > x_{max} \\ (x_{min} - x)(\tanh(a(x_{min} - x)))^2 & x < x_{min} \\ 0 & \text{otherwise} \end{cases} \tag{3.13}$$

This may be encoded as a noise model in the system. For any vectors in frame A which span a common limb segment and anthropometric limits x_{min} and x_{max},

$$e = f_M(\left\| \vec{s}_A^{\,\mathbf{j_1}} - \vec{s}_A^{\,\mathbf{j_2}} \right\|_2, x_{min}, x_{max}; a) \tag{3.14}$$

As this error model is introduced to the system to model a hard limit constraint, the distribution of e is not motivated from the dynamics of the system. Rather, the "strength" of the constraint may be tuned through the adjustment of error model scalar parameter a.

Femur and Tibia Length Discrepancy

In addition to aforementioned anthropometric information about the distribution of femur and tibia lengths, there also exists anthropometric information about the *discrepancy*, or difference, between the right and left femur and tibia [176, 186, 151]. Similarly, such a constraint is useful to precisely specify the human kinematic model, especially under insufficient kinematics or high measurement noise. Assuming that this distribution is on average zero for the greater population, a probabilistic model of this error distribution for the femur is written:

$$e = f_D(\vec{s}_2^{\,\mathbf{rh}}, \vec{s}_2^{\,\mathbf{rk}}, \vec{s}_5^{\,\mathbf{lh}}, \vec{s}_5^{\,\mathbf{lk}}) = \left\| \vec{s}_2^{\,\mathbf{rh}} - \vec{s}_2^{\,\mathbf{rk}} \right\|_2 - \left\| \vec{s}_5^{\,\mathbf{lh}} - \vec{s}_5^{\,\mathbf{lk}} \right\|_2, \quad e \sim \mathcal{N}(0, \sigma_D^2) \tag{3.15}$$

and similarly for the tibia, where σ_D represents the standard deviation of the discrepancy distribution. According to Shultz and Nguyen [176], $\sigma_D = 0.8$ cm for the femur and $\sigma_D = 0.6$ cm for the tibia.

Full Problem Representation

Recall the convenient IMU numbering scheme of the IMU on the lower back, right thigh, right shank, right foot, left thigh, left shank, and left foot as $\mathcal{S} = \{1, ..., 7\}$ respectively. Let IMU coordinate frames A and B and joint center(s) $\mathbf{j}$ represent relevant parameters of any of the formulated factor error models above. The posterior probability of all variables $\mathcal{Y}$ given all measurements $\mathcal{Z}$ and priors $p(\mathcal{Y}_0)$ is represented as:

$$\begin{aligned} p(\mathcal{Y}|\mathcal{Z}) \propto p(\mathcal{Z}|\mathcal{Y})p(\mathcal{Y}_0) = p(\mathcal{Y}_0) & \underbrace{\prod_{(i,j)\in\mathcal{K}} \prod_{s\in\mathcal{S}} p(\mathcal{I}^s_{(i,j)} | \mathcal{X}^{\mathbf{N}}_{s,i}, \mathcal{X}^{\mathbf{N}}_{s,j})}_{\text{IMU dynamics (Sec. 3.3.2)}} \quad \underbrace{\prod_{k\in\mathcal{K}} \prod_{s\in\mathcal{S}} p(\widetilde{\omega}_{s,k} | \widehat{\omega}_{s,k}, \vec{b}^{\,\omega}_{s,k})}_{\text{IMU angular velocities (Sec. 3.3.2)}} \\ & \underbrace{\prod_{k\in\mathcal{K}} \prod_{(A,B)\in\mathcal{S}} p(\vec{r}_A, \mathcal{X}^{\mathbf{N}}_{A,k}, \mathcal{X}^{\mathbf{N}}_{B,k}, \widehat{\omega}_{A,k}, \widehat{\omega}_{B,k})}_{\text{knee hinge dynamics (Sec. 3.3.2)}} \quad \underbrace{\prod_{k\in\mathcal{K}} \prod_{(A,B)\in\mathcal{S}} p(\mathcal{X}^{\mathbf{N}}_{A,k}, \mathcal{X}^{\mathbf{N}}_{A,k}, \vec{s}^{\,\mathbf{j}}_A, \vec{s}^{\,\mathbf{j}}_B)}_{\text{joint connection (Sec. 3.3.2)}} \\ & \underbrace{\prod_{k\in\mathcal{K}} \prod_{A\in\mathcal{S}} p(\vec{r}_A, \vec{s}^{\,\mathbf{j_1}}_A, \vec{s}^{\,\mathbf{j_2}}_A)}_{\text{knee axis vs. segment proximal (Sec. 3.3.2)}} \quad \underbrace{\prod_{A\in\mathcal{S}} p(\vec{s}^{\,\mathbf{j_1}}_A, \vec{s}^{\,\mathbf{j_2}}_A)}_{\text{Anthropometry (Sec. 3.3.2)}} \quad \underbrace{\prod_{(A,B)\in\mathcal{S}} p(\vec{s}^{\,\mathbf{j_1}}_A, \vec{s}^{\,\mathbf{j_2}}_A, \vec{s}^{\,\mathbf{j_3}}_B, \vec{s}^{\,\mathbf{j_4}}_B)}_{\text{Segment length discrepancy (Sec. 3.3.2)}} \end{aligned} \tag{3.16}$$

The setting of all variables which maximize Eq. 3.16 is referred to as the maximum a posteriori estimate of $\mathcal{Y}$, denoted $\hat{\mathcal{Y}}_{\text{MAP}}$. Equivalently, $\hat{\mathcal{Y}}_{\text{MAP}}$ minimizes the negative log

likelihood of Eq. 3.16, additionally separating the factors into a simple sum of squares of the residual error models presented in Sec 3.3.2. Under the assumption of Gaussian factors,

$$\begin{aligned}\hat{\mathcal{Y}}_{\text{MAP}} = \arg\max_{\mathcal{Y}} p(\mathcal{Y}|\mathcal{Z}) = \arg\min_{\mathcal{Y}} \left[-\log_e\, p(\mathcal{Y}|\mathcal{Z})\right] = \sum_{\mathcal{Y}_0} \|e_0\|^2_{\Sigma_0} + \sum_{s\in\mathcal{S}} \sum_{(i,j)\in\mathcal{K}} \|e^s_{\mathcal{I}}\|^2_{\Sigma_{\mathcal{I}}} + \\ \sum_{k\in\mathcal{K}} \sum_{s\in\mathcal{S}} \left\| f_\omega(\widehat{\omega}_{s,k}, \vec{b}^{\,\omega}_{s,k}, \widetilde{\omega}_{s,k}) \right\|^2_{\Sigma_g} + \sum_{k\in\mathcal{K}} \sum_{(A,B)\in\mathcal{S}} \left\| f_K(\vec{r}_A, \mathcal{X}^{\mathbf{N}}_{A,k}, \mathcal{X}^{\mathbf{N}}_{B,k}, \widehat{\omega}_{A,k}, \widehat{\omega}_{B,k}) \right\|^2_{\Sigma_K} + \\ \sum_{k\in\mathcal{K}} \sum_{(A,B)\in\mathcal{S}} \left\| f_J(\mathcal{X}^{\mathbf{N}}_{A,k}, \mathcal{X}^{\mathbf{N}}_{B,k}, \vec{s}^{\,\mathbf{j}}_A, \vec{s}^{\,\mathbf{j}}_B) \right\|^2_{\Sigma_J} + \sum_{k\in\mathcal{K}} \sum_{A\in\mathcal{S}} f_o(\vec{r}_A, \vec{s}^{\,\mathbf{j_1}}_A, \vec{s}^{\,\mathbf{j_2}}_A)^2/\sigma_o^2 \\ \sum_{A\in\mathcal{S}} f_L(\vec{s}^{\,\mathbf{j_1}}_A, \vec{s}^{\,\mathbf{j_2}}_A)^2/\sigma_L^2 + \sum_{(A,B)\in\mathcal{S}} f_D(\vec{s}^{\,\mathbf{j_1}}_A, \vec{s}^{\,\mathbf{j_2}}_A, \vec{s}^{\,\mathbf{j_3}}_B, \vec{s}^{\,\mathbf{j_4}}_B)^2/\sigma_D^2 \end{aligned} \tag{3.17}$$

The factor graph representation of this problem is given in Fig. 3-3.

Model Identifiability

Following the terminology of Raue et al. [154], the proposed model has a short list of nonidentifiability conditions. There are two *structural nonidentifiabilities*, i.e., inherent unobservability properties of the model.

(Structural nonidentifiability #1) *Gauge freedom* [185] of the solution in absolute position, velocity, and heading. The proposed model does not have an absolute reference for position, velocity, or heading (i.e., GPS or magnetometers). Therefore, the estimated solution is correct *up to* a constant offset in these degrees of freedom. This nonidentifiability is addressed through the use of priors to anchor the solution, as detailed in Sec. 3.4.10.

(Structural nonidentifiability #2) Knee axis sign ambiguity: both the positive and negative sign of knee axes $\vec{r}_A$ and $\vec{r}_B$ are equivalent nonunique solutions to Eqs. 3.7 and 3.8, respectively. This manifests as $2^2 = 4$ discrete equivalent-error local minima per leg. These equivalent local minima are disambiguated post-hoc, detailed in Sec. 3.4.12.

Additionally, the model admits two *practical nonidentifiabilities*, i.e., nonidentifiabilities which are emergent due to insufficient quality or amount of the sensor observations.

(Practical nonidentifiability #1) Nonidentifiability of the four IMU-to-hip static vectors $\vec{s}_1^{\mathbf{rh}}, \vec{s}_1^{\mathbf{lh}}, \vec{s}_2^{\mathbf{rh}}, \vec{s}_5^{\mathbf{lh}}$ when the measurement human kinematic data does not sufficiently explore both hip's degrees of freedom. The hip is modeled as a 3DOF free ball joint. Therefore the solution to the constrained joint center of rotation model (Eq. 3.9) is only identifiable and unique when both IMUs flanking the joint sufficiently rotate in multiple DOF relative to the joint center. This nonidentifiability condition is addressed through the use of a human functional calibration for setting priors on these hip vectors, as detailed in Sec. 3.4.8.

(Practical nonidentifiability #2) Discerning heading relationship between IMUs flanking the hip and ankle joints. In a magnetometer-free estimation framework, the heading relationship between IMUs must be derived from kinematics alone. It is possible that constrained joint center of rotation model Eq. 3.9 provides the necessary information. However, in conditions where one or more of the static vectors from the IMU to neighboring joint centers is generally vertical, i.e., orthogonal to the heading plane, then the associated IMU's orientation trajectory becomes underconstrained and all constant-offset heading solutions are viable. This situation may occur, for example, in upright walking gait with small step length. In the case of the 1DOF knee, this heading relationship between thigh and shank IMUs is well defined by hinge model Eq. 3.7. However, this heading relationship may be underspecified for the more general hip and ankle joints. In order to preclude this nonidentifiability condition during the 30 minute walking task, the hip and ankle joints were also parameterized as a hinge similar to the knee, detailed in Sec. 3.4.9.

The relationship between the knee's axis and segment direction (Eq. 3.11) prevents an additional structural nonidentifiability condition from emerging. As previously discussed

in *practical nonidentifiability #1*, both IMUs flanking a joint must sufficiently rotate in multiple DOF relative to the joint center to yield a unique solution to the constrained joint center of rotation model (Eq. 3.9). In the case of the 1DOF knee, this is biomechanically impossible. Therefore there would be no unique solution to Eq. 3.9—the set of solutions would define a knee rotation center *anywhere* along the medial/lateral line which contains the true knee rotation center. Indeed, for the hip, the medial/lateral location of the rotation center can only be specified through abduction/adduction of the hip. This illustrates the importance of modeling the angular relationship between knee's axis and the femur/tibia segment length through Eq. 3.11. This model specifies *where* along the medial/lateral line the knee rotation center must lie to be consistent with human anthropometric data.

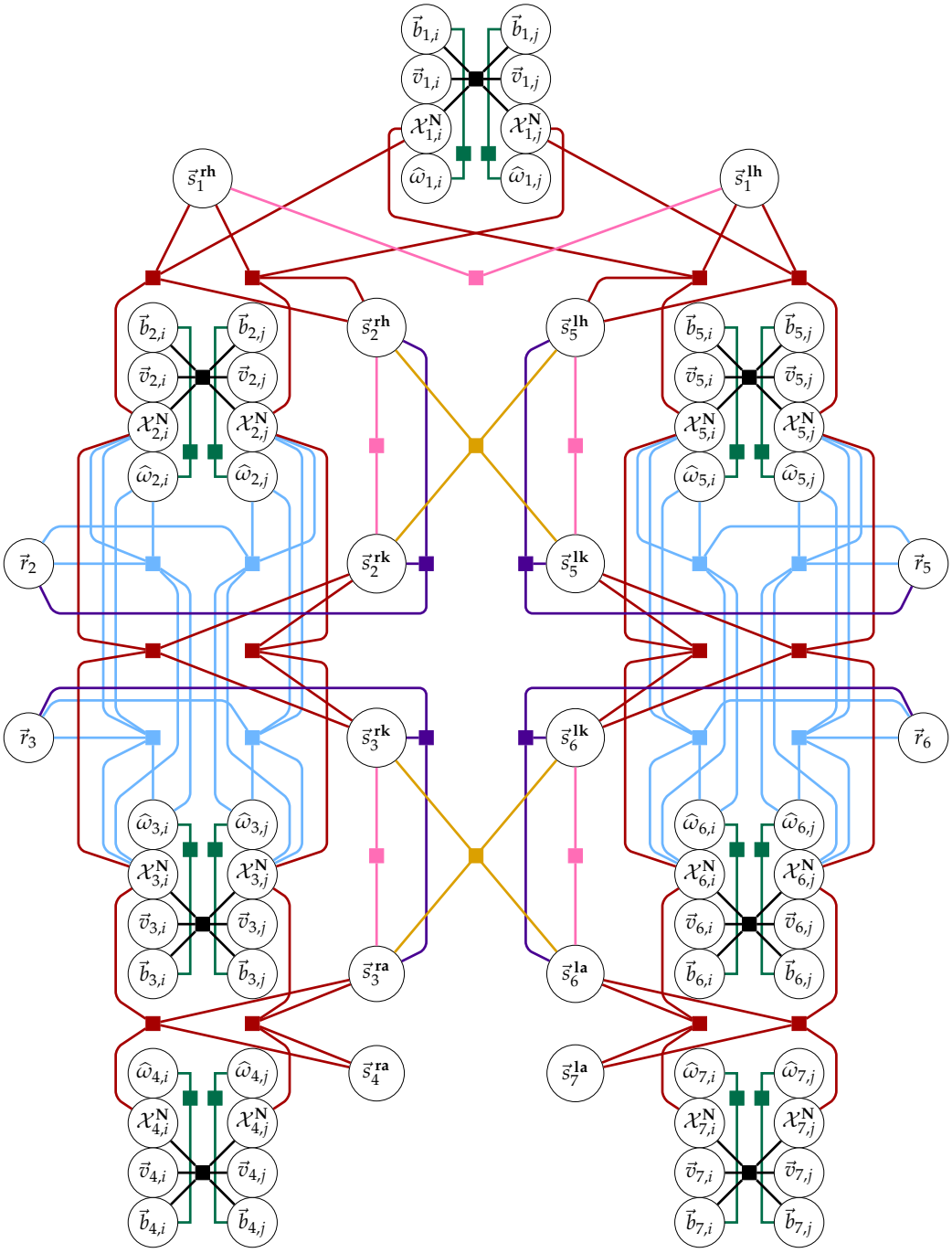

Figure 3-3: Factor graph representation of the problem for consecutive keyframes i and j. Variables are represented as circles, whereas the connecting factors are represented as solid squares.

3.4 Materials and Methods

3.4.1 Participants

Twelve subjects (4 male, 8 female, age = 24.6 $\pm$ 3.0 years) participated in this study. The protocol was approved by the Committee on the Use of Humans as Experimental Subjects at MIT (Protocol 1906898310). Exclusion criteria included (1) diagnosis or self-reporting of any lower extremity impairments that limit the subject's ability to walk, (2) diagnosed or self-reported health conditions (e.g., muscle, heart, etc.) that would prevent the subject for walking for 30 minutes, (3) inability to walk independently of an assistive device for 30 minutes on a treadmill, (4) lack of fluency in the English language.

3.4.2 Study Protocol

First, each participant in the study performed a reference functional calibration, detailed in Sec. 3.4.8. Then, each participant walked for approximately 30 minutes at a self-selected walking speed (speed = 1.13 $\pm$ 0.18 m/s) in order to capture each subject's natural treadmill gait. The calibration task was chosen to address practical nonidentifiablities (Sec. 3.3.2), and the walking task was chosen to represent an operationally-relevant task to end users for which a long dataset may be taken. During treadmill walking, the subject was asked to reach comfortable speed before data recording began, and data recording was ended at least 30 minutes later before the subject ended walking. Each subject was outfitted with a set of reflective motion capture markers (Fig. 3-5) and strap-on IMUs (Opal IMU, APDM, Inc., Portland, OR, USA). The IMUs contain dual 3-axis accelerometers ($\pm$16 g, $\pm$200 g), and a 3-axis gyroscope ($\pm$2000 deg/s). Markers were placed on anatomical landmarks and on the IMUs. These anatomical landmark markers were placed according to a modified Cleveland Clinic lower body marker set for use in OpenSim [174, 55] inverse kinematic modeling. The position of the reflective markers was captured using a 13-camera Vicon

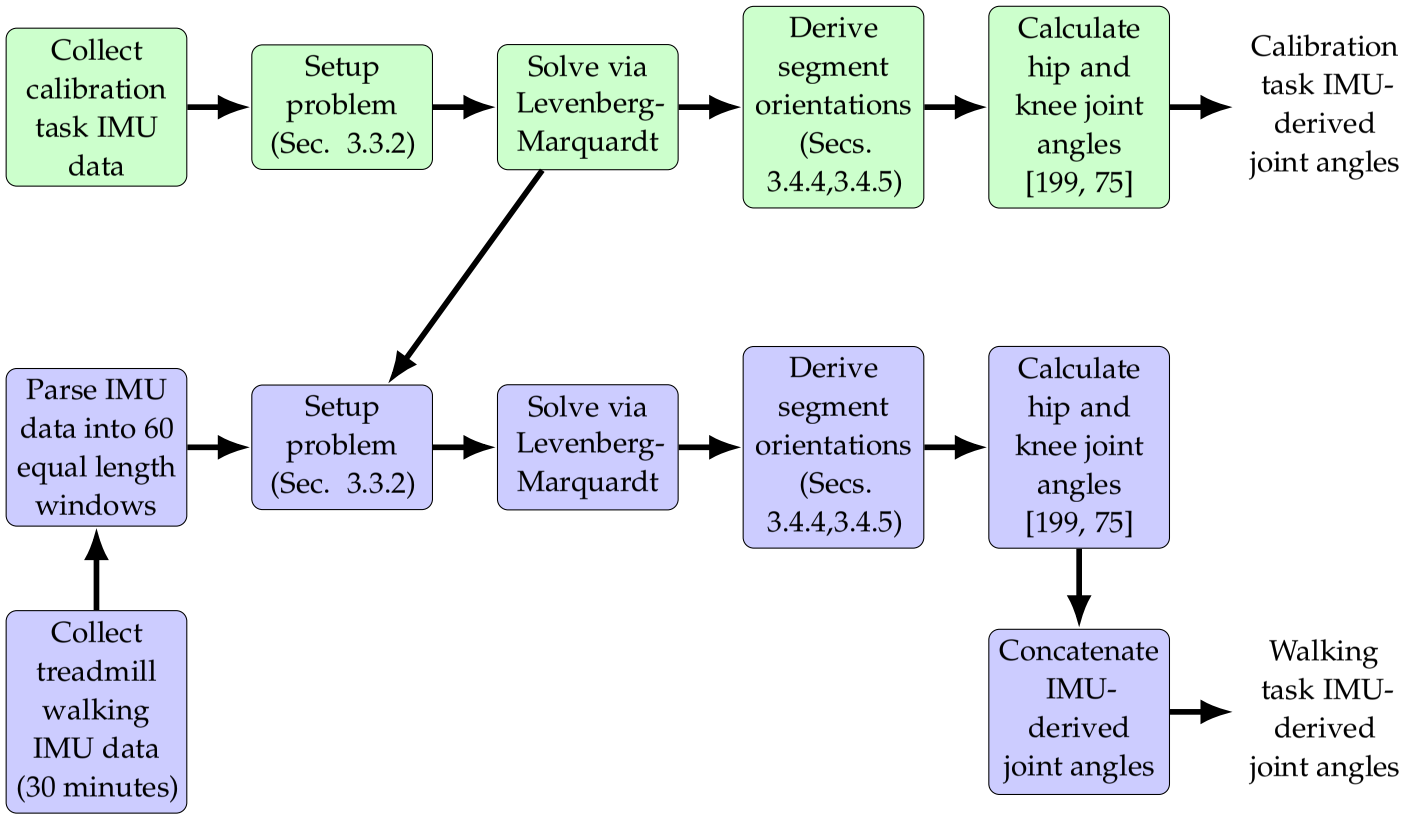

Figure 3-4: Conceptual process methodology to compute IMU-derived joint angles for both the calibration task and the treadmill walking task. Calibration task computed solutions for $\vec{s}_2^{\mathbf{rh}}$, $\vec{s}_1^{\mathbf{rh}}$, $\vec{s}_1^{\mathbf{lh}}$, $\vec{s}_5^{\mathbf{lh}}$ are used as priors in the walking task problem. Levenberg-Marquardt is used as an iterative solver to the proposed optimization problem.

motion capture system (Vicon Motion Systems, Inc., Los Angeles, CA, USA) at a sampling rate of 200 Hz. A timing pulse was used to start and stop the recording of the IMU and motion capture data at the same time, so the measurements were aligned in time and of the same length.

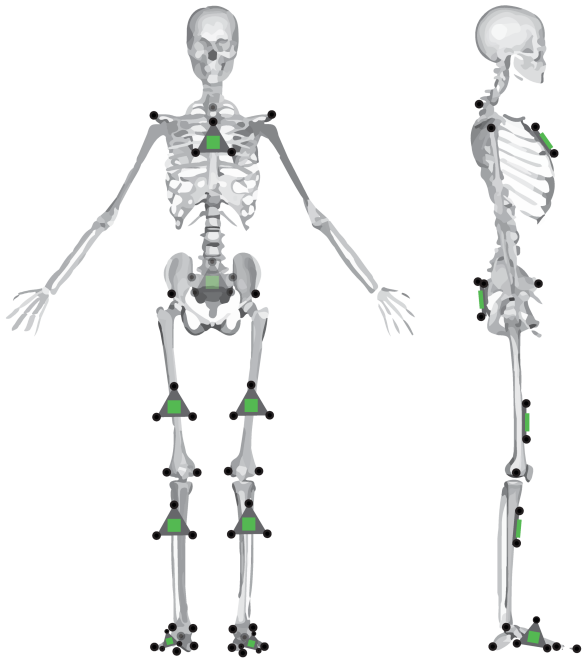

Figure 3-5: Placement of the reflective markers (black circles) and IMUs (green) on the subject. IMUs on the thigh and shank were not placed precisely, and location varied both vertically and in the transverse plane.

3.4.3 Data Processing

A methodology flowchart illustrating the derivation of IMU-based joint angles for the walking and calibration tasks is shown in Fig. 3-4. The optimization of Eq. 3.17 was implemented within the GTSAM 4.0 library [54] in C++ and MATLAB. The measured IMU data were recorded at 200 Hz, and 20 measurements were preintegrated between keyframes, i.e., the time-series IMU poses, velocities, biases—and additionally the derived

joint angle calculations—were estimated at 10 Hz. The large 30 minute dataset was cut into 60 equal-length subsets (approximately 30 seconds long each) to limit computational processing time, memory constraints, and numerical precision. Each of these datasets were processed post-hoc via Levenberg-Marquardt [135]. The size of the system squared Jacobian $\mathbf{J}^\intercal\mathbf{J}$ grows quickly: the number of rows or columns is equal to the total size of all variables in the problem (in their manifold representation). For 30 seconds of data with IMU states estimated at 10 Hz along with static variables for joint hinge axes $\vec{r}$ and static vectors from IMUs to joint centers $\vec{s}$ this yields a square matrix of size 37,850. The problem was solved on an Intel® Core™ i7-4910 MQ CPU (2.90 GHz). Criteria for convergence were the following: an absolute change in error between iterations of 1×10^{-6} or less, a relative change in error of 1×10^{-4} or less, or 10000 iterations, whichever was satisfied first. The optical motion capture data, used as a truth reference in this study, were compared directly to the derived IMU states at 10 Hz. The motion capture data were low-pass filtered with a 30 Hz, 6th order Butterworth filter and then processed in OpenSim 4.0 [174, 55], with inverse kinematics computed according to OpenSim's gait 2392 model [56, 203, 11, 10]. A custom subject model was constructed for each subject prior to processing in the OpenSim solver by scaling the generic model according to anthropometric measures derived from the subject's marker data while static. Additionally, the 3-marker acrylic reference placed on each IMU (Fig. 3-5) allowed for simple calculation of a truth reference for IMU orientation and position in the optical motion capture frame. The IMU data were processed according to the proposed model in Sec. 3.3. For each of the 12 walking trials, time-series measurements were compared: knee and hip joint angles as derived in Sections 3.4.4 and 3.4.5 vs. the OpenSim-estimated joint angles (the truth datum) and estimated IMU orientation vs. marker-based orientation truth reference. When comparing any data to truth, where appropriate, the results from the equal-length subsets were concatenated to form a continuous dataset.

3.4.4 Derivation and Processing of Knee Angles

From the estimated states, it is desired to derive coordinate systems of the underlying femur, tibia, and pelvic anatomical segments. The knee axis and the proximal direction of the femur and tibia are not necessarily orthogonal [79]. The following function is used to construct an orthonormal leg coordinate system (LCS) where the proximal direction ($+z$) is fixed and the right direction ($+x$) is corrected to ensure orthonormality, with the anterior direction ($+y$) derived from the cross product:

$$R_A^{A'} = f_{LCS}(x, z) = \begin{bmatrix} ((z \times x) \times z)^\top \\ (z \times x)^\top \\ z^\top \end{bmatrix} \tag{3.18}$$

Then, the orientation between the IMU on the leg segment and the underlying anatomical segment can be derived for the right femur, right tibia, left femur, and left tibia from the relevant knee axis and normalized proximal vector,

$$R_2^{2'} = f_{LCS}\left(\vec{r}_2, \frac{(\vec{s}_2^{\,\mathbf{rh}} - \vec{s}_2^{\,\mathbf{rk}})}{\left\|\vec{s}_2^{\,\mathbf{rh}} - \vec{s}_2^{\,\mathbf{rk}}\right\|_2}\right) \tag{3.19a}$$

$$R_3^{3'} = f_{LCS}\left(\vec{r}_3, \frac{(\vec{s}_3^{\,\mathbf{rk}} - \vec{s}_3^{\,\mathbf{ra}})}{\left\|\vec{s}_3^{\,\mathbf{rk}} - \vec{s}_3^{\,\mathbf{ra}}\right\|_2}\right) \tag{3.19b}$$

$$R_5^{5'} = f_{LCS}\left(\vec{r}_5, \frac{(\vec{s}_5^{\,\mathbf{lh}} - \vec{s}_5^{\,\mathbf{lk}})}{\left\|\vec{s}_5^{\,\mathbf{lh}} - \vec{s}_5^{\,\mathbf{lk}}\right\|_2}\right) \tag{3.19c}$$

$$R_6^{6'} = f_{LCS}\left(\vec{r}_6, \frac{(\vec{s}_6^{\,\mathbf{lk}} - \vec{s}_6^{\,\mathbf{la}})}{\left\|\vec{s}_6^{\,\mathbf{lk}} - \vec{s}_6^{\,\mathbf{la}}\right\|_2}\right) \tag{3.19d}$$

The knee's three rotation angles are then reported according to Grood and Suntay [75].

3.4.5 Derivation and Processing of Hip Angles

The approach to deriving the hip angles is similar, however, the current problem only estimates information about the medial/lateral direction in the pelvic frame (i.e., from the vector spanning the hip rotation centers in the lumbar IMU frame). An assumption about the proximal or anterior direction is necessary to construct a full definition of the pelvic coordinate system. The following function is used to construct an orthonormal pelvic coordinate system where the right direction ($+x$) is fixed and the proximal direction ($+z$) is corrected to ensure orthonormality, with the anterior direction ($+y$) derived from the cross product:

$$R_A^{A'} = f_{PCS}(x, z) = \begin{bmatrix} x^\top \\ (z \times x)^\top \\ (x \times (z \times x))^\top \end{bmatrix} \tag{3.20}$$

In the current study, the proximal direction in the pelvic frame, $\mathbf{v}^{1'}$, was defined as the approximate average vertical vector from the IMU on the lower back. This approach is only appropriate for upright gait, or $\mathbf{v}^{1'}$ should only be derived from a primarily upright gait portion of a larger dataset. This assumption also drives static offset differences between the derived hip angles and the OpenSim truth hip angles.

Then, the orientation between the lumbar IMU and the pelvic coordinate system can be derived from $\mathbf{v}^{1'}$ and the normalized right direction vector,

$$R_1^{1'} = f_{PCS}\left(\frac{(\vec{s}_1^{\,\mathbf{rh}} - \vec{s}_1^{\,\mathbf{lh}})}{\left\|\vec{s}_1^{\,\mathbf{rh}} - \vec{s}_1^{\,\mathbf{lh}}\right\|_2}, \mathbf{v}^{1'}\right) \tag{3.21}$$

The hip's three rotation angles are then reported according to Wu et al. [199].[1]

[1]There is an inconsistency in segment coordinate system definition between Grood and Suntay [75] and Wu et al. [199], i.e., Grood and Suntay originally define the proximal direction of a segment to be $+z$ but Wu et al. define it to be $+x$. In this work, $+z$ is used for the proximal direction in all segments. The Wu joint coordinate system definition is then modified to report the same angles.

3.4.6 Selection of Noise Parameters

One major advantage of casting the estimation problem of Eq. 3.17 *only* in terms of IMU pose trajectories (i.e., the minimal parameterization of the problem), rather than estimating the time-series pose trajectories of the underlying anatomical frames (c.f. [97, 183]) is that model noise terms may be measured empirically. The IMUs in this experiment had a truth reference—the 3-marker planes on which the IMUs were mounted. Additionally, markers were placed on the medial and lateral rotation points of the knee and ankle to compute the mocap-derived joint centers. The mocap hip center was derived from subject pelvic anthropometry according to Seidel et al. [173], using markers on the anterior and posterior superior iliac spine (ASIS and PSIS, respectively). From these joint center locations according to optical motion capture data, the true distance between the IMU pose and a neighboring joint center can be computed. For a single subject (S1), for each IMU and neighboring joint center combination, the empirical distribution of e_k in Eq. 3.9 and best-fit Gaussian covariance Σ_j were found. This covariance was used for each subject afterward. Similarly for the knee hinge constraint, the empirical distribution of e_i in Eq. 3.7 for S1 was found and best-fit Gaussian covariance Σ_k was used for each subject in the experiment.

3.4.7 Selection of Anthropometric Priors

The parameters of the anthropometric model (Sec. 3.3.2) were defined for the three types of anthropometric constraints present in this model (Table 3.2): (a) distance between ankle and knee rotation centers for both legs, (b) distance between knee and hip rotation centers for both legs, and (c) distance between the two hip rotation centers. Note that as constraint (a) and (b) exist for both legs, there are five anthropometric constraints implemented in the model. If the anthropometric length μ_L is measured precisely for a given subject, associated variance σ_L^2 may be set to a low value to enforce a hard constraint on anthropometric length. However, in this study, and in many other applications, measuring multiple μ_L per subject

is impractical. Therefore, these distributions were inferred from literature.

Table 3.2: Assumed mean and variance for anthropometric priors in the proposed model. All values in meters.

Constraint	μ_L	σ_L	L_{min}	L_{max}	**Source**
Tibial length	0.411	0.026	0.344	0.479	ANSUR II [150], *Calf Link*
Femur length	0.394	0.030	0.326	0.480	ANSUR II [150], *Thigh Link*
Femoral head separation	0.187	0.009	0	0.409	Rabari et al. [153], ANSUR II [150], *Hip Breadth*

The sources used for anthropometric measurements [150, 153] report distributions separately for male and female subjects. As this study incorporated both male and female subjects, a composite distribution must be constructed. Given a measurement mean μ, standard deviation σ for each gender, the larger distribution of measurements was taken as $N((\mu_M + \mu_F)/2, \sigma_M^2 + \sigma_F^2)$.

Additionally, the maximum/minimum anthropometric length constraint of Sec. 3.3.2 was implemented in this model. For the femur and tibia length, the minimum and maximum constraints were set as the 1st percentile female length and the 99th percentile male length, respectively. For femoral head separation, the maximum was set as the 99th percentile male hip breadth. However, as no suitable minimum could be found, this value was set to zero.

3.4.8 Human Calibration

The positional constraint for the common joint centers between IMUs (Eq. 3.9) only yields unique solutions when both IMUs sufficiently rotate about the shared rotation center. This condition is met for many joints and tasks. However, in a nominal gait the lumbar IMU has limited rotation about the hip center, which creates a potential practical

nonidentifiability condition of the hip vectors (Sec. 3.3.2). In order to mediate this concern, a functional calibration which intentionally excites the degrees of freedom of the hip is used to provide identifiable estimates of the four hip vectors, which are in turn used as priors in the model during the walking task.

Human Calibration Protocol

The calibration protocol is meant to excite all of the degrees of freedom of the human joints.

1. *Ankle calibration*: Lift your right foot so that it is hovering a few inches off the ground. Perform three ankle flexion/extension cycles within maximum range of comfort. Then, while foot is lifted a few inches off ground, rotate the front of your foot in a circle three times within maximum range of comfort. Repeat for left ankle.

2. *Knee calibration*: Stand on left foot while keeping both thighs as vertical as possible. Swing right foot behind you (flexing the knee), at least 90 degrees, then return right foot to ground (extending the knee). Do this three times. Repeat for left knee.

3. *Hip calibration*: From standard pose, while keeping knee and ankle neutral, swing your straight right leg up in front of you to maximum range of comfort and return to ground (flexion/extension of hip) three times. Then, perform an adduction/abduction of hip by swinging straight right leg out to lateral side of the body to maximum range of comfort and then returning foot to ground three times. Finally, perform internal/external rotation of hip by keeping foot near to ground and rotating your foot in and out three times to maximum range of comfort while keeping your ankle and knee stiff. Repeat for left hip.

4. *Torso calibration*: From neutral pose, bend down and touch your toes and come back up. Then, twist your torso (forward-left torso twist-forward-right torso twist-

forward) to maximum range of comfort. Finally, a side-to-side bend: up-left-up-right-up.

Human Calibration Data Processing

The calibration data is processed according to the proposed method, with one addition. During each joint calibration step in Sec. 3.4.8, it is assumed that the joint rotation center remains fixed in the world frame—the subject should not be ambulating while performing any of these calibrations. So, during these periods, the static joint center rotation constraint Eq. 3.9 is creatively used to model this assumption. Rather than modeling the connection between IMU frames A and B with connecting static vectors v_A and v_B, the constraint may be used to connect the same IMU to the joint center across consecutive keyframes k and $k+1$ by recasting Eq. 3.9 as:

$$e_k = f_J(\mathcal{X}^{\mathbf{N}}_{A,k}, \vec{s}^{\,\mathbf{j}}_A, \mathcal{X}^{\mathbf{N}}_{A,k+1}, \vec{s}^{\,\mathbf{j}}_A) \tag{3.22}$$

This constraint was added to the factor graph during joint calibration periods. The estimated values for the four vectors relating the two joint centers of rotation, $\vec{s}_1^{\,\mathbf{lh}}, \vec{s}_5^{\,\mathbf{lh}}, \vec{s}_1^{\,\mathbf{rh}}, \vec{s}_2^{\,\mathbf{rh}}$, were used as priors in the general estimation problem for the full walking trial for each subject.

3.4.9 Ankle and Hip Joint Hinge

As described in Sec. 3.3.2, the heading relationship between adjacent IMUs is likely underspecified for the IMUs which flank the hip and ankle joints. In order to preclude this nonidentifiability condition for the 30 minute walking trial, the hip and ankle joints were modeled as kinematic hinges—the proximal and distal IMUs to these joints are constrained in the same way as the knee hinge in Sec. 3.3.2.

3.4.10 Other Priors

This current implementation has no absolute reference of position (e.g., landmarks or GPS) or absolute reference of heading (e.g., landmarks or magnetometers). This leads to a *gauge freedom* [185] of absolute position, velocity, and heading of the estimated solution. There are multiple approaches [212] to remedy gauge freedom; here, the simplest approach is taken. At the first keyframe for the lumbar IMU, a prior of zero position, zero velocity, and zero heading angle is set. This approach will yield an estimated solution which is accurate *up to* a constant offset of absolute position, velocity, and heading.

3.4.11 Initialization

For general nonlinear, nonconvex optimization, consideration of initial point is important. A good initialization of the method not only yields faster convergence, but also reduces the chance of convergence to local minima [31], which will typically produce nonsensical solutions. For this work, position, velocity, and IMU biases were initialized to zero, and orientations were initialized to the identity rotation matrix. Static vectors from IMUs to neighboring joint centers and knee axes were initialized from an assumed nominal alignment.

3.4.12 Hinge Axis Direction Disambiguation

As discussed in Sec. 3.3.2, one structural nonidentifiability of this problem is that both the positive and negative signed knee axes sign are equivalent solutions to Eq. 3.7. This condition does not affect the optimization solution; however will impact the ISB-consistent anatomical coordinate system definition that assumes axes point to the subject's right (Sec. 3.4.4). The following steps were performed post-hoc (after the optimization and prior to joint angle derivation) to ensure that all axes point to the subject's right.

(Step #1) Ensuring both knee axes are pointed in the same direction. First, the sign of $\vec{r}_B$ is adjusted to ensure it points to the same side as $\vec{r}_A$. Both knee axes are transformed into the global frame for all points in time through estimated IMU orientations $R_A^{\mathbf{N}}$ and $R_B^{\mathbf{N}}$. For each point in time, the angle between the knee axes in the world frame is computed. If the median of this distribution is greater than 90 degrees, we conclude that the knee axes point in opposite directions, and the sign of $\vec{r}_B$ is flipped. Otherwise, we conclude that knee axes are pointed in the same direction.

(Step #2) Ensuring both axes are pointed to the subject's right. After Step #1, both knee axes will point to either the subject's left or the subject's right. However, if both axes point to the subject's left, then the knee flexion/extension angle as derived in Sec. 3.4.4 will have the incorrect sign. Per the ISB-recommended knee angle convention (if both knee axes point to the subject's right), the range of motion (ROM) of the knee angle should fall approximately in [+10°,-150°]. If both knee axes point to the subject's left, this ROM will fall in [+150°,-10°]. Therefore, after Step #1 the knee angle is computed. If the median knee angle is greater than +20°, it is concluded that both knee axes must have been pointing to the subject's left. Then both axes' signs are flipped and the angle is recomputed.

3.4.13 Statistical Analysis

Hypothesis 1 considers the RMSE of pitch and roll estimate of individual IMUs in the proposed model compared with a control method, i.e., the individual optimization-based smoothing of each IMU's pose trajectory. For each subject, the pitch and roll error was concatenated across all 7 IMUs and 60 subset data runs. For both the pitch and roll, the concatenated error was tested for normality via Kolmogorov–Smirnov [121], which supported a non-normal distribution of errors. Therefore, separate Friedman tests [71] were performed to assess the effect of algorithm on pitch and roll estimation accuracy.

To characterize IMU position estimation accuracy of the proposed method, RMSE of the norm distance between adjacent IMUs is is reported and computed for each subject as:

$$\text{RMSE}(\left\| p^A_{k,IMU} - p^B_{k,IMU} \right\|_2 - \left\| p^A_{k,OMC} - p^B_{k,OMC} \right\|_2) \quad \forall\, k = 1...M \tag{3.23}$$

where p_{IMU} is the estimation position of the IMU, p_{OMC} is the position of the IMU according to the 3-marker mocap clusters on each IMU, and $(A, B) \in \mathcal{S}$ is every adjacent pair of IMUs in the model. Note that the *norm* difference in position is reported rather than vector components because the proposed model has no guarantee of absolute heading reference, so it was intractable to align the world frame of the proposed model with the world frame of the optical motion capture system.

Comparison of the ground-truth OpenSim-estimated joint angles (hereafter referred to as *mocap angles*) and the joint angles derived according to the proposed method (hereafter referred to as *IMU angles*) for the knee and hip flexion/extension angle were performed according to Bland-Altman [138, 23]. This analysis technique considers a linear regression between the IMU angles and mocap angles. The y-intercept of the regression reveals information about the static bias offset between the mocap angles and the IMU angles. Likewise, the slope may reveal information about dynamic bias in the measurement. Here, *absolute RMSE* is used to refer to the RMSE between the raw mocap angles and IMU angles. *Relative* or *zero-mean* RMSE is used to refer to the RMSE between the raw mocap angles and the IMU angles *after* the IMU angles are corrected via the aforementioned y-intercept. This relative RMSE is used to convey method error after subtracting datum offsets between the IMU and mocap data. These small static offsets between mocap and IMU angles may occur, for example, due to imperfect estimation of the static vectors from the IMUs to neighboring joint centers or imperfect marker placement assumptions in the mocap model. Factors that can influence these static offsets are discussed in Sec. 3.5.

3.5 Results and Discussion

The median wall time to run the optimization to convergence of each 30-second IMU data subset was 680.03 seconds. Tabulated results of pitch and roll RMSE are presented in Table 3.3. Kolmogorov-Smirnov test for normality on both error sets (pitch error difference distribution: $p < 0.001, D = 0.46$, roll error difference distribution: $p < 0.001, D = 0.48$) supported that the difference distributions are not Gaussian. Friedman tests support that there are not significant effects of the model on pitch and roll error estimation (pitch: Friedman $\chi^2(1) = 1.33, p = 0.248$; roll: Friedman $\chi^2(1) < 0.001, p > 0.99$).

Table 3.3: RMSE of pitch and roll across all IMUs and data subsets for a single subject in degrees, compared between the proposed method and a control method

	Proposed Method		**Control Method**	
Subject	**Pitch**	**Roll**	**Pitch**	**Roll**
1	1.833	1.523	1.902	1.918
2	3.860	2.836	1.839	1.985
3	3.105	3.531	1.820	2.715
4	1.377	2.107	1.432	1.991
5	3.697	6.184	2.186	3.565
6	1.020	1.980	1.888	2.118
7	0.966	0.989	1.376	1.755
8	1.875	2.203	1.453	2.149
9	1.903	1.853	1.617	2.000
10	1.657	2.977	1.107	2.833
11	1.622	2.537	1.448	2.684
12	1.247	1.996	0.762	2.090
Average	**2.014**	**2.560**	**1.569**	**2.317**

No significant difference was found between these methods in terms of pitch and roll estimation accuracy. Furthermore, both approaches are very accurate, at approximately 2.5 degrees RMSE or less for both pitch and roll. These results support hypothesis 1—that the proposed method does not significantly increase error of IMU pitch/roll estimation when compared against a robust control method. Note that yaw estimates were not analyzed, as the proposed method did not include any heading reference sensor. A motivation for this work was to estimate skeletal kinematics in a way which did not require accurate absolute yaw estimation.

Table 3.4: RMSE in centimeters of total distance between each IMU pair, per subject, for the 30 minute walking task. Prior to taking the RMSE, data were concatenated across 60 equal-length subset results. For subject 3, an occluded marker prevented computation of true lumbar IMU location.

Subject	**Lumbar RThigh**	**RThigh RShank**	**RShank RFoot**	**Lumbar LThigh**	**LThigh LShank**	**LShank LFoot**
1	6.69	1.54	3.16	4.35	4.90	3.34
2	4.38	1.56	2.88	2.13	4.66	3.60
3	N/A	6.88	1.72	N/A	4.00	3.18
4	5.49	1.10	3.23	2.72	0.44	3.99
5	6.90	5.97	3.79	6.74	8.97	3.27
6	0.82	1.17	2.78	5.30	2.64	3.77
7	7.02	1.21	2.90	7.05	1.53	3.69
8	2.71	1.17	2.97	5.56	1.07	3.55
9	7.76	0.97	1.99	7.71	0.52	3.10
10	6.96	2.24	1.83	5.24	0.86	2.90
11	7.42	4.44	1.89	7.28	3.99	2.90
12	4.57	0.32	2.12	4.82	0.60	2.71
Mean	**5.52**	**2.38**	**2.60**	**5.35**	**2.85**	**3.33**
Std	**2.20**	**2.15**	**0.67**	**1.81**	**2.57**	**0.39**

RMSE of norm distance between adjacent IMUs are reported for each subject in Table 3.4. These results support that the method robustly constrains the positional relationship between IMUs on the human body. As expected, the error is larger for the IMU pairs flanking the hip joints (i.e., the lumbar-thigh IMU pairs), as it is harder to estimate the hip joint's relationships given the limited kinematics of simple walking. While this analysis demonstrates a constrained positional relationship between IMUs, future work is

required to specify operationally-relevant position accuracy criteria for IMU-based human kinematics systems.

RMSE of IMU angles vs. mocap angles is presented in Tables 3.5-3.8. These results are presented for both the human calibration task (Tables 3.5, 3.6) and walking task (Tables 3.7, 3.8). Additionally, both the absolute (raw) RMSE (Tables 3.5, 3.7) and relative RMSE (Tables 3.6, 3.8) are presented.

These results offer a few key takeaways. The proposed method adequately estimates knee flexion/extension, hip flexion/extension and hip abduction/adduction *without* the use of magnetometers to provide IMU heading. Hip internal/external rotation accuracy is largely dependent on the type of task performed. In general, results are more accurate for the functional calibration task than for walking task. This result is expected, as the calibration task excites more degrees of freedom of the human skeleton, yielding estimates of the model variables which more adequately capture the subjects' kinematics. The comparison of absolute vs. relative RMSE highlights how model assumptions can affect derived joint angles. The relative RMSE supports a similarity in the time series of the data, while the absolute measures can be confounded by a static bias that will be further discussed.

Average knee flexion/extension angle absolute/relative RMSE was found to be $8.35^\circ/4.13^\circ$ for the 30 minute walking task and a more accurate $4.30^\circ/2.95^\circ$ for the calibration task. These results are generally in line with the accuracy reported elsewhere in the literature, such as McGrath et al. [125]. However, McGrath et al. [125] used simulated IMU data and assumed the proximal IMU vector for the thigh and shank IMU, whereas this method estimates these quantities and uses real IMU data. The difference between absolute and relative RMSE can be driven by factors associated with both the IMU model and the optical motion capture model to which it was compared. The IMU model accuracy may be partly explained by imperfect estimation of the static vectors from the IMUs to the joint centers. If these joint centers are improperly estimated to lie slightly anterior or posterior of their

Table 3.5: Absolute RMSE (degrees) of IMU joint angles vs. mocap joint angles for the calibration dataset. *F/E* is flexion/extension, *I/E* is internal/external rotation, and *A/A* is abduction/adduction of the joint.

Subject	**RKnee *F/E***	**LKnee *F/E***	**RHip *F/E***	**RHip *I/E***	**RHip *A/A***	**LHip *F/E***	**LHip *I/E***	**LHip *A/A***
1	3.42	2.78	9.58	12.93	5.31	10.60	14.87	6.81
2	3.18	5.89	9.28	21.43	5.91	9.52	19.81	6.10
3	4.34	9.19	8.95	16.83	5.81	10.55	20.47	3.37
4	3.25	6.02	8.45	22.20	5.89	7.96	8.73	4.54
5	3.01	5.47	6.11	17.70	10.26	4.46	13.40	8.48
6	5.00	4.87	6.11	20.76	8.62	4.51	11.89	5.60
7	3.31	6.23	12.21	16.02	7.09	11.55	11.48	4.17
8	3.76	4.71	10.17	11.26	10.48	10.62	19.20	9.15
9	3.95	6.69	10.47	8.44	4.14	12.77	10.12	4.84
10	3.34	3.11	5.90	9.94	6.20	8.29	20.99	8.63
11	3.87	2.90	8.37	8.23	4.55	8.55	12.71	6.32
12	2.23	2.62	5.79	7.94	2.96	4.86	9.79	5.34
Mean	3.55	5.04	8.45	14.47	6.44	8.69	14.46	6.11
Std	0.70	1.97	2.09	5.37	2.32	2.81	4.50	1.86

Table 3.6: Zero-mean RMSE (degrees) of IMU joint angles vs. mocap joint angles for the calibration dataset. *F/E* is flexion/extension, *I/E* is internal/external rotation, and *A/A* is abduction/adduction of the joint.

Subject	**RKnee *F/E***	**LKnee *F/E***	**RHip *F/E***	**RHip *I/E***	**RHip *A/A***	**LHip *F/E***	**LHip *I/E***	**LHip *A/A***
1	2.47	2.23	9.14	11.65	4.84	9.97	7.33	5.64
2	2.17	2.05	9.36	10.97	5.50	11.43	6.52	4.16
3	4.54	4.32	5.04	8.38	5.92	5.28	8.38	3.29
4	2.46	2.99	7.08	7.10	5.15	7.83	10.13	4.62
5	2.89	3.67	5.71	7.35	9.07	4.31	7.16	8.70
6	3.83	2.84	6.07	9.29	8.38	3.23	10.07	4.59
7	3.58	3.02	10.51	14.83	3.78	10.11	12.48	3.25
8	3.00	3.55	9.83	10.80	6.43	9.49	7.87	7.50
9	2.75	2.64	8.79	7.03	4.14	9.08	6.79	4.47
10	3.28	2.58	4.72	5.98	3.63	7.33	12.73	4.72
11	2.38	1.93	6.74	7.78	3.14	7.69	13.20	4.09
12	2.48	2.98	3.85	6.78	2.93	2.99	8.98	1.86
Mean	2.99	2.90	7.24	8.99	5.24	7.40	9.30	4.74
Std	0.70	0.70	2.23	2.60	1.96	2.84	2.41	1.85

Table 3.7: Absolute RMSE (degrees) of IMU joint angles vs. mocap joint angles for the 30 minute walking trial. *F/E* is flexion/extension, *I/E* is internal/external rotation, and *A/A* is abduction/adduction of the joint. Each RMSE is averaged across the 60 equal subsets of the 30 minute walk dataset.

Subject	**RKnee *F/E***	**LKnee *F/E***	**RHip *F/E***	**RHip *I/E***	**RHip *A/A***	**LHip *F/E***	**LHip *I/E***	**LHip *A/A***
1	8.62	6.24	2.51	14.02	15.74	3.28	14.61	20.99
2	5.59	6.30	5.03	7.86	5.22	10.33	57.65	10.23
3	12.33	7.00	9.28	49.13	7.27	10.35	25.06	4.12
4	13.23	6.33	10.38	48.76	44.74	9.38	42.78	38.25
5	5.96	22.23	6.34	8.68	8.40	25.55	48.88	12.50
6	5.25	3.97	16.06	4.65	5.50	15.96	4.70	5.32
7	12.95	6.57	3.44	9.51	4.78	6.85	24.59	4.75
8	14.54	9.28	11.13	8.34	11.21	12.83	33.83	17.80
9	12.22	4.95	2.97	11.94	5.59	12.48	80.19	8.57
10	5.30	4.78	9.56	22.89	24.70	13.82	37.99	24.08
11	11.41	9.20	10.56	14.46	18.39	12.71	48.87	16.12
12	2.78	3.43	6.52	12.79	2.51	6.93	21.65	4.64
Mean	9.18	7.52	7.81	17.75	12.84	11.71	36.73	13.95
Std	4.03	4.97	4.05	15.27	12.01	5.59	20.66	10.22

Table 3.8: Zero-mean RMSE (degrees) of IMU joint angles vs. mocap joint angles for the 30 minute walking trial. *F/E* is flexion/extension, *I/E* is internal/external rotation, and *A/A* is abduction/adduction of the joint. Each RMSE is averaged across the 60 equal subsets of the 30 minute walk dataset.

Subject	**RKnee *F/E***	**LKnee *F/E***	**RHip *F/E***	**RHip *I/E***	**RHip *A/A***	**LHip *F/E***	**LHip *I/E***	**LHip *A/A***
1	2.66	3.29	2.14	30.87	6.11	2.42	24.22	3.27
2	2.81	4.12	3.42	9.60	2.54	10.30	57.83	7.84
3	4.36	4.17	9.03	46.26	7.24	5.24	22.71	4.39
4	3.73	4.06	8.78	52.38	8.87	9.21	39.36	8.26
5	4.61	13.94	2.74	9.46	6.73	15.54	40.21	10.86
6	3.23	3.71	2.24	6.67	5.53	2.19	8.27	5.06
7	2.82	4.47	3.10	6.68	4.43	5.27	24.25	4.94
8	4.35	5.72	4.15	10.63	5.47	5.72	34.03	6.57
9	2.58	2.62	3.00	32.64	5.62	12.67	81.10	8.57
10	4.74	4.37	5.11	25.45	4.38	8.45	37.91	6.70
11	3.62	3.60	3.49	8.09	5.25	9.06	48.08	7.35
12	2.74	2.71	3.49	18.39	2.10	2.42	18.66	2.63
Mean	3.52	4.73	4.22	21.43	5.36	7.37	36.39	6.37
Std	0.82	3.02	2.33	16.03	1.88	4.25	19.57	2.40

true values, this would induce a static offset in the derived joint angles. Additional sources of error may come from imperfect mocap data, such as mismatch between the placement of the physical mocap markers on the human subject and the virtual markers of the scaled OpenSim skeletal model. The OpenSim model is also imperfect, making assumptions about subject geometry and kinematic joint definitions. Soft tissue artifacts also increase error of all IMU-based methods, which is discussed in more detail later. Finally, all joint angles are estimated without a heading reference. It's reasonable to believe that if the subject were in an environment which allowed for robust magnetometer usage (such as outdoors) and a well-calibrated magnetometer was available on the IMU package, that the estimated joint angles would have increased accuracy, because full orientation identifiability would be established rather than relying solely on the kinematics of the system (e.g., the hinge model) to provide information on the heading relationship between IMUs.

It should be noted that only the flexion/extension angle is compared for the knee, as the mocap angles are based on the OpenSim gait 2392 model, which is a 1DOF knee model. However, the proposed method also derives knee internal/external and adduction/abduction angles. Across all subjects, the [25^{th}, 75^{th}] percentiles of knee ROM were [18.7°, 25.2°] for internal/external rotation and [12.4°, 16.6°] for abduction/adduction. In comparison, Deesloovere et al. [57] reports a knee internal/external rotation ROM of 14.41° $\pm$ 4.1° during walking. Lafortune et al. [104] reports a knee abduction/adduction ROM of 10°. Neither of these clinically-accepted ROM values are within the [25^{th}, 75^{th}] percentile of the results from the proposed method. These larger ROM for the IMU-derived angles are possibly due to noises within the system (e.g. soft tissue artifacts) or suboptimal solutions from numerical optimization. As the knee articulates, the motion of muscle and underlying tissue alters the relative orientation between the IMU and anatomical coordinate frames, which may yield the observed overestimation of the full ROM.

Average hip flexion/extension angle absolute/relative RMSE is 9.76°/5.80° and adduction/abduction angle RMSE is 13.40°/5.87° for the 30 minute walking task. For the calibra-

tion task, the average hip flexion/extension angle absolute/relative RMSE is 8.57°/7.32° and adduction/abduction angle RMSE is 6.28°/4.99°. This accuracy is generally similar to other state-of-the-art IMU-based hip angle estimation techniques that incorporate magnetometers, such as Adamowicz et al. [3], who reported a flexion/extension RMSE of 8.62° for walking and 7.88° for a chosen calibration task [29], and also abduction/adduction RMSE of 8.03° in walking and 9.16° in calibration. For the walking task, the hip internal/external angle absolute/relative RMSE is 15.85°/28.91° and for the calibration task this average RMSE was 14.47°/9.15°. In comparison, Adamowicz et al. reported errors of 9.99° during walking and 10.36° during calibration. The proposed method therefore performs similarly during calibration, but has larger error during walking. These results suggest that performance in hip internal/external rotation accuracy is likely task-dependent. Hip angle estimation is confounded by the same error sources as discussed previously. However, the hip internal/external angle estimation is additionally confounded by another source of error: poor hip hinge kinematics. If the hinge kinematic model Eq. 3.7 is insufficient to provide information about relative heading angles between IMUs on the lower back and thighs, then it would be expected that hip internal/external rotation would not be well-estimated using this optimization framework. This point is discussed in further detail later. High error during the walking task is likely anecdotal evidence that the hip did not act as well-defined hinge for most subjects in this study during walking. Additionally, the actual calibration that was applied from the calibration task onto the 30 minute walking task was only a prior on the four static vectors connected to the two hip centers, $\vec{s}_2^{\mathbf{rh}}, \vec{s}_5^{\mathbf{lh}}, \vec{s}_1^{\mathbf{rh}}, \vec{s}_1^{\mathbf{lh}}$. This calibration approach, while minimal, was likely insufficient to also provide practical identifiability of this heading relationship between lower back and thigh IMUs; it is possible that a calibration approach which also applies a prior on initial relative orientation between these IMUs or some prior on the actual internal/external rotation angle may remedy this problem.

Moreover, it should be noted that the reason the relative RMSE was higher than the

absolute RMSE for the hip internal/external rotation angle during the 30 minute walking task was because of poor correlation between the IMU and mocap hip internal/external rotation angle during walking. Poor correlation creates a Bland-Altman regression which is not meaningful—potentially with large y-intercepts which actually *increases* RMSE when applied to the IMU angles. The case of hip internal/external rotation represents a limitation of the absolute vs. relative RMSE reporting approach: it only captures the static offset phenomena in a signal when the *estimated and ground truth signal are highly correlated*, which was true for the other degrees of freedom estimated.

Soft tissue effects on knee angle estimation Comparison between the IMU and mocap angles also reveals information about the soft tissue artifacts impacting the system. Figure 3-6 shows the estimated knee angle plotted against the mocap-derived knee angle for an exemplary case. The plot is shown colored by temporal location in the gait cycle, where the gait cycle is defined from maximum flexion point to maximum flexion point (approximately toe off to toe off) of the same knee's mocap angle. If the knee angle estimate had no error, it would lie along the line with slope equal to one. From the maximum flexion point of the knee, as the knee begins to extend (from toe-off through swing phase), the method tends to slightly underestimate the knee angle value. As the knee reaches maximum extension (approximately heel strike, the top right of Fig. 3-6), there is visible disruption due to soft tissue dynamics occurring at heel strike. The loop at the top right of Fig. 3-6) represents the loading response into midstance phase of gait. Through the rest of the stance phase, the IMU angle tends to moderately overestimate the mocap knee angle.

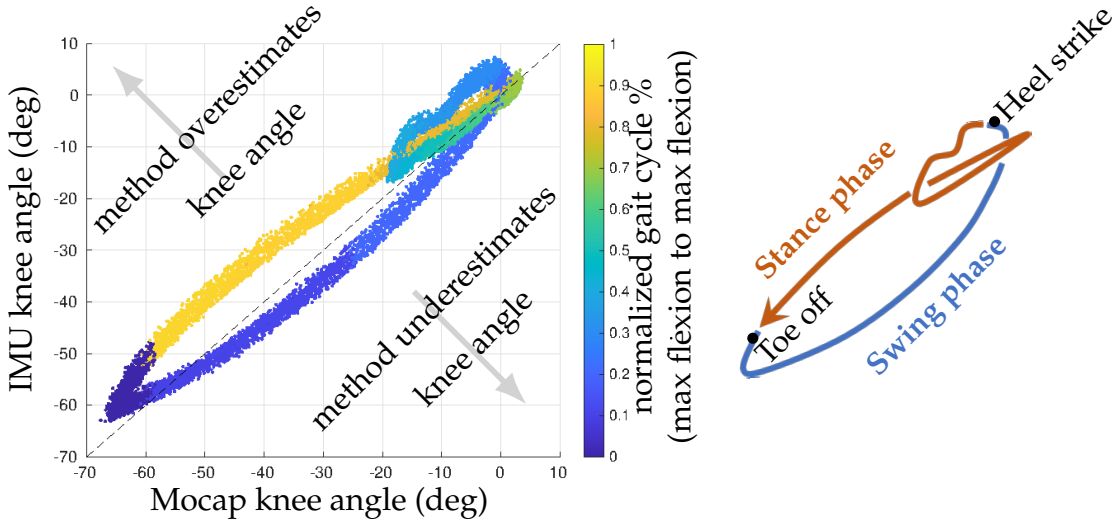

Figure 3-6: (Top) Subject 10 IMU vs. mocap left knee angle, colored by gait cycle. Gait cycle is defined to start and end at knee maximum flexion (approximately toe off). An ideal estimate would lie along the reference line with unity slope, shown as a black dotted line. Note the top-right corner of the data, where a disturbance between the heel strike and toe strike phase is observed. (Bottom) An approximate stylized representation of the gait cycle data, with swing (blue) and stance (orange) phases labeled, along with toe off and heel strike events.

In general, this plot is fairly elliptical except during the heel strike to beginning of foot flat region, where the most soft tissue perturbation is observed. The elliptical shape of this plot (overestimating the mocap angle in one phase vs. underestimating in another phase) is likely due to the tension and compression cycle of the skin tissue through gait. This shape may also be exacerbated by the contraction cycle of the muscles (e.g., quadriceps) during gait, fatty tissue perturbation, or possibly even assumptions of static knee hinge axis and static vectors from the IMUs to neighboring joint centers in the proposed IMU model. Additionally, this quasi-elliptical phenomenon may also be affected through factors of the optical motion capture model, such as static rotation axes or offsets between the virtually modeled markers vs. the actual placement of the markers on the subject. It should also be noted that the IMUs and motion capture markers likely experience different

tissue dynamics. The IMUs are heavier and attached to the human via a thick elastic band. The motion capture markers are very light, attached only via a double-sided adhesive sticker. The mass of the IMU and tension of its elastic band may dampen higher-frequency perturbations that would otherwise affect the optical motion capture markers.

The shape and perturbation effects of Fig. 3-6 are generally seen across subjects. However, it is more prominent in some subjects than others. These effects are likely driven by a complex combination of subject anatomy and anthropometry, such as height, fatty tissue presence, muscle tissue presence, as well as location of the IMU on the thigh and shank surface and subject gait technique. A larger subject study would be required to quantify the systemic factors which contribute to soft tissue perturbation.

This approach illustrates not only the existence of soft tissue artifacts between strap-down body-worn sensors and the optical motion capture model, but also suggests where in the gait cycle these perturbations are most prominent. Future work may include this approach in a larger analysis of the noise dynamics of the tissues of the leg on body-worn IMUs or use this approach to build heuristic correction models which are calibrated for specific subjects (i.e., outside of the heel strike to foot flat region, an elliptical correction of knee angle could be calibrated for a specific subject with only a few scalar parameters).

On quality of hinge joints The kinematic model Eq. 3.7 describes the kinematic relationship between the point estimate of the axis of rotation of the joint, and the orientations and angular velocities of the IMUs proximal and distal to the joint. This leads to an important question: *how "hinge-like" must the kinematics of a joint be in order to leverage this model?*

Figure 3-2 shows an example of a "good" hinge joint, i.e., a joint where the relative angular velocity across the joint tends to lie nearly parallel to the true rotation hinge of the joint. Noise within the system, due to soft tissue perturbation or imperfect IMU orientation and angular velocity estimation, tends to give the set of relative angular velocity vectors an

ideally-narrow double cone shape (the radius of the double cone is roughly proportional to the noise of the hinge system). However, in the case of a non-hinge joint, these relative angular vectors may follow a more spherical distribution. Under this spherical distribution, it becomes difficult to find a point estimate of the hinge joint, as all candidate hinge solutions $\vec{r}$ tend to yield equivalent-error solutions to Eq. 3.7. These non-hinge kinematics represents a practical nonidentifiability condition in the system. A modification of this work which only adds the hinge constraint during known periods of hinge-like behavior would exclude the kinematic measurements which lead to the spherical distribution of relative angular velocity vectors and yield practical identifiability of the hinge axis.

3.5.1 Future Work and Limitations

Future work should systematically assess the properties of a sufficient vs. an insufficient kinematic hinge. Inadequate hinge kinematics represented a limitation in the current work, as the hip joints did not always provide a discernible heading relationship between the lumbar and thigh IMUs (as the knee hinge joint did between the thigh and shank IMUs). Strictly speaking, the hip is not a hinge joint, however, under certain conditions it may be systematically found to provide suitable kinematics to leverage the proposed hinge model. A method which attempts to discern *when* a joint acts as a kinematic hinge (such as [190] for the knee) could potentially be formulated as a probabilistic constraint in this factor graph framework. Furthermore, the current work uses anthropometric measures derived from standard populations. However, in many relevant use cases of this system, an assumption of standard anthropometry may not be appropriate (e.g., for gait analysis, where limb length discrepancies may drive abnormal gait). In these instances, the end user should specifically measure the anthropometry of the subject where possible to avoid increased error due to inappropriate anthropometric constraints in the model.

Future extensions of the current work should also implement more robust initialization schemes which initialize the solution within the "basin of attraction" of the global minimum.

For this work, a few initialization approaches were implemented, but none were shown to be more robust than the trivial "zero" initialization approach. This trivial initialization yields a limitation, as some poor results were almost certainly the result of emergent local minimum in which the optimization method became trapped. Additionally, other solution methodologies such as a simulated annealing [95] type approach may more robustly avoid local minima. Furthermore, IMU-based methods may be confounded by sensor bias. In the current work, time-series IMU gyroscope and accelerometer bias were estimated under a random-walk model with calibration parameters provided by the manufacturer. In the case that high error is observed, it may be necessary to recalibrate the sensor to update its calibration parameters and/or collect robust prior measurements of sensor bias.

The ease of use of the factor graph based approach presented here allows for many possible extensions to this work to be neatly included as probabilistic constraints. These possible extensions include automatic hinge kinematics detection, foot ground contact estimation [130] (while leveraging zero velocity updates and IMU position anchoring), the IMU-to-segment assignment problem [215], gait parameter estimation, activity/task identification, detection of IMU discrete shifting on the body, and many more.

The current work was validated against a simple walking task and a scripted calibration task. While many functional calibration methods are present in the literature, a systematic study of these methods and which minimal set of motions sufficiently excite the degrees of freedom of the human skeleton may unify the numerous approaches. A robotic reference (rather than a human) may be useful in this pursuit–a robot may quickly reproduce motions while removing soft tissue noise. Since no absolute pelvic proximal direction reference was available (in the lumbar IMU frame), the proposed approach can not absolutely derive hip flexion/extension or abduction/adduction. Here, an average gravity vertical vector was assumed as this proximal reference, however, this is only appropriate when derived from upright torso kinematics where a small error is likely induced due to nominal pelvic anterior tilt. This assumption is sufficient for *relative* tracking of the hip joint angles,

informed by the low relative RMSE of these IMU joint angles.

The vectors constraining the IMUs to their neighboring joint centers and joint rotation axes were assumed to be static in the proposed method. This assumption is not strictly true, due to soft tissue perturbation and imperfect hinge kinematics of joints. Future work could consider a time-series bias model of these parameters to better capture these dynamics. In the case of knee flexion/extension, these soft tissue artifacts were well observed when comparing IMU and mocap angles. However, in the case of knee internal/external rotation and abduction/adduction, these were unable to be directly compared because the mocap reference model did not permit these DOF. As a result, only the ROM of these DOF were able to be compared to the literature. Future work should consider using 3DOF models of the knee where appropriate, in order to better capture the effects of system noise on these DOFs. Additionally, all noise models in this work are assumed Gaussian and isotropic. Future work could also consider alternate noise modeling approaches or parameter estimation techniques [211] where appropriate.

3.6 Conclusion

A method has been developed for an optimization-based human lower body kinematics estimator without the use of magnetometers while minimizing external calibrations to the system. The proposed method adequately estimates knee flexion/extension, hip flexion/extension and hip abduction/adduction. Hip internal/external rotation accuracy is largely dependent on the type of task performed. As the walking task did not provide sufficient kinematics to identify the hip's rotational center, a functional calibration task was used to augment the walking task. This method directly estimated the knee's rotation axis and positional relationship between IMUs and their adjacent joint centers, which enabled all joints to be derived and reported using ISB convention. Accuracy of joint angles estimates are presented for both the walking and calibration tasks, and in both absolute

and relative RMSE form, across all 12 subjects in the study. The method was shown to maintain accuracy of IMU pitch/roll estimation once the biomechanical model was added. Relative positional error between adjacent IMUs was less 5.35 cm mean RMSE for all IMU pairs, supporting that the proposed method does robustly constrain IMU positional relationships. The method formulates a number of novel kinematic and anthropometric models of the human lower body, including a hinge model for the knee joint, inclusion of subject anthropometry from population data, femur/tibia segment length discrepancy, and modeling of the angle between the knee's rotation axis and segment proximal direction. These novel constraints provide additional observability to the lower body kinematic model. This work is formulated as a factor graph and implemented in a framework which leverages state-of-the-art IMU estimation techniques. The developed framework allows for expressive inclusion of new kinematics models, intended to provide the foundation for future work to build upon.

Chapter 4

Characterization of Human and Spacesuit Joint Deviations from Body-Worn Inertial Measurement Units

Chapters 2 and 3 describe the development and validation of a robust IMU-based lower-body kinematics estimation framework which requires no calibration under sufficient joint kinematics. As discussed in Chapter 1, this thesis seeks to apply these techniques to inform space suit design and evaluation. This chapter applies the IMU system derived in Chapters 2 and 3 to address two research aims: first, this chapter gives background on a relevant space suit requirement specification. A novel definition of joint deviation is presented to inform this requirement—only from IMU-derived joint angles. Second, this chapter considers specific application to space suit hard bearing joint fatigue modeling. IMU-derived joint angles are used to inform a representative bearing fatigue model based on Lundberg-Palmgren theory. Both of these approaches are demonstrated for a single

subject performing an analog geological survey EVA.

A modified version of this chapter has been accepted in *IEEE Aerospace* (2021) for publication.

4.1 Abstract

Space suits are designed and tested to support humans and work in the vacuum of space and extraplanetary surfaces. Current suit designs intend to enable terrestrial behaviors in extraplanetary settings. In order to inform this design, engineers must understand relevant work environments and human kinematics the suit must support. This work demonstrates the usage of body-worn IMUs to inform suit design parameters, specifically: suit joint cycles per hour requirement specification and suit hard bearing lifespan modeling. From IMU-estimated human joint angles for the elbow, hip, and knee, this work proposes (1) a definition of joint deviation with operational relevance to quantifying suited joint cycles and (2) a model of suit bearing degradation over time based on Lundberg-Palmgren theory. These proposed concepts are demonstrated using a single subject equipped with a set of body-worn IMUs performing a 96 minute long terrestrial fieldwork task—an analog to future extraplanetary science. Results of the counted joint cycles suggest that historical joint cycles/hour requirements (e.g., AX-5 space suit) may be insufficient to capture the full scope of kinematics of planetary fieldwork. Domain experts should consider the level of joint deviation magnitude that is relevant to a designed mission profile. The novel modeling of suit joint rotation and bearing degradation from IMU-based measurements demonstrate an extensible framework to inform future suit design and suited operations evaluation. The use of wearable IMUs has the potential to provide new information for assessing both the operator and the suit through informing physical work demands, mobility requirements, and operations planning.

4.2 Introduction

Extravehicular activity (EVA) is any space operation or activity performed outside the protective environment of a spacecraft, therefore requiring supplemental or independent life support equipment for the astronaut [124]. Space suits are a critical component of EVA support. Suits are designed to and tested against a set of requirements which are specified to provide human work and life support during EVA. Modern suits, such as NASA's next-generation xEMU, utilize hard rotational bearing joints at the waist, hip, shoulder, and wrist [50, 51] in addition to traditional soft goods joints. These hard bearing joints designs are in part motivated by the desire to support operator mobility under increased suit pressure [5].

One requirement of interest for suit joint design is the expected joint cycles per hour, which has more recent heritage in Space Shuttle Extravehicular Activity (EVA) [155]. Future extraplanetary EVA, in contrast to historical Shuttle EVA, will require operational expectations which are less-scripted, with delayed communication, while still supporting productive scientific operations [19, 132]. Previous Shuttle EVA also typically occurred with an operator fixed to a structure (e.g., the Canadarm [163]) in a configuration which constrained lower body kinematics and may not be representative of future terrestrial tasks. Additionally, while modern suit joint component testing literature may suggest that joint testing profiles are inspired by expected motion (e.g., De Baca et al. [14]), there is little literature on *how* this expected motion is systematically assessed. This motivates a research question: can modern data acquisition and processing abilities support the automatic parsing and counting of relevant deviations?

4.2.1 Background

Astronauts undergo significant training in realistic analog environments, allowing ample opportunity for human motion capture. Marker-based optical motion capture

(OMC) represents the current gold standard in human motion capture approaches [34]. This approach requires a set of cameras rigidly mounted around a capture volume to localize the 3D position of a set of reflective markers which are affixed to the human. While this approach is accurate, the measurements must typically be made in a controlled laboratory environment [66], which is intractable for many analog EVA studies. Small, wearable inertial measurement units (IMUs) have been widely used as an alternative to robustly capture human kinematics in the field. Like OMC, however, a mathematical model of the human is necessary to transform IMU measurements into meaningful kinematics outcomes (e.g., skeletal joint angles). One class of IMU-based approaches typically considered precisely aligning the IMUs to the human segments [122, 65, 64, 97] and/or prescribing *a priori* functional calibrations the human must perform to use the system [63, 62, 190, 3]. Other so-called *self-calibrating* approaches have used kinematics models of the skeleton to minimize the need for calibration [170, 137, 125, 183], although functional calibrations may be necessary in the case that the realistic human kinematics are insufficient to get an automatic calibration of the system. These self-calibrating approaches are of particular relevance to the suit community, as suit donning operations are already cumbersome and the suit may restrict the ability to precisely align the IMUs or perform scripted calibration motions.

IMUs have previous been used in suited-human studies. Di Capua and Akin [58] first proposed using IMUs to evaluate human kinematics within the suit. Bertrand et al. [21] studied the differences between joint angles as measured by IMUs on the human arm and suit arm. Anderson et al. [7] used IMUs and pressure sensors in-suit to characterize interaction between the suit and human. Fineman et al. [67] used IMUs on the human and suit to understand suit fit. Kim et al. has recently used IMUs to classify activities and postures while suited [92], as well as compare gait characteristics in gravity offload environments at the NASA Neutral Buoyancy Laboratory (NBL) and Active Response Gravity Offload System (ARGOS) facilities [93].

For the application of informing requirements (namely, suit joint cycles per hour), a definition of joint cycles is needed. Previous literature within the ergonomics domain may offer insight into creating definitions of joint cycles which are assessable by wearable sensors. Many models of ergonomic assessment toward work related musculoskeletal disorders (WRMSDs) have been proposed [178]. Typically, WRMSD risk assessment approaches use visual observation (which is notably error prone [59]). IMUs offer a potentially convenient solution to assessing risk of WRMSDs in situations where optical motion capture is intractable. According to Lim and D'Souza [111], current IMU-based ergonomics assessment typically expresses *intensity* of a motion or posture through ordinal categories based on joint angles (e.g., classifying trunk angle into an ordinal scale of MSD risk [12, 13]) or through some average/cumulative statistic (e.g., average arm acceleration). They state that further research is needed to develop valid and sensitive measurement of WRMSD risk relying on directly-measured exposure data.

One widely used observational model of interest is the Occupational Repetitive Action (OCRA) [143, 144] model for assessing biomechanical risks related to upper limb repetitive movements. Standard ISO 11228-3 [69] suggests OCRA as the preferred method for risk assessment [40]. Colombini and Occhipinti [39] offer the following relevant definition of concepts for OCRA: a *cycle* is a sequence of relatively short technical actions repeated several times in the same way; a *technical action* is a set of motions involving one or more body segments to enable the cycle to be completed. In the case of cyclic motion, these technical actions would include the physical deviations of the joint. This definition is broad by nature, and allows users to provide their own operationally-relevant specific definitions.

Taborri et al. [181] proposed one novel IMU-based algorithm for counting technical actions toward determining the OCRA frequency factor for risk assessment. Their approach used a time and amplitude threshold, counting the first minimum/maximum pair in a signal which meets these thresholds as a technical action. This approach was validated against an expert-created reference count of technical actions from video, where a large

range of errors were reported (from nearly 0% to over 170%), depending on frequency of task and choice of threshold values. The approach of counting everything which meets a threshold as a technical action may lead to erroneous counting (e.g., noisy IMU signals may induce many erroneous local maxima and minima). Supporting a spectrum of technical actions, as occurs in EVA-relevant tasks, requires a method that captures the joint range magnitudes and timing, as opposed to the number of min-max pairings with a fixed threshold.

With EVA-relevant kinematic data, there is also opportunity to inform design and maintenance planning. IMU measurements of the human and/or suit kinematics offer a practical application toward modeling suit bearing lifecycles. The Lundberg-Palmgren [115] model (1947) represents the most commonly used approach to the prediction of rolling-element bearing fatigue life. The bearing's fatigue life is typically specified as its L_{10} life, or the the time that 90 percent of a group of bearings (i.e., identical geometry and loading) will exceed without failing by rolling-element fatigue. This criterion (typically specified in millions of bearing inner-race revolutions) is the basis for calculating bearing life and reliability today [209]. Human (or suit) worn IMUs provide a way to directly measure total rotation of the joint, allowing a bearing fatigue model like Lundberg-Palmgren to be leveraged with kinematically-relevant data.

This work demonstrates the use of body-worn IMUs to measure human kinematics in an analog unsuited extraplanetary EVA environment. A novel definition of human joint deviations is used to summarize human motion by evaluating task joint cycles–which has application to suit requirements specification. We additionally provide a representative analysis for using IMU-derived kinematic data in a bearing failure model. The measured human joint rotations are used as an analog for suit bearing rotation. In combination with an assumed bearing geometry and loading model, these expected bearing rotations are used to inform the operational task time until a joint's L_{10} life is achieved. An IMU-enabled bearing fatigue model may be useful to inform bearing design and evaluation or even as

an online model to monitor total bearing fatigue over time (if a suit were equipped with IMUs). The presented bearing fatigue model is an example model—other models could also be derived based on IMU-measured human and/or suit kinematics.

This chapter will first detail the the novel definition of joint deviation from time-series joint angle measurements, and subsequent interpretations of joint deviation and magnitude (Sec. 4.3). Then, the use of Lundberg-Palmgren fatigue modeling to predict time to bearing L_{10} life, from time series joint angle data and a bearing geometry and loading model is shown (Sec. 4.4). An experiment is performed to collect IMU-based human joint angle data in an analog EVA environment, and the relevant human joints considered, tasks analyzed, and bearing model parameters used are detailed (Sec. 4.5). Results are then presented (Sec. 4.6), namely, plots of cumulative joint deviation magnitudes for each task and joint and the final analyzed bearing L_{10} life. Finally, a discussion of these results in context for space suit design, requirements specification, and testing protocol development is given (Sec. 4.7).

4.3 Defining Joint Deviations

IMUs are mounted to the assumed-rigid limb segments of a human and/or suit. These IMUs measure time-series angular velocity, total acceleration, and possibly local magnetic field. The discrete time-series joint angle $\theta_i \ \forall k = i...N$ may be derived from any number of IMU-based joint angle estimation techniques. The joint angle of interest is assumed to be zero at standing neutral posture and positive in the direction of typical joint articulation (e.g., for hip flexion/extension: $\theta = 0$ in neutral standing, $\theta > 0$ in flexion).

A single *joint deviation* is then defined as a subset of joint angle θ for which the joint deviates greater than a neutral angular threshold η and then returns to less than that threshold. More precisely, a joint deviation $\delta \subset \theta$ is any continuous (in time) proper subset of joint angle θ such that $\theta > \eta$. The joint deviation *magnitude* μ is then defined as the maximum minus the minimum of the deviated angle δ:

$$\mu_j = f_m(\delta_j) = \max(\delta_j) - \min(\delta_j) \; \forall \, j \tag{4.1}$$

The joint deviation duration τ is defined as the length of time the joint remains deviated. A visual representation of this definition over some example joint angle data is shown in Fig. 4-1.

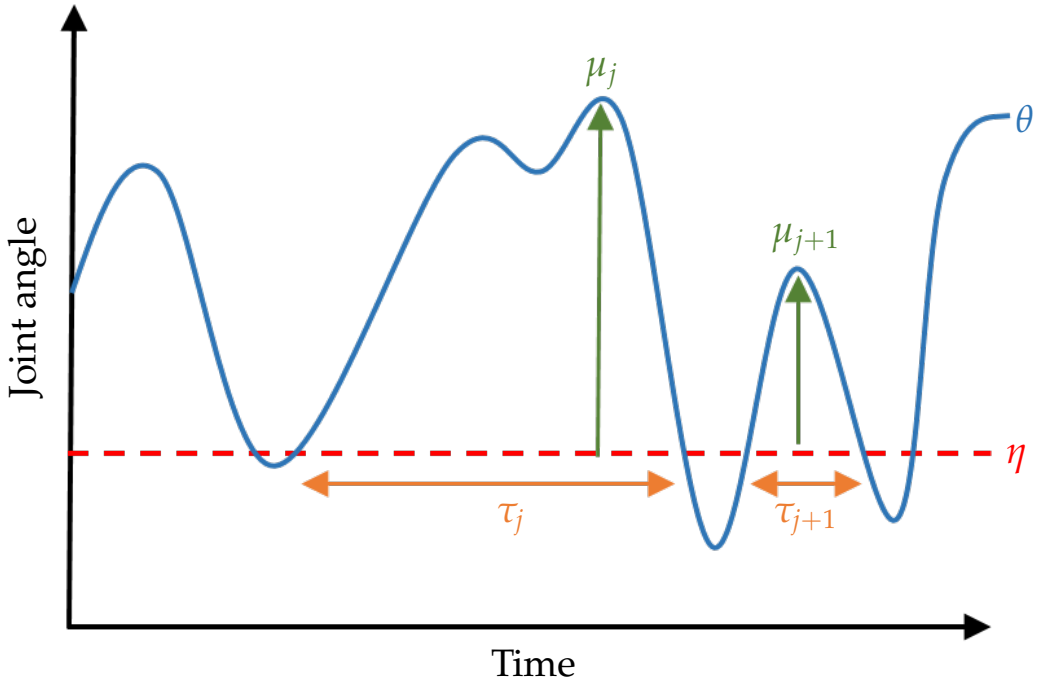

Figure 4-1: Representation of the joint deviation definition over example time-series joint angle data θ given neutral threshold η. Two valid joint deviations are shown, and their constituent magnitudes μ and durations τ are highlighted.

The neutral angular threshold η captures the undeviated (angular) position that a joint angle returns to in a cyclic task, i.e., a joint angle is considered deviated if $\theta > \eta$ and undeviated otherwise. In the case of non-cyclic motion, the concept of a joint deviation is not meaningful. This creates an important caveat: in order for a joint deviation δ to be captured under the aforementioned definition, a joint angle must first deviate, $\theta > \eta$,

but then *the joint must return to an undeviated configuration* $\theta \leq \eta$ before the deviation is considered complete. η is task-specific, as human kinematics will change across different tasks. Ideally, η would be defined *a priori* from operational knowledge, if it is known to what joint angle an operator is expected to return during a cyclic task. However, in practice, this approach is intractable—this *a priori* knowledge may not exist, different humans may perform the same task differently, or the same human may perform the same task with different technique over time or across environmental circumstances. For example, considering specifying the neutral threshold to which the human elbow flexion/extension angle returns during cyclic hammering of a nail: η likely depends on how far away the nail is from the person, or with how much force a person is hammering.

Therefore, it is proposed to take a metric-based approach to specifying η. One approach is to specify η as the value which maximizes the sum of the magnitudes of joint deviations δ:

$$\eta^* = \arg\max_{\eta} \sum_j f_m(\delta_j) \tag{4.2}$$

An interpretation for this approach is that Eq. 4.2 yields the value for η which maximizes (in an angular distance sense) the amount of cyclic motion captured in the proposed approach. This equation may be tractably solved through brute force search: loop over all possible values of η and choose the one which maximizes Eq. 4.2.

After determining η (Eq. 4.2), parsing the joint deviations, and determining each deviation's magnitude μ (Eq. 4.1) and duration τ, the distribution of joint deviation magnitudes and durations has been assessed.

4.4 Model of Suit Bearing Degradation

The IMU-derived human joint angle signal has additional applications toward understanding total rotation of hard suit bearing joints. From the discrete time-series human

joint angle θ, the (scalar) total angular distance traveled by a human joint Ψ_{human} may be computed:

$$\Psi_{\text{human}} = \sum_{i=1}^{N-1} |\theta_{i+1} - \theta_i| \tag{4.3}$$

In the standard case that a suit bearing is not oriented exactly in the plane of rotation of the joint, the bearing must rotate *more* in order to achieve the same articulation of the joint as measured by joint angle θ. A mathematical model is required to map total rotation of the human joint Ψ_{human} to the total rotation of its underlying bearing(s) Ψ_{bearing}, i.e., $\Psi_{\text{bearing}} = f_b(\Psi_{\text{human}})$.

According to Lundberg-Palmgren model of bearing fatigue [115, 116, 149], the bearing's dynamic load capacity C_D is a function of bearing geometry and material and is a property of a given bearing. Today, this concept is codified in ABMA/ANSI and ISO standards. C_D represents the constant equivalent load for which $L_{10} = 10^6$ revolutions. For ball diameters $d < 25.4$ mm, C_D (in Newtons) is empirically modeled as:

$$C_D = f_{cm}(i \cos\beta)^{0.7} Z^{2/3} d^{1.8} \tag{4.4}$$

where β is the bearing ball contact angle, Z is the number of balls in the bearing race, i is the number of rows of rolling elements, and d is the diameter of a single ball (in millimeters). Finally, f_{cm} is a coefficient which accounts for bearing material and configuration properties.

It is assumed that a bearing endures a constant load P_{eq}, the geometric sum of the radial and axial components of bearing load. Given P_{eq} and C_D from Eq. 4.4, a bearing's L_{10} life in millions of revolutions is modeled as:

$$L_{10} = \left(\frac{C_D}{P_{eq}}\right)^p \tag{4.5}$$

where the load-life exponent $p = 3$ for ball bearing [115] and $p = 10/3$ for roller

bearings [116].

Given total bearing rotation Ψ_{bearing} in radians achieved over total time T, the time on task for a bearing to achieve its L_{10} life may be determined:

$$\text{Time to } L_{10} = \frac{2 \cdot \pi \cdot 10^6 \cdot L_{10} \cdot T}{\Psi_{\text{bearing}}} \tag{4.6}$$

From this time to L_{10}, the allowable operational time (i.e., in number of EVAs) of a bearing can be estimated.

4.5 Methods

4.5.1 Experimental Methods

This study was performed in collaboration with the Scientific Physical and Operations Characterization (SPOC) project at NASA's Johnson Space Center (JSC). The protocol was reviewed and approved by both the University of Michigan (HUM00168276) and JSC (STUDY00000113). A single subject was equipped with IMUs (Opal IMU, APDM, Inc., Portland, OR, USA) on the feet, shanks, thighs, lower back, sternum, upper arms, lower arms, hands, and head (15 IMUs total). The IMUs contain dual 3-axis accelerometers ($\pm$16 g, $\pm$200 g), a 3-axis gyroscope ($\pm$2000 $^\circ$/s), and a 3-axis magnetometer ($\pm$8 Gauss), and were attached to the subject's limb segments using elastic straps. The subject (a trained geologist) performed a representative geological survey EVA in shirt-sleeve (i.e., no space suit) at the JSC rockyard, an outdoor training and science field site encompassing multiple analog environments. The data collection spanned four different regions within the rockyard: 1) the rock field, 2) the Martian mound, 3) the sand dunes, and 4) the Lunar surface. The participant progressed through these four areas in this order, spending approximately 20 minutes in each region for a total testing session time of about 90 minutes. Within each region, the participant completed geologically relevant fieldwork activities including

reconnaissance, sampling, documentation, as well as traversing uneven terrain and scaling rocky slopes [193].

4.5.2 Selected Bearing Model Parameters

The bearing model is applied to unsuited test subject data for demonstration purposes only, in lieu of taking IMU measurements of the suit directly. Three representative single-bearing suit joints are chosen to model space suit motion: one corresponding to flexion/extension of the knee, one corresponding to flexion/extension of the hip, and one corresponding to flexion/extension of the elbow. Each of the three joints is modeled as a bearing which rotates at a fixed ratio more than the underlying human skeletal angle (i.e., bearing ratio model f_b is linear). To select the bearing ratio, a conservative estimate was selected using data from Cullinane et al.[45]. They found a maximum bearing angular velocities during walking of about 180 °/s for the mid bearing of the Mark III spacesuit hip bearing assembly. If a subject walks at 1 Hz, with hip flexion cycles of 30° magnitude, then the hip articulates a total 60°/s during walking. Conservatively assuming the bearing angular velocity of 180°/s is constant, the bearing rotates 3 times more than the human hip per second. Therefore, a bearing ratio of 3 is chosen for this work. All 3 bearings are assumed to be deep-groove, single-row rolling ball bearings which bear a constant equivalent load. This equivalent load, as well as bearing geometry (i.e., number of balls and ball diameter) are taken from the tested hip bearing of the Z-2 Prototype Planetary Extravehicular Space Suit Assembly in Rhodes et al. [156]. The material and geometry coefficient f_{cm} is chosen as a conservative value (i.e., permits lowest dynamic load capacity) from standard ANSI/AMBA 9 [1], as presented in Zaretsky [208]. Relevant bearing model parameters are summarized in Table 4.1, and were used to determine bearing C_D and L_{10}.

Table 4.1: Assumed bearing geometry and loading parameters for all bearings (hip, knee, elbow) considered

Parameter	Value
Equivalent load, P_{eq}	1111 lbf
No. rolling balls per row, Z	142
Ball diameter, d	0.131 in
Contact angle, β	0 deg
No. rolling ball rows, i	1
Material and geometry coefficient, f_{cm}	60.71
Bearing ratio	3

4.5.3 Data Processing and Analysis

Data from the overall EVA task (5763 sec) is referred to as "SPOC dataset," and had two additional representative tasks extracted for analysis in this work: first, a 63 second long walking sample, chosen because it was the longest approximately-continuous walking sample in the data. Second, a 12 second long hammering task which occurred while the subject sampled a rock, chosen because it was the first hammering example in the data. Measured IMU data were recorded at 120 Hz. IMU data were processed for right knee and right hip flexion/extension angles according to McGrath and Stirling [127] with one major exception: as this study took place outdoors, magnetometer measurements were included to give IMU heading information. This heading information, combined with the diverse human kinematics of EVA, made it such that no calibration of the IMU system was needed. Right elbow flexion/extension angles were derived from IMU data according to Müller et al. [137]. Elbow angles were estimated at the full sampling rate of the IMU (120 Hz), however, knee and hip angles were estimated at a lower rate (12 Hz) as 10 IMU measurements were preintegrated between estimated keyframes following the selected

method. The right side of the body was chosen because the subject used the right hand for hammering. For the three analyzed tasks, only joints of interest were considered: all three joints were considered for the entire SPOC data, knee and hip were considered for walking, and elbow was considered for hammering.

The sign convention of the flexion/extension angles of the 3 joints are chosen so that 0 degrees represents standing neutral posture and positive angles represent the common deviation of the joint from standing neutral. This corresponds to flexion of all 3 joints. The hammering and walking tasks, as short constant tasks, are processed for a single neutral threshold η. The SPOC dataset (96 minutes long) was split into 500 equal length segments with η computed for each window, followed by a calculation of joint deviation durations and magnitudes.

Total joint rotation Ψ_{human} for each joint is found via Eq. 4.3. This value is multiplied by the constant bearing ratio to determine Ψ_{bearing}. Finally, from the total task time to achieve Ψ_{bearing}, the equivalent time to the bearing L_{10} is found from Eq. 4.6. For each of the 6 combinations of joints and tasks, time to L_{10} is reported both in hours and number of EVAs, assuming a single EVA is 8 hours long.

4.6 Results

The distributions of 500 values of neutral threshold η (Eq. 4.2) for each joint in the SPOC task are shown in Fig. 4-2. The [25^{th},75^{th}] percentiles of the hip [-13.9°,19.7°] and knee [-2.3°,13.6°] distributions lie near zero degrees, which is indicative of the subject spending most of their time deviating from a standing neutral posture. The distribution of η for the elbow, however, has a wider spread—a [25^{th},75^{th}] percentile of [19.2°,75.7°]. It is likely there existed a variety of elbow tasks that created a diverse set of underlying joint angle neutral baselines from which joint cycles occurred. Hammering and walking (each subset excerpts of the total SPOC trial) were each considered as a single task. The

hammering task assigned an optimal elbow neutral threshold η of 40.48°, which represents a neutral baseline which is moderately deviated from a straight elbow (i.e., zero degrees). This result highlights that for the current hammering task, the subject did not continuously return to a fully extended elbow during hammering cycles. For the walking task, results for the knee ($\eta = 0.10°$) and hip ($\eta = -12.40°$) suggest that the subject did return to a fully-extended knee and hip during walking joint cycles.

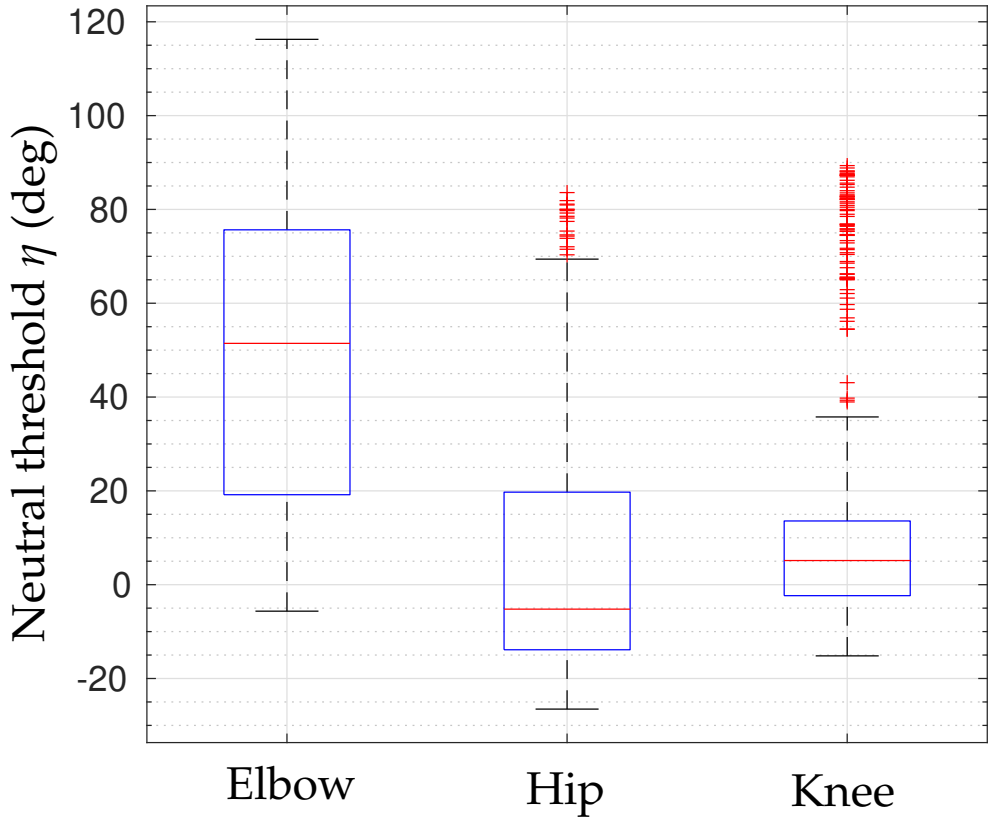

Figure 4-2: Distribution of 500 neutral threshold η values for each of the three joints analyzed in the SPOC dataset.

The distributions of joint deviation durations for each joint analyzed in the SPOC

dataset are shown in Fig. 4-3. Most deviation durations for all three joints are short. For elbow flexion/extension, 59.2% of durations are less than 1 second; 77.0% are less than 2 seconds. This type of right-skewed distribution is also seen for the knee (64.3% $<$ 1 sec., 83.4% $<$ 2 sec.) and hip (43.1% $<$ 1 sec., 73.4% $<$ 2 sec.).

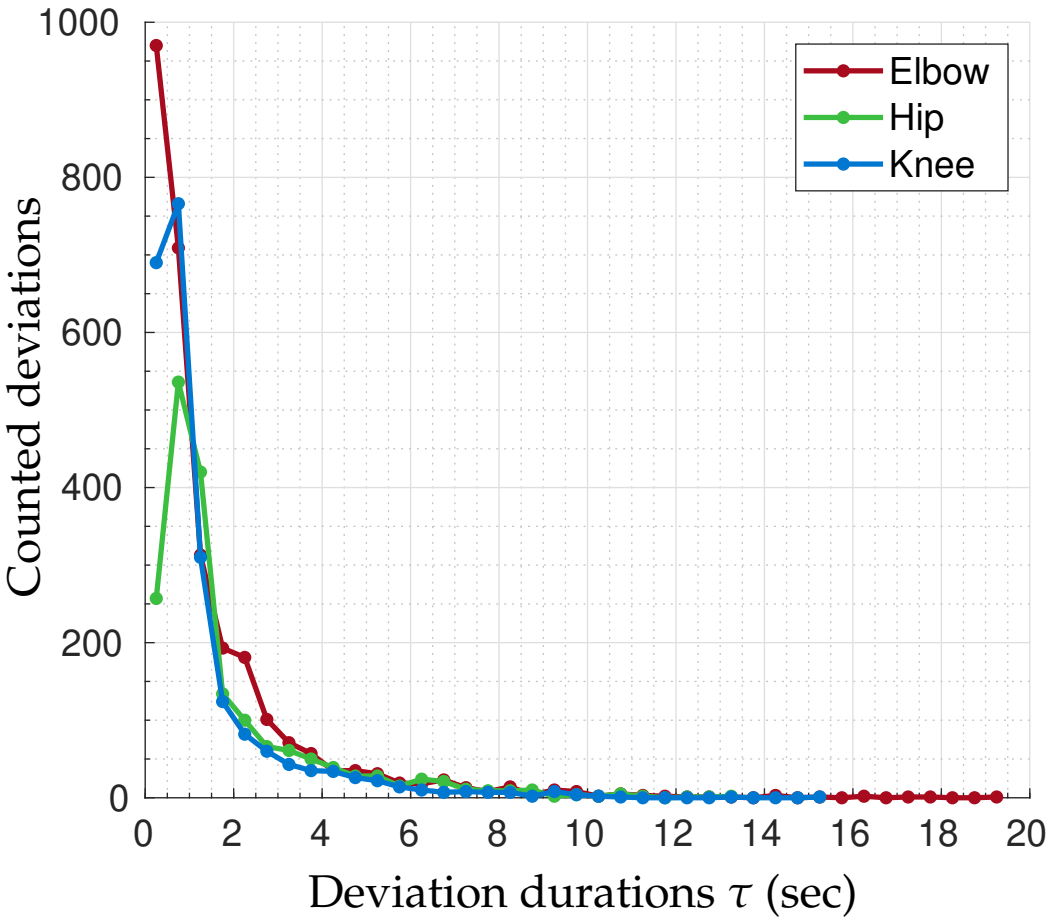

Figure 4-3: Distribution of joint deviation durations τ for all 3 joints considered in the SPOC dataset: elbow flexion/extension (total deviations $N = 2838$), hip flexion/extension ($N = 1840$), and knee flexion/extension ($N = 2270$). Each point represents the center of 0.5-second-wide bin.

The distributions of joint deviation magnitudes for each joint analyzed in the SPOC

dataset are shown in Fig. 4-4. For all three joints, very small deviations are the most common size. This result is expected—small, unintentional perturbations of a joint are seen in natural human kinematics. The elbow flexion/extension distribution shows decreasing presence of larger deviations. In contrast, a second mode is shown at larger magnitudes for the lower body joints—about 40° for the hip and 60° for the knee. Both of these modes correspond to typical peak hip (30°-35° [102]) and knee (63.6° $\pm$ 5.6° [96]) flexion angles during gait. This mode is likely emergent due to the relatively high representation of gait amongst all lower body kinematics in the geological survey task. If a motion was cyclic with constant amplitude, that would appear as a single spike with no spread. These distributions highlight the spread in joint deviation magnitude present in natural human kinematics. Visual observation suggested there was not a relationship between joint deviation magnitude and duration. In the observed natural human kinematics, there existed various combinations of short/long durations with small/large magnitudes.

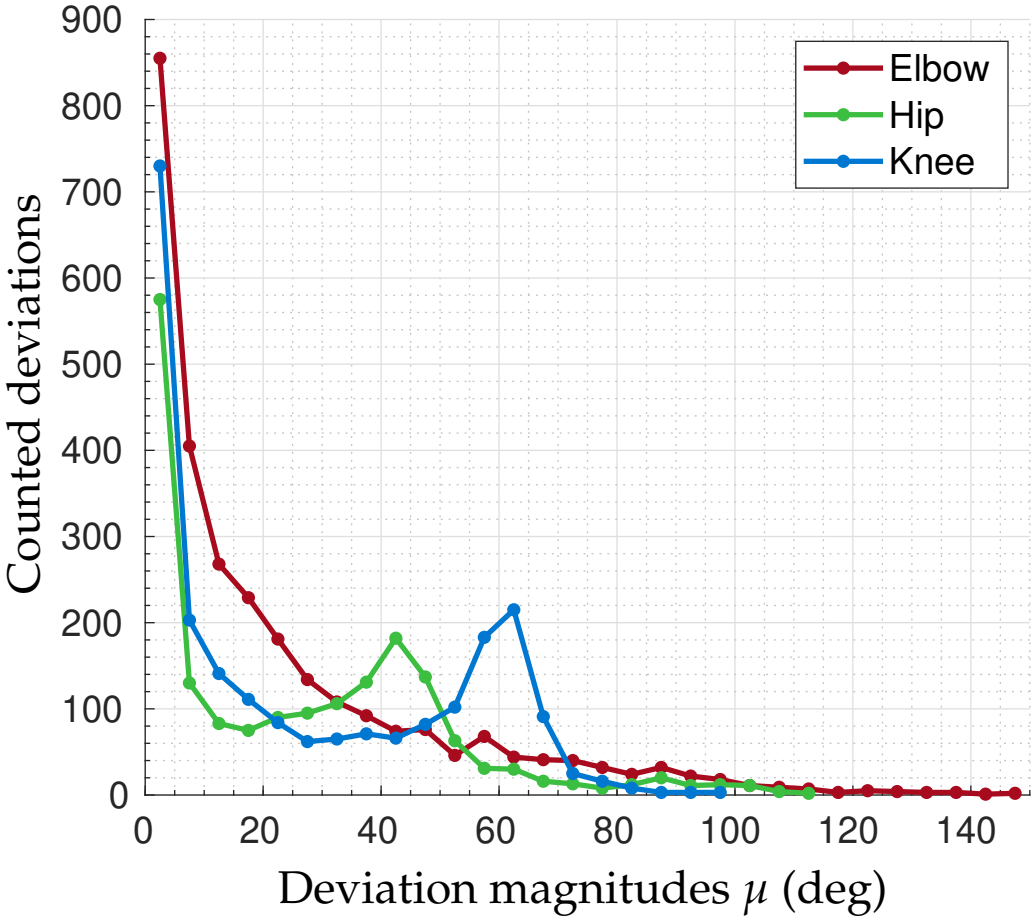

Figure 4-4: Distribution of joint deviation magnitudes μ for all 3 joints considered in the SPOC dataset: elbow flexion/extension, hip flexion/extension, and knee flexion/extension. Each point represents the center of a 5-degree-wide bin.

Due to the low number of samples of parsed joint deviations for the individual task examples (i.e., hammering and walking), a histogram is not shown. However, the cumulative distribution of joint deviations magnitudes are shown in Figs. 4-5a and 4-5b). The cumulative distribution for the SPOC dataset is also shown in Fig. 4-5c. If a motion was cyclic with constant amplitude, that would appear as a step function rising at the amplitude level. These cumulative distributions have been plotted over joint deviation

magnitudes in *descending* size with a reference deviations/hour vertical scale to enable operational interpretation of how many joint deviations per hour can be expected of *at least* a given deviation magnitude. This interpretation will be discussed further in Sec. 4.7. For the SPOC task with total duration 5763 seconds, the equivalent number of joint deviations per hour was 1772.8 dev/hour for elbow flexion/extension, 1154.4 dev/hour for hip flexion/extension, 1418.0 dev/hour for knee flexion/extension. These equivalent joint cycle rates are smaller for the SPOC dataset than the individual tasks (hammering elbow 3905.4 dev/hour, walking hip 2171.3 dev/hour, walking knee 2685.5 dev/hour).

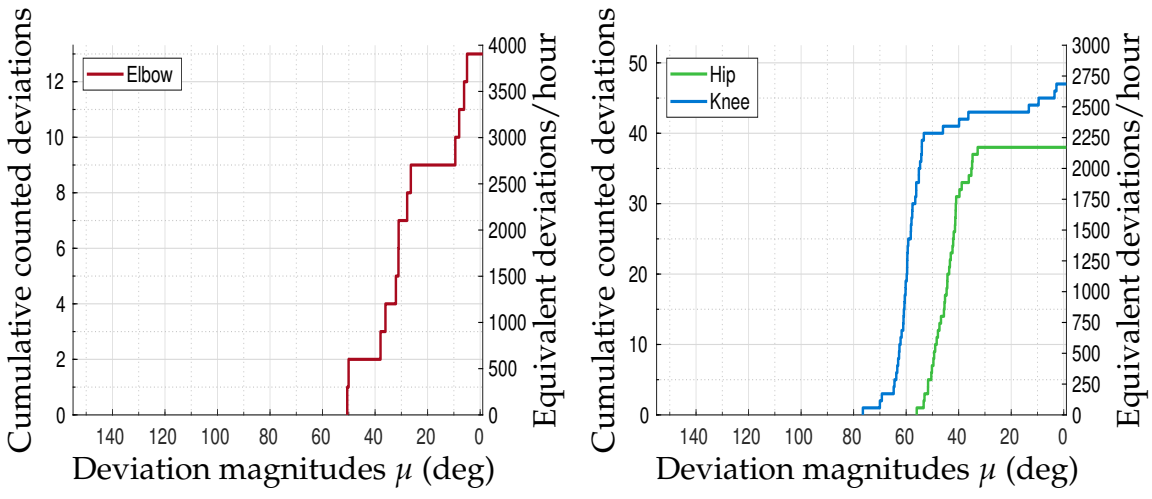

(a) Hammering task

(b) Walking task

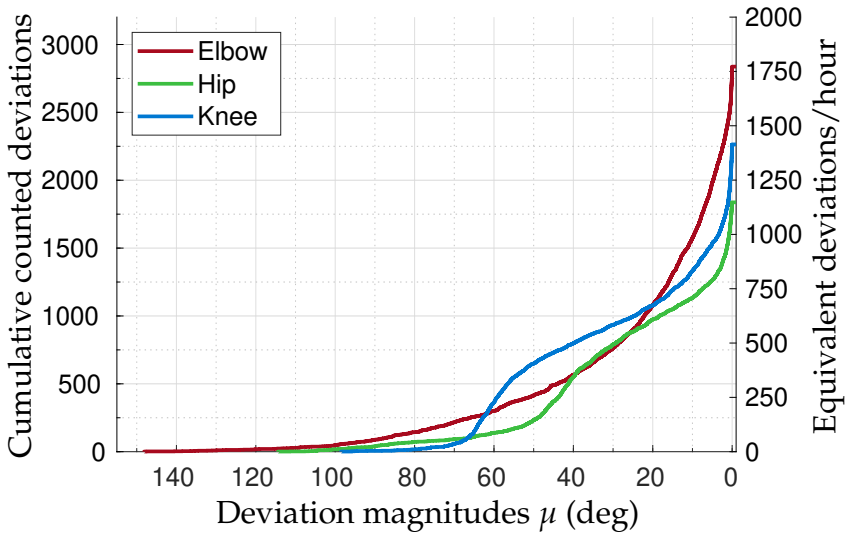

(c) Total SPOC trial

Figure 4-5: Cumulative counted deviation magnitudes in descending magnitude order for the three tasks considered, with each task's relevant joints plotted. A second reference right vertical axis has been added to display the equivalent deviations per hour (i.e., counted deviations divided by total task time). All 3 plots are scaled to have the same horizontal (deviation magnitude) and vertical (deviations per hour) scales. Joint angles labeled elbow, knee, and hip refer to flexion/extension of that joint. The representative tasks of hammering (a) and walking (b) are subset excerpts of the total SPOC trial (c).

Table 4.2: Results of human kinematics processing and mapping to bearing degradation model. T is total measured task time in seconds, Ψ_{human} and Ψ_{bearing} are measured total joint rotation (Eq. 4.3) and equivalent bearing rotation respectively, both in radians. Computed bearing $C_D = 14384.94$ N (Eq. 4.4), $L_{10} = 24.66E6$ revolutions (Eq. 4.5) for all bearings. Time to L_{10} (Eq. 4.6) is reported in both hours and number of EVAs. 1 EVA is assumed to be 8 hours long. Number of EVAs are rounded down to nearest whole number.

Joint	Task	T (s)	Ψ_{human} (rad)	Ψ_{bearing} (rad)	Time to L_{10} (hr)	Time to L_{10} (EVAs)
RKnee	Walk	62.99	98.9	296.6	9139.9	1142
RHip	Walk	62.99	79.1	237.3	11425.5	1428
RElbow	Hammer	11.98	20.5	61.6	8372.4	1046
RKnee	SPOC	5763.17	2640.0	7920.0	31321.0	3915
RHip	SPOC	5763.17	1994.6	5983.7	41456.6	5182
RElbow	SPOC	5763.17	3394.4	10183.1	24360.2	3045

The IMU-measured human kinematics were processed for total human joint rotation Ψ_{human} and equivalent bearing rotation Ψ_{bearing}. These data were used as inputs to model time to bearing L_{10} in both hours (Eq. 4.6) and number of EVAs (Table 4.2). Results suggest that a very large operational time (tens of thousands of hours) may be performed before a suit bearing reaches its L_{10} lifespan. More total rotation per unit time (i.e., Ψ_{human}/T) is observed in the individual tasks of walking and hammering vs. the full SPOC terrestrial fieldwork EVA. As a result, time to L_{10} is longer for the realistic SPOC fieldwork trial.

4.7 Discussion

The first aim of this work is to demonstrate the usage of body-worn IMUs to motivate an operationally-relevant definition of human deviation which informs suit requirements

definition. The proposed definition allows for the assessment of joint deviations across different joint cycle baseline references (i.e., neutral thresholds η). This capability is useful for evaluating natural human kinematics where human technique may change within or across tasks.

The distributions of joint deviation magnitudes shown in Fig. 4-4 suggest that there is large non-normal spread in the magnitude of deviation during natural human kinematics. While certain modes may emerge (e.g., gait for the lower body joints) depending on relative proportion of tasks, these emergent modes do not diminish the importance of considering the entire distribution. Operationally, this may suggest that specified requirements related to joint cycle magnitudes (and subsequent test protocols) are *not* adequately specified by a single scalar value. Additionally, the distributions of joint deviation magnitudes for the SPOC task in Figs. 4-4 and 4-5c offer insight to the counted number of joint cycles over time. The equivalent number of joint deviations per hour noted in Sec. 4.6 can be compared against previous literature. Reinhardt and Magistad [155] suggest that the AX-5 suit was designed to a requirement of 84.7 elbow joint cycles per hour and 19.8 knee joint cycles per hour. These are orders of magnitude smaller than the counted number of joint deviations per hour found in the current terrestrial fieldwork geological survey task. The current analysis found 21 and 72 times more joint deviations per hour for the elbow and knee, respectively, than the historical AX-5 requirements.

Of course, many counted deviations in the current work were very small in magnitude. As an alternate perspective, we may order the deviations in descending magnitude (i.e., Fig. 4-5) and consider what the *smallest* deviation magnitude is which is captured by the joint cycles per hour requirement. Example for the knee: the AX-5 joint cycles/hour requirement of 19.8 represents the 1.39^{th} percentile of the 1418.0 knee joint cycles/hour observed in the SPOC geological survey task. The (100-1.39)=98.6^{th} percentile of knee deviation magnitudes is equivalent to 75.8°. (Note: this analysis could also be read from Fig. 4-5c by finding what level of knee joint deviation magnitude corresponds to 19.8 joint

deviations/hour.) It could then be concluded that the AX-5 suit 19.8 knee joint cycles per hour requirement applied to the current data would only capture knee deviations *larger* in magnitude than 75.8°. This is very large, and would not even capture typical knee flexion angle during walking (63.6° ± 5.6° [96])—a task which was heavily represented in the current SPOC dataset. An equivalent perspective for the elbow suggests that the AX-5 suit 84.7 elbow joint cycles per hour would only capture deviations which are larger than 81.3°. This perspective highlights that questions related to *how many* joint cycles per hour occur in a suit are inherently related to the level of joint deviation magnitude that the domain expert considers to be operationally-relevant. For example, if a suit is intended to enable natural unsuited ambulation characteristics, requirements should at least comfortably capture knee deviation magnitudes that are typical of gait.

Furthermore, understanding of the constituent magnitudes and relative occurrences of joint deviations used to complete a task may have implications for human performance. Using the estimated joint angles as inputs to musculoskeletal models, it would also be possible to estimate the metabolic cost of swinging weighted tools. Tool usage strategies may be optimized for minimizing metabolic cost, peak joint torque, time required to complete the task, or a number of other cost functions.

It should be noted that this definition of joint deviation was not validated for a particular task with work domain experts in this work. Domain experts (e.g., suit engineers) can support selecting the regions of the plot (Figs. 4-4 and 4-5) or values of the neutral threshold η that are relevant for a given task. This definition of joint deviation (and deviation magnitude and duration) may be relevant to other ergonomics fields as well, where further validation by domain experts would also be required. The concept of duration exists in occupational ergonomics, but may take multiple meanings, for example: global task duration (e.g., Winkel and Mathiassen [196]), time spent in categorized postures (e.g., Arias et al. [13]), or subtask action cycle duration (e.g., the ULRA method [159, 160]). The proposed definition of duration is more consistent with the latter definition.

The proposed approach used a constant neutral threshold η to represent the angular setpoint that a joint returns to while completing cyclic motion. This assumption may not apply if the return setpoint in cyclic motion significantly varies, however, this approach does capture performing the same task with different form. For example, the analyzed hammering task in the results (11.98 sec long) assigned an optimal η from Eq. 4.2 of 40.48°. However, two other hammering samples from the SPOC data (9.48 and 4.98 sec long) returned optimal η of 19.26° and 21.45° from full elbow extension. This difference in η across hammering task samples suggests that the subject did not return to the same point while hammering across different instances. These differences in form may be driven by the force used during hammering, subject body posture, or distance from the subject to the hammering impact point.

The second aim of this work is to demonstrate the usage of body-worn IMUs to motivate a suit bearing degradation model based on Lundberg-Palmgren theory. Results of the bearing fatigue model suggests that a very large operational time (tens of thousands of hours) would be required for a suit bearing to achieve its L_{10} life. This result is expected, as bearings are typically manufactured for higher-frequency, higher-loading applications than the space suit use case. The long suit bearing fatigue life is likely consistent with current expectations, however, offers a new perspective for how to calculate the expected total rotation of the bearing from IMU data. Results also suggest that there is a larger time to L_{10} for realistic EVA data (i.e., SPOC), rather than the active task examples (walking and hammering). This result is also expected—in realistic EVA scenarios the operator is likely not kinematically active all the time. These periods of little kinematics, such as standing for a break or recording field notes, lower the total number of joint deviations (i.e., the y-axis of Fig. 4-5). Therefore, the total time to bearing L_{10} is longer. This phenomenon also explains why equivalent number of deviations per hour is larger for individual tasks (hammering, walking) than the SPOC data. Furthermore, in the SPOC data, the largest total rotation was shown in elbow flexion/extension while hip flexion/extension rotated

least (see Ψ_{bearing} in Table 4.2). This difference in total rotation across joints may be due to naturally different rotation levels across joints or may indicate a proportionately larger presence of upper body tasks in the geological survey.

The current bearing geometry and loading model has multiple nuances. The assumed constant equivalent load of 1111 lbf is likely conservative (i.e., higher than operational loading). However, this bearing model is non-conservative in many other ways. This model *only* captures fatigue due to total rotation of the joint. It does not capture non-mechanical fatigue (i.e., thermal, pressure) or mechanical fatigue due kinematics outside of the operational tasks (i.e., donning/doffing the suit, suit motion in shipping). Moreover, the assumed constant 3:1 bearing-to-human rotation ratio is also an oversimplification of actual suit bearing rotation. Therefore, the results of Table 4.2 are only representative of how the IMU-derived kinematics may be used—they are not meant to be taken as engineering recommendations for any current or previous suit.

4.8 Limitations and Future Work

The current study measured IMU-based human kinematics in an analog shirt-sleeved terrestrial fieldwork EVA. The same approaches could extend to the suit if the suit were equipped with IMUs on the rigid body segments. The current definition of joint deviation (and related concepts of joint deviation magnitude, duration, and neutral threshold) requires further validation in operationally-relevant environments by subject matter experts (e.g., suit engineers). A validated, standardized definition of joint deviation within the bioastronautics community may inform future work in a number of human health and performance related questions, including: injury risk assessment (both suited and unsuited), suit range of motion, suit mobility evaluation, and operator physical workload modeling. Additionally, the proposed definition of joint deviation models joint cycle kinematics as deviation from a neutral (undeviated) threshold η. It is proposed to define or derive (e.g.,

Eq. 4.2) η on a per-task basis. However, in the current 96-minute-long SPOC study, individual tasks were not parsed due to practical time constraints. Future work may consider automatic task parsing approaches to better support the selection of η.

The presented bearing model is very simplified, accounting for only fatigue wear due to total rotation of the bearing during operational tasks. Moreover, this model considers no additional fatigue due to the bearing changing direction, i.e., all equivalent rotation of the bearing due to joint motion is considered to be in the same direction for the purpose of using Lundberg-Palmgren. In this study, IMUs measured human kinematics and suit bearing rotation was assumed at a 3:1 constant ratio to human joint rotation. In reality, suit bearing rotations have a complex relationship with underlying skeletal kinematics and a more appropriate mathematical model should be used. Alternatively, if IMUs were placed directly on the bearings, total bearing rotation Ψ_{bearing} could be measured directly rather than extrapolated from human joint rotation. Future work should consider modeling non-constant loading of the bearing and differing bearing geometries and assembly configurations. In addition to expanding the model to include degradation due to other factors (e.g., thermal, pressure), an expanded model should consider which failure criteria are relevant to EVA operations. For example, the current model is based on a bearing's L_{10} life, the point where 10% of bearings will have shown signs of mechanical fatigue. However, this number may not be conservative enough for mission critical operations or not use an operationally-relevant definition of bearing failure. The presented bearing failure model also does not include bearing wear due to, e.g., donning/doffing of the suit. The proportion of time spent in mission operations vs. suit maintenance and setup operations like donning/doffing will also change depending on mission profile.

If IMUs were designed into the suit, these approaches could be automated so that a suit may keep track of its own expected bearing wear in real time, allowing for more precise maintenance scheduling. This approach of modeling total kinematic rotation towards calculating expected bearing wear may have application to other bearing devices, like

exoskeletons, or non-bearing joint devices which fatigue over time as a function of total rotation or number of joints cycles, such as prosthetic joints or space suit soft-goods joints.

4.9 Conclusion

The current work demonstrates the usage of body-worn IMUs to evaluate human and/or suit kinematics in relevant environments. A definition of joint deviation (with related concepts of joint deviation magnitude and duration) has been proposed to support the automatic parsing and counting of relevant deviations using IMUs. The further use of body-worn IMUs measurements to assess suit joint bearing degradation was shown through an example model of suit bearing lifespan based on Lundberg-Palmgren theory. Both of the proposed concepts are demonstrated for a single subject outfitted with multiple IMUs performing a terrestrial geological survey task (96 minutes long). This IMU-measured human kinematics data is additionally mapped to virtual suit bearing rotations as an analog to taking the IMU measurements from an actual suit. Results suggest that natural human kinematics are composed of a diverse non-normal distribution of different joint deviation magnitudes and durations, although common modes may emerge depending on task composition in the EVA. Engineers should consider what level of joint deviation magnitude is relevant on a mission-specific basis. However, historical AX-5 suit elbow and knee joint cycles/hour requirements would have significantly underestimated the number of joint deviations found in terrestrial fieldwork. Processed results of the example bearing model suggest that a very long operational time (thousands of EVAs) would be required for suit bearings to reach their lifespan due to rolling element mechanical fatigue for a fieldwork-type mission. Additional work is needed to validate the proposed joint deviation definition in operationally-relevant environments with domain experts (e.g., suit engineers), as well as determining appropriate bearing models which account for all sources of degradation. The use of wearable IMUs has the potential to provide new

information for assessing both the operator and the suit through informing physical work demands, mobility requirements, and operations planning.

Chapter 5

Conclusions and Future Work

The goal of this work was to advance the current state-of-the-art in IMU-based human pose estimation and propose operationally-relevant outcomes for space suit design and operations. We set out to address the following research questions:

1. Can we develop a self-calibrating IMU approach for the human lower body which is accurate in both joint angle estimation and IMU pose estimation?
2. Can these IMU-based approaches provide operationally-relevant measurements for the design and testing of space suits?

In this thesis, these research questions were addressed through the following specific aims:

1. Estimate the human knee flexion/extension angle in gait through the development of a novel human-knee kinematic model for IMU-based knee pose estimation which is agnostic to placement of IMUs on the leg.
2. Develop a self-calibrating optimization-based smoothing approach to the IMU-based human lower-body pose estimation problem which models human kinematics and anthropometry, and

(a) maintains IMU pitch/roll estimation accuracy vs. a single-IMU smoothing approach,

(b) provides accurate estimation of knee (flexion/extension) and hip (flexion/extension, internal/external rotation, abduction/adduction) angles reported in ISB convention,

(c) and demonstrates the reduction of relative IMU position drift between adjacent IMUs.

3. Propose and demonstrate

(a) a metric of IMU-derived human joint deviation with application to space suit requirements specification

(b) and the use of IMU data to inform a representative model of expected suit bearing rotation and lifespan estimation,

both assessed for an unsuited analog EVA geological survey task.

The first aim was addressed in Chapter 2 with the development of a knee flexion/extension axis estimator based on principal component analysis (PCA). This novel model of hinge kinematics was used in a larger lower-body, optimization-based smoothing approach in Chapter 3 to address the second aim. The final aim was then addressed in Chapter 4, where the work detailed in Chapters 2 and 3 was applied in to propose an operational definition of human joint deviation and a space suit bearing degradation model.

5.1 Summary of Results

This section summarizes the main results from each of the chapters of this thesis. Section 5.2 presents the major contributions to the existing literature.

5.1.1 A Self-Calibrating Knee Flexion-Extension Axis Estimator using Principal Component Analysis with Inertial Sensors

Chapter 2 developed a novel kinematic model of single-DOF hinge joint motion, based on the concept of relative angular velocity across a hinge joint (Eq. 2.1). The kinematic model for a 1DOF hinge joint is a simplification of the 2 DOF elbow joint presented by Müller et al. [137]. A powerful result follows: in the case of a 1 DOF joint, finding the maximum likelihood hinge axis simplifies to finding the best-fit axis over the set of relative angular velocity vectors. Therefore, unlike the 2 DOF elbow problem, an iterative approach is not necessary—the problem can be solved efficiently using PCA. The estimated knee axis (along with an assumed-proximal vector) is then used to calculate the knee's flexion/extension angle according to ISB convention [75] and compared against an OMC reference for a short walking task. Due to large orientation estimation error in the manufacturer's orientation filter, the method is shown for both measured IMU data and simulated IMU data from the mocap markers. The method is also compared against a popular state-of-the-art self-calibrating approach, Seel et al. [170]. Results highlight that this approach is of similar accuracy to existing methods, while being much faster to solve. Additionally, this method was validated against a larger subject set ($N = 15$), allowing variability across subjects to be characterized. A post-hoc explanatory model of method error suggests that error is a function of thigh IMU circumferential motion and accuracy of knee flexion/extension hinge axis estimation—highlighting the importance of axis estimation to calculation of knee angle under ISB angle conventions. However, these sources of error were likely small compared to potential gains through increased IMU orientation estimation accuracy.

5.1.2 Body-Worn IMU Human Skeletal Pose Estimation using a Factor Graph Based Optimization Framework

Chapter 3 developed a human lower-body kinematics estimation methodology without the use of magnetometers. The maximum a posteriori estimation problem is modeled graphically as a factor graph and solved via nonlinear least-squares optimization techniques. The model proposed a number of novelties to the literature, including: reformulating the knee hinge model from Chapter 2 for least-squares optimization, inclusion of anthropometric priors from population data, segment length discrepancy, the relationship between the knee's hinge axis and femur/tibia proximal and segment direction. This work was built on top of a state-of-the-art IMU pose estimation framework [70]. It was found that pure walking kinematics alone is not enough to calibrate the system. So, additionally a calibration task was used to set priors on variables which were unidentifiable under walking alone. The proposed method was evaluated for both the walking and calibration tasks against an OMC reference. Accuracy of derived joint angles without magnetometers for knee flexion/extension, hip flexion/extension, and hip abduction/adduction are similar to current state-of-the-art with magnetometer use (RMSE 3°–7°). Hip internal/external rotation accuracy is task-dependent and subject to unobservability for certain tasks. Additional results suggest that the proposed method maintains IMU pitch/roll estimation accuracy and also effectively constrains distance relationships between adjacent IMUs. A discussion of system identifiability is provided, and the impact of soft tissue artifacts on knee flexion/extension angle accuracy is shown.

5.1.3 Application of Human-Body Worn IMUs to Space Suit Requirements and Testing Protocol Development

Chapter 4 applied the IMU-based skeletal pose estimation techniques of Chapters 2 and 3 to two practical problems. First, an operational definition of joint deviation was proposed to inform future space suit requirements definition. This definition was used to characterize human kinematics in an analog EVA geological survey environment. Results suggest that human kinematics in real environments are a complex combination of high-magnitude, low-frequency motions and low-magnitude, high-frequency motions. This combination of motions may not be captured by current space suit requirements and testing protocols, and engineers should consider the relevance of different motion paradigms to design and evaluation of the space suit. Second, this chapter proposed a method to evaluate total space suit bearing rotation over time, applying this model within the Lundberg-Palmgren framework of modeling rolling bearing fatigue. Results suggest that suits are unlikely to fail due to mechanical degradation of the bearings due to total rotation. However, this approach did not account for many other forms of bearing wear—pressure cycling, thermal cycling, donning/doffing the suit, debris, etc. Engineers should consider using IMU-derived measures and models to inform suit bearing degradation, of which the proposed bearing fatigue model is one example. Any future model of bearing fatigue should account for other environmental and fatigue factors in order to best make informed operational decisions about design and testing of the space suit bearing joints. The proposed IMU-enabled bearing fatigue model also has the potential to become an online, in-suit approach to have the suit self-monitor its own bearing mileage.

5.2 Contributions to Literature

This thesis makes several contributions to the existing literature on IMU-based human kinematics estimation, occupational ergonomics, and extravehicular operations.

1. A novel kinematic model of a 1 DOF hinge joint (e.g., the human knee) based on the relative angular velocity across the joint was proposed.

2. An estimator of the knee's static hinge axis based on the aforementioned hinge model and principal component analysis (PCA) was developed. This PCA-based approach is faster than previous iterative approaches.

3. This estimation approach was validated against a larger set of subjects than previous works. A post-hoc explanatory model of method error is developed, and potential sources of error as well as inter-subject variability are shown.

4. A lower-body skeletal pose estimation technique was developed without the use of magnetometers which offers a number of modeling advances over existing literature, such as anthropometric modeling of segment length, segment length discrepancy, and the angular relationship between the knee hinge's axis and the femur/tibia orientation.

5. A discussion of identifiability, as well as the properties of ideal kinematic hinges, for the proposed kinematic hinge model was provided. This discussion details design criteria for calibration motions which most accurately calibrate 1DOF hinge systems.

6. The impact of soft tissue artifacts on knee flexion/extension angle accuracy during gait was demonstrated. It was shown that, relative to an optical mocap reference, IMU-derived knee angles may underestimate the mocap knee angle during swing phase, and may overestimate during stance.

7. An operational definition of *joint deviation* was proposed for the purpose of space suit requirements specification and assessment of human kinematics for extravehicular activity.

8. The use of IMU data to inform a model which maps human kinematics to degradation of suit hard joint bearings was shown. This model was used to provide a practical methodology for predicting bearing wear.

5.3 Applications and Future Work

This thesis sought to advance the current state-of-the-art in IMU-based human motion capture as well as provide a practical application of such a system to extravehicular operations. However, there are other practical applications of this system to other fields. Additionally, there are other advanced modeling approaches which could be made to increase system accuracy and usability. We now present some of these modeling extensions and propose new research directions.

5.3.1 Additional Advances in IMU-Based Human Pose Estimation

Chapter 3 presents a lower-body human pose estimator based on IMUs placed on the lumbar, thighs, shanks, and feet. That work presents a number of novel modeling approaches and leverages a state-of-the-art IMU estimation technique. A number of advanced modeling approaches could be added to this work—some existing elsewhere in the literature and some currently unexplored. The IMU-to-segment assignment problem has been approached through deep learning techniques [215], but could possibly be cast as a probability maximization problem and included in the work of Chapter 3. Additionally, foot ground-contact estimation (e.g., Miezal et al. [130]) has the potential to include useful

external information into the problem to aid observability and reduce position bias drift. This approach could additionally be modeled using switchable constraints [180] to robustly model the effect on the foot's pose when in contact with the ground. In the presented work, variables representing the knee's hinge axis and positional relationship to adjacent joint centers were assumed to be static. It may be possible to robustly model a bias parameter on these variables to represent perturbation due to soft tissue noise.

Additional work could also expand the proposed model to include upper body kinematics. For example, the Müller method [137] for elbow kinematics estimation can be cast as a factor graph and included in the proposed model. Future work should consider novel models of the scapula and spinal kinematics: two joints which have been difficult to robustly model and estimate solely from surface-mounted IMUs.

As IMUs and cameras have become smaller, there will likely be a point where it is tractable to include a camera on the external surface of the strap-on IMU. At this point, full visual-inertial SLAM can be performed in a multi-IMU system to robustly and accurately estimate IMU pose as well as map the environment around the human.

5.3.2 Soft Tissue Modeling

In this work, and most works, the human body is modeled as a rigid body. This is strictly untrue, as soft tissue artifacts affect any surface-mounted devices—both IMUs and optical motion capture markers. Many works include a noise parameter to account for this (e.g., the I2S noise distribution). However, future work may seek to model the dynamics of soft tissue in an attempt to more robustly capture this noise within the model. Unfortunately, these soft tissue artifacts also affect optical motion capture references, which most IMU-based works are evaluated against. Validating a model of soft tissue noise will likely require X-Ray imaging to estimate the underlying bone segment poses.

5.3.3 Automated Methods in Occupational Ergonomics

Chapter 4 proposed an operational definition of human joint deviation with application to evaluating human kinematics in extravehicular activity. As discussed in 4.2, with few exceptions, IMU-based ergonomics necessarily rely on operational ergonomics definitions which were intended for visual observation. This represents a limitation in the current ergonomics literature—modern measurement approaches like IMUs can create high-frequency accurate measurements. New ergonomics definitions should be proposed and assessed in operational environments and validated against expert-assessed visual observation approaches. In particular, the proposed human deviation definition of Chapter 4 may offer a useful definition for other work environments, but requires further validation.

5.3.4 On-Board Human/Suit Kinematics Monitoring

The combined work of this thesis presents a multiple-IMU-based system which could be embedded into the space suit (or placed on the human inside the suit) to monitor human/suit kinematics. These monitored kinematics can inform a host of relevant decisions, including human workload management, consumables sizing and administration, and suit maintenance due to wear. Future EVAs will need to be more autonomous: they will occur on extraplanetary bodies with larger communication delay and further away from base stations than previously. Creating autonomous systems within the suit as a decision aid for operational decision making could create safer, more efficient EVAs as humanity seeks to explore the stars.

5.4 Concluding Remarks

This thesis offers advances and practical applications for the use of body-worn IMUs to estimate human skeletal pose. The ability to measure human kinematics accurately

in the field with minimal calibration provides opportunity to better quantify human performance and monitor human health. It is our hope that the scientific and engineering community can build upon these algorithms to create more accurate, more efficient, and more robust estimation approaches. The application of these algorithms will only come through collaboration with experts in the field—clinicians, operational engineers, coaches, etc. The use of body-worn IMUs is only as practical as they are accurate, robust, and able to provide the information relevant to end users. We recommend the adoption of body-worn IMUs in fields where human motion is important in decision making, but more importantly, we recommend the collaboration necessary to make the technology useful. Properly applied, this technology can provide subject matter experts a critical decision aid to make humans healthier, safer, and more productive.

Bibliography

[1] ABMA 9: Load Ratings and Fatigue Life for Ball Bearings. *American Bearing Manufacturers Association*, Washington.

[2] Andrew F J Abercromby, J Scott Cupples, Sudhakar Rajulu, Jesse A Buffington, Jason R Norcross, Steven P Chappell, Wyle Science, and Engineering Group. Integrated Extravehicular Activity Human Research Plan: 2016. *46th International Conference on Environmental Systems*, 2016.

[3] Lukas Adamowicz, Reed Gurchiek, Jonathan Ferri, Anna Ursiny, Niccolo Fiorentino, and Ryan McGinnis. Validation of Novel Relative Orientation and Inertial Sensor-to-Segment Alignment Algorithms for Estimating 3D Hip Joint Angles. *Sensors*, 19(23):5143, nov 2019.

[4] Norhafizan Ahmad, Raja Ariffin Raja Ghazilla, Nazirah M. Khairi, and Vijayabaskar Kasi. Reviews on Various Inertial Measurement Unit (IMU) Sensor Applications. *International Journal of Signal Processing Systems*, 2013.

[5] David L Akin. Revisiting the Mark III/AX-5 Suit "Fly-Off": Lessons Learned Applicable to Modern-Day Suits. In *International Conference on Environmental Systems*, number July, pages 1–30, 2019.

[6] David J. Allerton and Huamin Jia. A review of multisensor fusion methodologies for aircraft navigation systems, 2005.

[7] A Anderson, A Hilbert, P Bertrand, S Mcfarland, D J Newman, Biomechanics Facility, Ventilation Garment, Master Candidate, and Master Candidate. In-Suit Sensor Systems for Characterizing Human-Space Suit Interaction. *International Conference on Environmental Systems*, 2014.

[8] Allison P. Anderson, Dava J. Newman, and Roy E. Welsch. Statistical Evaluation of Causal Factors Associated with Astronaut Shoulder Injury in Space Suits. *Aerospace Medicine and Human Performance*, 2015.

[9] Allison Paige Anderson. *Understanding human-space suit interaction to prevent injury during extravehicular activity*. PhD thesis, Massachusetts Institute of Technology, 2014.

[10] F. C. Anderson and M. G. Pandy. Dynamic optimization of human walking. *Journal of Biomechanical Engineering*, 2001.

[11] Frank C. Anderson and Marcus G. Pandy. A dynamic optimization solution for vertical jumping in three dimensions. *Computer Methods in Biomechanics and Biomedical Engineering*, 1999.

[12] Oscar E. Arias, Peter E. Umukoro, Sonja Stofell, Jack T. Dennerlein, and Glorian Sorensen. Association between trunk flexion and physical activity in Patient Care Unit workers. In *Proceedings of the Human Factors and Ergonomics Society*, 2012.

[13] Oscar E. Arias, Peter E. Umukoro, Sonja D. Stoffel, Karen Hopcia, Glorian Sorensen, and Jack T. Dennerlein. Associations between trunk flexion and physical activity of patient care workers for a single shift: A pilot study. *Work*, 2017.

[14] Richard C De Baca, Alfredo Juarez, Evaluation Contract, White Sands, Test Facility, Las Cruces, Stephen Peralta, Jonathan Tylka, Las Cruces, Richard Rhodes, Mechanical Engineer, Las Cruces, Mechanical Engineer, and Las Cruces. Failure Simulation Testing of the Z-1 Spacesuit Titanium Bearing Assemblies. (July):1–13, 2016.

[15] Saba Bakhshi, Mohammad H. Mahoor, and Bradley S. Davidson. Development of a body joint angle measurement system using IMU sensors. In *Proceedings of the Annual International Conference of the IEEE Engineering in Medicine and Biology Society, EMBS*, 2011.

[16] Sergi Barrantes, Antonio J. Sánchez Egea, Hernán A. González Rojas, Maria J. Martí, Yaroslau Compta, Francesc Valldeoriola, Ester Simo Mezquita, Eduard Tolosa, and Josep Valls-Solè. Differential diagnosis between Parkinson's disease and essential tremor using the smartphone's accelerometer. *PLoS ONE*, 2017.

[17] Arnaud Barré, Jean Philippe Thiran, Brigitte M. Jolles, Nicolas Theumann, and Kamiar Aminian. Soft tissue artifact assessment during treadmill walking in subjects with total knee arthroplasty. *IEEE Transactions on Biomedical Engineering*, 60(11):3131–3140, 2013.

[18] Akram Bayat, Marc Pomplun, and Due A. Tran. A study on human activity recognition using accelerometer data from smartphones. In *Procedia Computer Science*, 2014.

[19] Kara H. Beaton, Steven P. Chappell, Andrew F.J. Abercromby, Matthew J. Miller, Shannon E. Kobs Nawotniak, Allyson L. Brady, Adam H. Stevens, Samuel J. Payler, Scott S. Hughes, and Darlene S.S. Lim. Using Science-Driven Analog Research to Investigate Extravehicular Activity Science Operations Concepts and Capabilities for Human Planetary Exploration. *Astrobiology*, 2019.

[20] Elena Bergamini, Marco Iosa, Valeria Belluscio, Giovanni Morone, Marco Tramontano, and Giuseppe Vannozzi. Multi-sensor assessment of dynamic balance during gait in patients with subacute stroke. *Journal of Biomechanics*, 2017.

[21] Pierre J Bertrand, Allison Anderson, Alexandra Hilbert, and Dava Newman. Feasibility of Spacesuit Kinematics and Human-Suit Interactions. *44th International Conference on Environmental Systems*, 2014.

[22] Jose-Luis Blanco. A tutorial on SE(3) transformation parameterizations and on-manifold optimization. Technical report, University of Malaga, 2010.

[23] J.M. Bland and D.G. Altman. Statistical Methods for Assessing Agreement Between Two Methods of Clinical Measurement. *Lancet*, 327:307–310, 1986.

[24] Ton Van Den Bogert. Practical guide to data smoothing and filtering. *Study Material*, pages 1–6, 1996.

[25] D C Boone and S P Azen. Normal range of motion of joints in male subjects. *Journal of Bone and Joint Surgery. American Volume*, 61(5):756–759, 1979.

[26] Johann Borenstein, Lauro Ojeda, and Surat Kwanmuang. Heuristic reduction of gyro drift in IMU-based personnel tracking systems. In *Optics and Photonics in Global Homeland Security V and Biometric Technology for Human Identification VI*, 2009.

[27] Nancy Byl, Wenlong Zhang, Sophia Coo, and Masayoshi Tomizuka. Clinical impact of gait training enhanced with visual kinematic biofeedback: Patients with Parkinson's disease and patients stable post stroke. *Neuropsychologia*, 2015.

[28] Rafael Caldas, Marion Mundt, Wolfgang Potthast, Fernando Buarque de Lima Neto, and Bernd Markert. A systematic review of gait analysis methods based on inertial sensors and adaptive algorithms, 2017.

[29] Valentina Camomilla, Andrea Cereatti, Giuseppe Vannozzi, and Aurelio Cappozzo. An optimized protocol for hip joint centre determination using the functional method. *Journal of Biomechanics*, 39(6):1096–1106, 2006.

[30] Luca Carlone, Zsolt Kira, Chris Beall, Vadim Indelman, and Frank Dellaert. Eliminating conditionally independent sets in factor graphs: A unifying perspective based on smart factors. In *Proceedings - IEEE International Conference on Robotics and Automation*, 2014.

[31] Luca Carlone, Roberto Tron, Kostas Daniilidis, and Frank Dellaert. Initialization techniques for 3D SLAM: A survey on rotation estimation and its use in pose graph optimization. In *Proceedings - IEEE International Conference on Robotics and Automation*, 2015.

[32] Ilaria Carpinella, Davide Cattaneo, Gianluca Bonora, Thomas Bowman, Laura Martina, Angelo Montesano, and Maurizio Ferrarin. Wearable Sensor-Based Biofeedback Training for Balance and Gait in Parkinson Disease: A Pilot Randomized Controlled Trial. *Archives of Physical Medicine and Rehabilitation*, 2017.

[33] Ambra Cesareo, Ylenia Previtali, Emilia Biffi, and Andrea Aliverti. Assessment of breathing parameters using an inertial measurement unit (IMU)-based system. *Sensors*, 19(1):88, 2019.

[34] Elena Ceseracciu, Zimi Sawacha, and Claudio Cobelli. Comparison of markerless and marker-based motion capture technologies through simultaneous data collection during gait: Proof of concept. *PLoS ONE*, 9(3), 2014.

[35] Eric Chalmers, Jonathan Le, Dulai Sukhdeep, Joe Watt, John Andersen, and Edmond Lou. Inertial sensing algorithms for long-term foot angle monitoring for assessment of idiopathic toe-walking. *Gait and Posture*, 2014.

[36] Prudhvi Tej Chinimilli, Sangram Redkar, and Wenlong Zhang. Human activity recognition using inertial measurement units and smart shoes. In *Proceedings of the American Control Conference*, 2017.

[37] J. C.K. Chow. Drift-free indoor navigation using simultaneous localization and mapping of the ambient heterogeneous magnetic field. In *International Archives of the Photogrammetry, Remote Sensing and Spatial Information Sciences - ISPRS Archives*, 2017.

[38] William W Clark and Jeremy R Romeiko. Inertial Measurements of Sports Motion, 2015.

[39] Daniela Colombini and Enrico Occhipinti. *Risk Analysis and Management of Repetitive Actions: A Guide for Applying the OCRA System (Occupational Repetitive Actions)*.

[40] Daniela Colombini and Enrico Occhipinti. Scientific basis of the OCRA method for risk assessment of biomechanical overload of upper limb, as preferred method in ISO standards on biomechanical risk factors, 2018.

[41] Steffi L. Colyer, Murray Evans, Darren P. Cosker, and Aki I.T. Salo. A Review of the Evolution of Vision-Based Motion Analysis and the Integration of Advanced Computer Vision Methods Towards Developing a Markerless System, 2018.

[42] James Connolly, Joan Condell, Brendan O'Flynn, Javier Torres Sanchez, and Philip Gardiner. IMU Sensor-Based Electronic Goniometric Glove for Clinical Finger Movement Analysis. *IEEE Sensors Journal*, 2018.

[43] Glen Cooper, Ian Sheret, Louise McMillian, Konstantinos Siliverdis, Ning Sha, Diana Hodgins, Laurence Kenney, and David Howard. Inertial sensor-based knee flexion/extension angle estimation. *Journal of Biomechanics*, 42(16):2678–2685, 2009.

[44] Matthew S. Cowley, Sarah Margerum, Lauren Harvill, and Sudhakar Rajulu. Model for predicting the performance of planetary suit hip bearing designs. *Advances in Applied Human Modeling and Simulation*, pages 317–326, 2012.

[45] Conor R. Cullinane, Richard A. Rhodes, and Leia A. Stirling. Mobility and agility during locomotion in the mark III space suit. *Aerospace Medicine and Human Performance*, 88(6):589–596, 2017.

[46] Andrea Giovanni Cutti, Alberto Ferrari, Pietro Garofalo, Michele Raggi, Angelo Cappello, and Adriano Ferrari. 'Outwalk': A protocol for clinical gait analysis based on inertial and magnetic sensors. *Medical and Biological Engineering and Computing*, 48(1):17–25, 2010.

[47] Farzin Dadashi, Arash Arami, Florent Crettenand, Gregoire P. Millet, John Komar, Ludovic Seifert, and Kamiar Aminian. A hidden Markov model of the breaststroke swimming temporal phases using wearable inertial measurement units. In *2013 IEEE International Conference on Body Sensor Networks, BSN 2013*, 2013.

[48] Farzin Dadashi, Florent Crettenand, Grégoire P. Millet, and Kamiar Aminian. Front-crawl instantaneous velocity estimation using a wearable inertial measurement unit. *Sensors (Switzerland)*, 2012.

[49] Andreas Daffertshofer, Claudine J.C. Lamoth, Onno G. Meijer, and Peter J. Beek. PCA in studying coordination and variability: A tutorial. *Clinical Biomechanics*, 19(4):415–428, 2004.

[50] Kristine Davis and Ian Meginnis. Testing of the NASA Exploration Extravehicular Mobility Unit Demonstration (xEMU Demo) Architecture at the Neutral Buoyancy Laboratory. 49th International Conference on Environmental Systems, 2019.

[51] Kristine Davis, Richard Rhodes, K Han Kim, Elizabeth Benson, Yaritza Hernandez, Linh Vu, and Sudhakar Rajulu. xEMU Lower Torso Assembly (LTA) Brief Fleet Sizing Study.

[52] Roy B. Davis, Sylvia Õunpuu, Dennis Tyburski, and James R. Gage. A gait analysis data collection and reduction technique. *Human Movement Science*, 1991.

[53] W. H.K. de Vries, H. E.J. Veeger, C. T.M. Baten, and F. C.T. van der Helm. Magnetic distortion in motion labs, implications for validating inertial magnetic sensors. *Gait and Posture*, 2009.

[54] Frank Dellaert. Factor graphs and GTSAM: A hands-on introduction. Technical Report September, 2012.

[55] Scott L Delp, Frank C Anderson, Allison S Arnold, Peter Loan, Ayman Habib, Chand T John, Eran Guendelman, and Darryl G Thelen. OpenSim: Open source to create and analyze dynamic simulations of movement. *IEEE transactions on biomedical engineering*, 54(11):1940–1950, 2007.

[56] Scott L. Delp, J. Peter Loan, Melissa G. Hoy, Felix E. Zajac, Eric L. Topp, and Joseph M. Rosen. An Interactive Graphics-Based Model of the Lower Extremity to Study Orthopaedic Surgical Procedures. *IEEE Transactions on Biomedical Engineering*, 37(8):757–767, 1990.

[57] Kaat Desloovere, Pius Wong, Liesbeth Swings, Barbara Callewaert, Hilde Vandenneucker, and Alberto Leardini. Range of motion and repeatability of knee kinematics for 11 clinically relevant motor tasks. *Gait and Posture*, 2010.

[58] Massimiliano Di Capua and David L. Akin. Body pose measurement system: System validation and range of motion analysis of three pressure suits. In *43rd International Conference on Environmental Systems*, 2013.

[59] Jose Antonio Diego-Mas, Jorge Alcaide-Marzal, and Rocio Poveda-Bautista. Errors Using Observational Methods for Ergonomics Assessment in Real Practice. *Human Factors*, 2017.

[60] Ulrich Dillmann, Claudia Holzhoffer, Yvonne Johann, Sabrina Bechtel, Stefan Gräber, Christoph Massing, Jörg Spiegel, Stefanie Behnke, Jan Bürmann, and Alfred K. Louis. Principal Component Analysis of gait in Parkinson's disease: Relevance of gait velocity. *Gait and Posture*, 39(3):882–887, 2014.

[61] John Etwell. Inertial navigation for the urban warrior. In *Library*, volume 3709, pages 196–204, 1999.

[62] J. Favre, R. Aissaoui, B. M. Jolles, J. A. de Guise, and K. Aminian. Functional calibration procedure for 3D knee joint angle description using inertial sensors. *Journal of Biomechanics*, 42(14):2330–2335, 2009.

[63] J. Favre, B. M. Jolles, R. Aissaoui, and K. Aminian. Ambulatory measurement of 3D knee joint angle. *Journal of Biomechanics*, 41(5):1029–1035, 2008.

[64] J Favre, B.M. Jolles, O Siegrist, and K Animian. Quaternion-based fusion of gyroscopes and accelerometers to improve 3D angle measurement. *The Institution of Engineering and Technology 2006*, 42(6):612–614, 2006.

[65] J Favre, F Luthi, B M Jolles, O Siegrist, B Najafi, K Aminian, K Ne, E J Favre, Ae B Najafi, Ae K Aminian, and Ae O Siegrist. A new ambulatory system for comparative evaluation of the three-dimensional knee kinematics, applied to anterior cruciate ligament injuries. *Knee Surg Sports Traumatol Arthrosc*, 14:592–604, 2006.

[66] Matthew Field, David Stirling, Fazel Naghdy, and Zengxi Pan. Motion capture in robotics review. In *2009 IEEE International Conference on Control and Automation, ICCA 2009*, 2009.

[67] Richard A. Fineman, Timothy M. McGrath, Damian G. Kelty-Stephen, Andrew F. Andrew, and Leia A. Stirling. Objective metrics quantifying fit and performance in spacesuit assemblies. *Aerospace Medicine and Human Performance*, 89(11):985–995, 2018.

[68] G. Kelley Fitzgerald, Sara R. Piva, and James J. Irrgang. Reports of joint instability in knee osteoarthritis: Its prevalence and relationship to physical function. *Arthritis Care and Research*, 51(6):941–946, 2004.

[69] International Organization for Standardization. ISO-TR 12295—Ergonomics—Application document for ISO standards on manual handling (ISO 11228-1, ISO 11228-2 and ISO 11228-3) and evaluation of static working postures (ISO 11226), 2014.

[70] Christian Forster, Luca Carlone, Frank Dellaert, and Davide Scaramuzza. IMU preintegration on manifold for efficient visual-inertial maximum-a-posteriori estimation. In *Robotics: Science and Systems*, 2015.

[71] Milton Friedman. The Use of Ranks to Avoid the Assumption of Normality Implicit in the Analysis of Variance. *Journal of the American Statistical Association*, 1937.

[72] Michael L Gernhardt, Jeffrey A Jones, Richard A Scheuring, Andrew F Abercromby, Jennifer A Tuxhorn, and Jason R Norcross. Risk of Compromised EVA Performance

and Crew Health Due to Inadequate EVA Suit Systems. *Human health and performance risks of space exploration missions*, 2009.

[73] Sebastian Glowinski, Karol Łosiński, Przemysław Kowiański, Monika Waśkow, Aleksandra Bryndal, and Agnieszka Grochulska. Inertial sensors as a tool for diagnosing discopathy lumbosacral pathologic gait: A preliminary research. *Diagnostics*, 2020.

[74] David Graurock, Thomas Schauer, and Thomas Seel. User-Adaptive Inertial Sensor Network for Feedback-Controlled Gait Support Systems. In *International Functional Electrical Stimulation Society*, La Grande-Motte, France, 2016. IFESS.

[75] E. S. Grood and W. J. Suntay. A Joint Coordinate System for the Clinical Description of Three-Dimensional Motions: Application to the Knee. *Journal of Biomechanical Engineering*, 105(2):136, 1983.

[76] Fei Han, Brian Reily, William Hoff, and Hao Zhang. Space-time representation of people based on 3D skeletal data: A review. *Computer Vision and Image Understanding*, 2017.

[77] T. Harada, H. Uchino, T. Mori, and T. Sato. Portable orientation estimation device based on accelerometers, magnetometers and gyroscope sensors for sensor network. In *IEEE International Conference on Multisensor Fusion and Integration for Intelligent Systems*, volume 2003-Janua, pages 191–196, 2003.

[78] K. M. Hays, R. G. Schmidt, W. A. Wilson, J. D. Campbell, D. W. Heckman, and M. P. Gokhale. A submarine navigator for the 21st century. In *Record - IEEE PLANS, Position Location and Navigation Symposium*, pages 179–188, 2002.

[79] A. M. Hollister, S. Jatana, A. K. Singh, W. W. Sullivan, and A. G. Lupichuk. The axes of rotation of the knee. *Clinical Orthopaedics and Related Research*, (290):259–268, 1993.

[80] Harold Hotelling. Analysis of a complex of statistical variables into principal components. *Journal of Educational Psychology*, 24(6):417–441, 1933.

[81] Scott S. Hughes, Christopher W. Haberle, Shannon E. Kobs Nawotniak, Alexander Sehlke, W. Brent Garry, Richard C. Elphic, Samuel J. Payler, Adam H. Stevens, Charles S. Cockell, Allyson L. Brady, Jennifer L. Heldmann, and Darlene S.S. Lim. Basaltic Terrains in Idaho and Hawai'i as Planetary Analogs for Mars Geology and Astrobiology. *Astrobiology*, 2018.

[82] Muhammad Ilyas, Kuk Cho, Seung Ho Baeg, and Sangdeok Park. Drift reduction in IMU-only pedestrian navigation system in unstructured environment. In *2015 10th Asian Control Conference: Emerging Control Techniques for a Sustainable World, ASCC 2015*, 2015.

[83] Muhammad Ilyas, Kuk Cho, Seung Ho Baeg, and Sangdeok Park. Drift reduction in pedestrian navigation system by exploiting motion constraints and magnetic field. *Sensors (Switzerland)*, 2016.

[84] Takuya Isho, Hideyuki Tashiro, and Shigeru Usuda. Accelerometry-based gait characteristics evaluated using a smartphone and their association with fall risk in people with chronic stroke. *Journal of Stroke and Cerebrovascular Diseases*, 2015.

[85] Delaram Jarchi, James Pope, Tracey K.M. Lee, Larisa Tamjidi, Amirhosein Mirzaei, and Saeid Sanei. A Review on Accelerometry-Based Gait Analysis and Emerging Clinical Applications, 2018.

[86] A. R. Jimenez, F. Seco, J. C. Prieto, and J. Guevara. Indoor Pedestrian navigation using an INS/EKF framework for yaw drift reduction and a foot-mounted IMU. In *Proceedings of the 2010 7th Workshop on Positioning, Navigation and Communication, WPNC'10*, 2010.

[87] Brian Johnson, David Williams, and J. Scott Cupples. Results from an Investigation into Extra-Vehicular Activity (EVA) Training Related Shoulder Injuries. In *Space 2004 Conference and Exhibit*, 2004.

[88] M P Kadaba, H K Ramakrishnan, and M E Wootten. Measurement of Lower-Extremity Kinematics during Level Walking. *Journal of Orthopaedic Research*, 8:383–392, 1990.

[89] Breelan M Kear, Thomas P Guck, and Amy L McGaha. Timed Up and Go (TUG) Test. *Journal of Primary Care & Community Health*, 8(1):9–13, 2016.

[90] Dohyung Kee and Waldemar Karwowski. LUBA: An assessment technique for postural loading on the upper body based on joint motion discomfort and maximum holding time. *Applied Ergonomics*, 2001.

[91] Deb A. Kegelmeyer, Sandra K. Kostyk, Nora E. Fritz, Marianne M. Fiumedora, Ajit Chaudhari, Marilly Palettas, Gregory Young, and Anne D. Kloos. Quantitative biomechanical assessment of trunk control in Huntington's disease reveals more impairment in static than dynamic tasks. *Journal of the Neurological Sciences*, 2017.

[92] Kim KJ, Beltran E, Dunn J, Bekdash O, Norcross J, Downs M, and Abercromby A. Characterization of Activities and Postures during Planetary Extravehicular Activities via Inertial Measurement Units. In *American Society of Biomechanics (ASB) Annual Conference*.

[93] Kim KJ, Dunn J, Beltran E, Bekdash O, Norcross J, Downs M, and Abercromby A. A Comparison of Gait Characteristics between Extravehicular Activity Training Environments. In *American Society of Biomechanics (ASB) Annual Conference*.

[94] A D King. Inertial navigation - Forty years of evolution. *Gec Review*, 13(3):140–149, 1998.

[95] S. Kirkpatrick, C. D. Gelatt, and M. P. Vecchi. Optimization by simulated annealing. *Science*, 1983.

[96] C. Kirtley, M. W. Whittle, and R. J. Jefferson. Influence of walking speed on gait parameters. *Journal of Biomedical Engineering*, 1985.

[97] Manon Kok, Jeroen D. Hol, and Thomas B. Schön. An optimization-based approach to human body motion capture using inertial sensors. *IFAC Proceedings Volumes (IFAC-PapersOnline)*, 19(3):79–85, 2014.

[98] Manon Kok, Jeroen D. Hol, and Thomas B. Schön. Using inertial sensors for position and orientation estimation, 2017.

[99] Manon Kok, Sina Khoshfetrat Pakazad, Thomas B. Schon, Anders Hansson, and Jeroen D. Holz. A scalable and distributed solution to the inertial motion capture problem. In *FUSION 2016 - 19th International Conference on Information Fusion, Proceedings*, 2016.

[100] Manon Kok and Thomas B. Schon. Magnetometer calibration using inertial sensors. *IEEE Sensors Journal*, 2016.

[101] Heli Koskimäki, Ville Huikari, Pekka Siirtola, Perttu Laurinen, and Juha Röning. Activity recognition using a wrist-worn inertial measurement unit: A case study for industrial assembly lines. In *2009 17th Mediterranean Conference on Control and Automation, MED 2009*, 2009.

[102] David E. Krebs, Claire E. Robbins, Leroy Lavine, and Robert W. Mann. Hip biomechanics during gait. *Journal of Orthopaedic and Sports Physical Therapy*, 1998.

[103] Frank R. Kschischang, Brendan J. Frey, and Hans Andrea Loeliger. Factor graphs and the sum-product algorithm. *IEEE Transactions on Information Theory*, 2001.

[104] M. A. Lafortune, P. R. Cavanagh, H. J. Sommer 3rd, and A. Kalenak. Three-dimensional kinematics of the human knee during walking. *J Biomech Eng.*, 25(4):347–357, 1992.

[105] Daniel Laidig, Dustin Lehmann, Marc Andre Begin, and Thomas Seel. Magnetometer-free Realtime Inertial Motion Tracking by Exploitation of Kinematic Constraints in 2-DoF Joints. In *Proceedings of the Annual International Conference of the IEEE Engineering in Medicine and Biology Society, EMBS*, 2019.

[106] Daniel Laidig, Thomas Schauer, and Thomas Seel. Exploiting kinematic constraints to compensate magnetic disturbances when calculating joint angles of approximate hinge joints from orientation estimates of inertial sensors. *IEEE International Conference on Rehabilitation Robotics*, pages 971–976, 2017.

[107] Scott C. Landry, Kelly A. McKean, Cheryl L. Hubley-Kozey, William D. Stanish, and Kevin J. Deluzio. Knee biomechanics of moderate OA patients measured during gait at a self-selected and fast walking speed. *Journal of Biomechanics*, 40(8):1754–1761, 2007.

[108] Jung Keun Lee and Tae Hyeong Jeon. Magnetic Condition-Independent 3D Joint Angle Estimation Using Inertial Sensors and Kinematic Constraints. *Sensors*, 19(24):5522, dec 2019.

[109] Robert LeMoyne, Timothy Mastroianni, Michael Cozza, Cristian Coroian, and Warren Grundfest. Implementation of an iPhone for characterizing Parkinson's disease tremor through a wireless accelerometer application. In *2010 Annual International Conference of the IEEE Engineering in Medicine and Biology Society, EMBC'10*, 2010.

[110] Stefan Leutenegger, Simon Lynen, Michael Bosse, Roland Siegwart, and Paul Furgale. Keyframe-based visual-inertial odometry using nonlinear optimization. *International Journal of Robotics Research*, 2015.

[111] Sol Lim and Clive D'Souza. A narrative review on contemporary and emerging uses of inertial sensing in occupational ergonomics, 2020.

[112] Zhao Liu, Jianke Zhu, Jiajun Bu, and Chun Chen. A survey of human pose estimation: The body parts parsing based methods. *Journal of Visual Communication and Image Representation*, 2015.

[113] H J Luinge, P H Veltink, and C T M Baten. Estimating orientation with gyroscopes and accelerometers. *Technology and health care*, 7(6):455, 1999.

[114] H. J. Luinge, P. H. Veltink, and C. T M Baten. Ambulatory measurement of arm orientation. *Journal of Biomechanics*, 40(1):78–85, 2007.

[115] G Lundberg and A Palmgren. Dynamic capacity of rolling bearings. *Acta Polytechnica – Mechanical Engineering Series*, 1:4–51, 1947.

[116] Gustaf Lundberg and A Palmgren. Dynamic capacity of roller bearings. *IVA Handlingar*, 210, 1952.

[117] Todd Lupton and Salah Sukkarieh. Visual-inertial-aided navigation for high-dynamic motion in built environments without initial conditions. *IEEE Transactions on Robotics*, 2012.

[118] Sebastian O H Madgwick, Andrew J L Harrison, and Ravi Vaidyanathan. Estimation of IMU and MARG orientation using a gradient descent algorithm. In *IEEE International Conference on Rehabilitation Robotics*, 2011.

[119] Martina Mancini, Lorenzo Chiari, Lars Holmstrom, Arash Salarian, and Fay B. Horak. Validity and reliability of an IMU-based method to detect APAs prior to gait initiation. *Gait and Posture*, 2016.

[120] Martina Mancini, Mahmoud El-Gohary, Sean Pearson, James Mcnames, Heather Schlueter, John G. Nutt, Laurie A. King, and Fay B. Horak. Continuous monitoring of turning in Parkinson's disease: Rehabilitation potential. *NeuroRehabilitation*, 2015.

[121] Frank J. Massey. The Kolmogorov-Smirnov Test for Goodness of Fit. *Journal of the American Statistical Association*, 1951.

[122] Ruth E. Mayagoitia, Anand V. Nene, and Peter H. Veltink. Accelerometer and rate gyroscope measurement of kinematics: An inexpensive alternative to optical motion analysis systems. *Journal of Biomechanics*, 35(4):537–542, 2002.

[123] Lynn McAtamney and E. Nigel Corlett. RULA: a survey method for the investigation of work-related upper limb disorders. *Applied Ergonomics*, 1993.

[124] James W McBarron II. Past, present, and future: the US EVA program. *Acta astronautica*, 32(1):5–14, 1994.

[125] Timothy McGrath, Richard Fineman, and Leia Stirling. An Auto-Calibrating Knee Flexion-Extension Axis Estimator Using Principal Component Analysis with Inertial Sensors. *Sensors*, 2018.

[126] Timothy McGrath and Leia Stirling. Calibration-free, online estimation of the knee flexion/extension axis using inertial measurement units. In *IEEE/RSJ International Conference on Intelligent Robots and Systems*, September 24-28, 2017, Vancouver, BC, Canada, 2017.

[127] Timothy McGrath and Leia Stirling. Body-Worn IMU Human Skeletal Pose Estimation Using a Factor Graph-Based Optimization Framework. *Sensors (Switzerland)*, 20(23):1–29, dec 2020.

[128] Markus Miezal, Gabriele Bleser, Norbert Schmitz, and Didier Stricker. A generic approach to inertial tracking of arbitrary kinematic chains. In *BODYNETS 2013 - 8th International Conference on Body Area Networks*, 2013.

[129] Markus Miezal, Bertram Taetz, and Gabriele Bleser. On inertial body tracking in the presence of model calibration errors. *Sensors (Switzerland)*, 2016.

[130] Markus Miezal, Bertram Taetz, and Gabriele Bleser. Real-time inertial lower body kinematics and ground contact estimation at anatomical foot points for agile human locomotion. In *Proceedings - IEEE International Conference on Robotics and Automation*, 2017.

[131] Markus Miezal, Bertram Taetz, Norbèrt Schmitz, and Gabriele Bleser. Ambulatory inertial spinal tracking using constraints. In *BODYNETS 2014 - 9th International Conference on Body Area Networks*, 2014.

[132] M.J. Miller, C.P. Pittman, T.G. Graff, A Abercromby, J Norcross, E Benson, H Kim, A Garbino, J Dunn, S.˜P. Chappell, K.H. Beaton, K.J. Kim, M Schubert, L.A. Stirling, T McGrath, G Nguyen, D Coan, and J.S. Cupples. Scientific Physical and Operations Characterization (SPOC) - Capturing Terrestrial Fieldwork in Context. In *Lunar and Planetary Science Conference*, volume 50 of *Lunar and Planetary Inst. Technical Report*, page 2120, mar 2019.

[133] Thomas B. Moeslund and Erik Granum. A Survey of Computer Vision-Based Human Motion Capture. *Computer Vision and Image Understanding*, 81(3):231–268, 2001.

[134] Thomas B. Moeslund, Adrian Hilton, and Volker Krüger. A survey of advances in vision-based human motion capture and analysis, 2006.

[135] Jorge J. Moré. The Levenberg-Marquardt algorithm: Implementation and theory. pages 105–116. 1978.

[136] Anastasios I. Mourikis and Stergios I. Roumeliotis. A multi-state constraint Kalman filter for vision-aided inertial navigation. In *Proceedings - IEEE International Conference on Robotics and Automation*, 2007.

[137] Philipp Muller, Marc Andre Begin, Thomas Schauer, and Thomas Seel. Alignment-Free, Self-Calibrating Elbow Angles Measurement Using Inertial Sensors. *IEEE Journal of Biomedical and Health Informatics*, 21(2):312–319, 2017.

[138] P. S. Myles and J. Cui. I. Using the Bland-Altman method to measure agreement with repeated measures. *British Journal of Anaesthesia*, 99(3):309–311, 2007.

[139] R. Nerino, L. Contin, W. J. Gonçalves Da Silva Pinto, G. Massazza, M. Actis, P. Capacchione, A. Chimienti, and G. Pettiti. A BSN based service for post-surgical knee rehabilitation at home. In *BODYNETS 2013 - 8th International Conference on Body Area Networks*, 2013.

[140] R. Nerino, L. Contin, A. Tirri, G. Massazza, A. Chimienti, G. Pettiti, N. Cau, and V. Cimolin. An improved solution for knee rehabilitation at home. In *BODYNETS 2014 - 9th International Conference on Body Area Networks*, 2014.

[141] Le Nguyen Ngu Nguyen, Daniel Rodríguez-Martín, Andreu Català, Carlos Pérez-López, Albert Samà, and Andrea Cavallaro. Basketball activity recognition using wearable inertial measurement units. In *ACM International Conference Proceeding Series*, 2015.

[142] Jason R. Norcross, Shane M. McFarland, and Robert Ploutz-Snyder. Metabolic Assessment of Suited Mobility using Functional Tasks. *Medicine & Science in Sports & Exercise*, 2016.

[143] E. Occhipinti. OCRA: A concise index for the assessment of exposure to repetitive movements of the upper limbs. *Ergonomics*, 1998.

[144] E. Occhipinti and D. Colombini. Updating reference values and predictive models of the OCRA method in the risk assessment of work-related musculoskeletal disorders of the upper limbs. *Ergonomics*, 2007.

[145] K J O'Donovan, R Kamnik, D T O'Keeffe, and G M Lyons. An inertial and magnetic sensor based technique for joint angle measurement. *J Biomech*, 40(12):2604–2611, 2007.

[146] Fredrik Olsson, Manon Kok, Thomas Seel, and Kjartan Halvorsen. Robust plug-and-play joint axis estimation using inertial sensors. *Sensors (Switzerland)*, 20(12):1, 2020.

[147] Roedolph A. Opperman, James M.A. Waldie, Alan Natapoff, Dava J. Newman, and Jeffrey A. Jones. Probability of spacesuit-induced fingernail trauma is associated with hand circumference. *Aviation Space and Environmental Medicine*, 2010.

[148] SK Pakazad, A Hansson, and MS Andersen. Distributed Primal-dual Interior-point Methods for Solving Loosely Coupled Problems Using Message Passing. *Optimization Methods and Software*, 2015.

[149] Arvid Palmgren. Ball and roller bearing engineering. Technical report, 1959.

[150] Steve Paquette, Claire Gordon, and Bruce Bradtmiller. Anthropometric Survey (ANSUR) II Pilot Study: Methods and Summary Statistics. Technical report, 2009.

[151] Melissa A. Pierre, David Zurakowski, Ara Nazarian, Diana A. Hauser-Kara, and Brian D. Snyder. Assessment of the bilateral asymmetry of human femurs based on physical, densitometric, and structural rigidity characteristics. *Journal of Biomechanics*, 2010.

[152] Ronald Poppe. Vision-based human motion analysis: An overview. *Computer Vision and Image Understanding*, 2007.

[153] Yash B. Rabari, Amol Sanap, D. V. Prasad, and Krunal H. Thadeshwar. The distance of the centre of femoral head relative to the midline of the pelvis: a prospective X-ray study of 500 adults. *International Journal of Research in Orthopaedics*, 2017.

[154] A. Raue, V. Becker, U. Klingmüller, and J. Timmer. Identifiability and observability analysis for experimental design in nonlinear dynamical models. *Chaos*, 2010.

[155] Al Reinhardt and John Magistad. AX-5 space suit reliability model. *SAE Technical Papers*, 99(1990):1057–1065, 1990.

[156] Richard A Rhodes, Brian Battisti, Raymond Ytuarte, and Bradley Schultz. Development and Evaluation of Titanium Spacesuit Bearings. In *46th International Conference on Environmental Systems*, 2016.

[157] Daniel Roetenberg, Henk Luinge, and Per Slycke. Xsens MVN: full 6DOF human motion tracking using miniature inertial sensors. *Xsens Motion Technologies BV, ...*, 2009.

[158] Daniel Roetenberg, Henk J. Luinge, Chris T M Baten, and Peter H. Veltink. Compensation of magnetic disturbances improves inertial and magnetic sensing of human body segment orientation. *IEEE Transactions on Neural Systems and Rehabilitation Engineering*, 13(3):395–405, 2005.

[159] Danuta Roman-Liu. Upper limb load as a function of repetitive task parameters: Part 1—a model of upper limb load. *International Journal of Occupational Safety and Ergonomics*, 2005.

[160] Danuta Roman-Liu. Repetitive task indicator as a tool for assessment of upper limb musculoskeletal load induced by repetitive task. *Ergonomics*, 2007.

[161] Angelo M. Sabatini. Quaternion-based extended Kalman filter for determining orientation by inertial and magnetic sensing. *IEEE Transactions on Biomedical Engineering*, 53(7):1346–1356, 2006.

[162] Angelo Maria Sabatini. Kalman-filter-based orientation determination using inertial/magnetic sensors: Observability analysis and performance evaluation. *Sensors*, 11(10):9182–9206, 2011.

[163] S. S. Sachdev. Canadarm—a review of its flights. *Journal of Vacuum Science & Technology A: Vacuum, Surfaces, and Films*, 1986.

[164] Sarvenaz Salehi, Gabriele Bleser, Attila Reiss, and Didier Stricker. Body-IMU autocalibration for inertial hip and knee joint tracking. In *BodyNets International Conference on Body Area Networks*, 2015.

[165] Nikolaos Sarafianos, Bogdan Boteanu, Bogdan Ionescu, and Ioannis A. Kakadiaris. 3D Human pose estimation: A review of the literature and analysis of covariates. *Computer Vision and Image Understanding*, 2016.

[166] Jojo V. Sayson, Jeffrey Lotz, Scott Parazynski, and Alan R. Hargens. Back pain in space and post-flight spine injury: Mechanisms and countermeasure development, 2013.

[167] Richard A. Scheuring, Charles H. Mathers, Jeffrey A. Jones, and Mary L. Wear. Musculoskeletal injuries and minor trauma in space: Incidence and injury mechanisms in U.S. astronauts. *Aviation Space and Environmental Medicine*, 2009.

[168] Johannes C.M. Schlachetzki, Jens Barth, Franz Marxreiter, Julia Gossler, Zacharias Kohl, Samuel Reinfelder, Heiko Gassner, Kamiar Aminian, Bjoern M. Eskofier, Jürgen Winkler, and Jochen Klucken. Wearable sensors objectively measure gait parameters in Parkinson's disease. *PLoS ONE*, 2017.

[169] P. B. Schmidt, D. J. Newman, and E. Hodgson. Modeling Space Suit Mobility: Applications to Design and Operations. In *SAE Technical Paper Series*, 2010.

[170] Thomas Seel, Jörg Raisch, and Thomas Schauer. IMU-based joint angle measurement for gait analysis. *Sensors (Basel, Switzerland)*, 14(4):6891–909, 2014.

[171] Thomas Seel and Stefan Ruppin. Eliminating the Effect of Magnetic Disturbances on the Inclination Estimates of Inertial Sensors. *IFAC-PapersOnLine*, 50(1):8798–8803, 2017.

[172] Thomas Seel and Thomas Schauer. Joint Axis and Position Estimation from Inertial Measurement Data by Exploiting Kinematic Constraints. In *IEEE International Conference on Control Applications*, pages 0–4, 2012.

[173] Geoffrey K. Seidel, David M. Marchinda, Marcel Dijkers, and Robert W. Soutas-Little. Hip joint center location from palpable bony landmarks-A cadaver study. *Journal of Biomechanics*, 28(8):995–998, 1995.

[174] Ajay Seth, Jennifer L. Hicks, Thomas K. Uchida, Ayman Habib, Christopher L. Dembia, James J. Dunne, Carmichael F. Ong, Matthew S. DeMers, Apoorva Rajagopal, Matthew Millard, Samuel R. Hamner, Edith M. Arnold, Jennifer R. Yong, Shrinidhi K. Lakshmikanth, Michael A. Sherman, Joy P. Ku, and Scott L. Delp. OpenSim: Simulating musculoskeletal dynamics and neuromuscular control to study human and animal movement. *PLoS Computational Biology*, 2018.

[175] K. Alex Shorter, Amy Wu, and Arthur D. Kuo. The high cost of swing leg circumduction during human walking. *Gait and Posture*, 2017.

[176] Sandra J. Shultz and Anh Dung Nguyen. Bilateral asymmetries in clinical measures of lower-extremity anatomic characteristics. *Clinical Journal of Sport Medicine*, 2007.

[177] Benoît Sijobert, Jennifer Denys, Christine Azevedo Coste, and Christian Geny. IMU based detection of freezing of gait and festination in Parkinson's disease. In *2014 IEEE 19th International Functional Electrical Stimulation Society Annual Conference, IFESS 2014 - Conference Proceedings*, 2014.

[178] Leia Stirling, Pedro Arezes, and Allie Anderson. Implications of Space suit Injury Risk for Developing Computational Performance Models. *Aerospace Medicine and Human Performance*, 90(6):1–13, 2019.

[179] Fabio A. Storm, Ben W. Heller, and Claudia Mazzà. Step detection and activity recognition accuracy of seven physical activity monitors. *PLoS ONE*, 2015.

[180] Niko Sunderhauf and Peter Protzel. Switchable constraints for robust pose graph SLAM. In *IEEE International Conference on Intelligent Robots and Systems*, 2012.

[181] Juri Taborri, Marco Bordignon, Francesco Marcolin, Alessandro Bertoz, Marco Donati, and Stefano Rossi. On the OCRA measurement: Automatic computation of the dynamic technical action frequency factor. *Sensors (Switzerland)*, 2020.

[182] Shigeru Tadano, Ryo Takeda, and Hiroaki Miyagawa. Three dimensional gait analysis using wearable acceleration and gyro sensors based on quaternion calculations. *Sensors (Basel, Switzerland)*, 13(7):9321–9343, 2013.

[183] Bertram Taetz, Gabriele Bleser, and Markus Miezal. Towards self-calibrating inertial body motion capture. In *FUSION 2016 - 19th International Conference on Information Fusion, Proceedings*, 2016.

[184] Annick A.A. Timmermans, Henk A.M. Seelen, Richard P.J. Geers, Privender K. Saini, Stefan Winter, Juergen Te Vrugt, and Herman Kingma. Sensor-based arm skill training in chronic stroke patients: Results on treatment outcome, patient motivation, and

system usability. *IEEE Transactions on Neural Systems and Rehabilitation Engineering*, 2010.

[185] Bill Triggs, Philip F. McLauchlan, Richard I. Hartley, and Andrew W. Fitzgibbon. Bundle adjustment – a modern synthesis. In *Lecture Notes in Computer Science (including subseries Lecture Notes in Artificial Intelligence and Lecture Notes in Bioinformatics)*, volume 1883, pages 298–372, 2000.

[186] EsomonuGodfrey Ugochukwu, LukpataPhilip Ugbem, OmamuyovwiM Ijomone, and OkemTheresa Ebi. Estimation of Maximum Tibia Length from its Measured Anthropometric Parameters in a Nigerian Population. *Journal of Forensic Science and Medicine*, 2016.

[187] Eline van der Kruk and Marco M. Reijne. Accuracy of human motion capture systems for sport applications; state-of-the-art review, 2018.

[188] Aliénor Vienne, Rémi P. Barrois, Stéphane Buffat, Damien Ricard, and Pierre Paul Vidal. Inertial sensors to assess gait quality in patients with neurological disorders: A systematic review of technical and analytical challenges, 2017.

[189] Aliénor Vienne-Jumeau, Flavien Quijoux, Pierre Paul Vidal, and Damien Ricard. Wearable inertial sensors provide reliable biomarkers of disease severity in multiple sclerosis: A systematic review and meta-analysis, 2020.

[190] Rachel V. Vitali, Stephen M. Cain, Ryan S. McGinnis, Antonia M. Zaferiou, Lauro V. Ojeda, Steven P. Davidson, and Noel C. Perkins. Method for estimating three-dimensional knee rotations using two inertial measurement units: Validation with a coordinate measurement machine. *Sensors (Switzerland)*, 17(9), 2017.

[191] Rachel V. Vitali, Stephen M. Cain, Lauro V. Ojeda, Michael V. Potter, Antonia M. Zaferiou, Steven P. Davidson, Megan E. Coyne, Clifford L. Hancock, Alyssa Mendoza, Leia A. Stirling, and Noel C. Perkins. Body-worn IMU array reveals effects of load on performance in an outdoor obstacle course. *PLoS ONE*, 2019.

[192] Rachel V. Vitali and Noel C. Perkins. Determining anatomical frames via inertial motion capture: A survey of methods. *Journal of Biomechanics*, 2020.

[193] Rachel V. Vitali, Leia A. Stirling, and Matthew J. Miller. Methodology for the Scientific Physical and Operations Characterization (SPOC) of Terrestrial Fieldwork. In *50th International Conference on Environmental Systems, ICES 2020*, 2020.

[194] Frank W. Warner. *Foundations of Differentiable Manifolds and Lie Groups*. Springer-Verlag, 1983.

[195] Ive Weygers, Manon Kok, Marco Konings, Hans Hallez, Henri De Vroey, and Kurt Claeys. Inertial sensor-based lower limb joint kinematics: A methodological systematic review, 2020.

[196] JØrgen Winkel and Svend Erik Mathiassen. Assessment of physical work load in epidemiologic studies: Concepts, issues and operational considerations. *Ergonomics*, 1994.

[197] Herman J. Woltring. A Fortran package for generalized, cross-validatory spline smoothing and differentiation. *Advances in Engineering Software (1978)*, 1986.

[198] Ge Wu and Peter R. Cavanagh. ISB recommendations for standardization in the reporting of kinematic data. *Journal of Biomechanics*, 1995.

[199] Ge Wu, Sorin Siegler, Paul Allard, Chris Kirtley, Alberto Leardini, Dieter Rosenbaum, Mike Whittle, Darryl D D'Lima, Luca Cristofolini, Hartmut Witte, Oskar Schmid, and Ian Stokes. ISB recommendation on definitions of joint coordinate system of various joints for the reporting of human joint motion—part I: ankle, hip, and spine. *Journal of Biomechanics*, 35(4):543–548, 2002.

[200] Ge Wu, Frans C.T. Van Der Helm, H. E.J. Veeger, Mohsen Makhsous, Peter Van Roy, Carolyn Anglin, Jochem Nagels, Andrew R. Karduna, Kevin McQuade, Xuguang Wang, Frederick W. Werner, and Bryan Buchholz. ISB recommendation on definitions of joint coordinate systems of various joints for the reporting of human joint motion - Part II: Shoulder, elbow, wrist and hand. *Journal of Biomechanics*, 38(5):981–992, 2005.

[201] Seline Wüest, Fabien Massé, Kamiar Aminian, Roman Gonzenbach, and Eling D. de Bruin. Reliability and validity of the inertial sensor-based Timed "Up and Go" test in individuals affected by stroke. *Journal of Rehabilitation Research and Development*, 2016.

[202] Ran Xu, Priyanshu Agarwal, Suren Kumar, Venkat N. Krovi, and Jason J. Corso. Combining skeletal pose with local motion for human activity recognition. In *Lecture Notes in Computer Science (including subseries Lecture Notes in Artificial Intelligence and Lecture Notes in Bioinformatics)*, 2012.

[203] Gary T. Yamaguchi and Felix E. Zajac. A planar model of the knee joint to characterize the knee extensor mechanism. *Journal of Biomechanics*, 1989.

[204] Donguk Yang, Jong Kwan Woo, Khalil Najafi, Sangwoo Lee, Jay Mitchell, and Dorian Challoner. 2ppm Frequency Drift and 300x Reduction of Bias Drift of Commercial 6-Axis Inertial Measurement Units Using a Low-Power Oven-Control Micro Platform. In *2015 IEEE SENSORS - Proceedings*, 2015.

[205] Sylvia X.M. Yang, Martin S. Christiansen, Peter K. Larsen, Tine Alkjær, Thomas B. Moeslund, Erik B. Simonsen, and Niels Lynnerup. Markerless motion capture systems for tracking of persons in forensic biomechanics: An overview. *Computer Methods in Biomechanics and Biomedical Engineering: Imaging and Visualization*, 2014.

[206] Yang Yang, Howard Leung, Lihua Yue, and Liqun Deng. Evaluating human motion complexity based on un-correlation and non-smoothness. *Lecture Notes in Computer Science (including subseries Lecture Notes in Artificial Intelligence and Lecture Notes in Bioinformatics)*, 6298 LNCS(PART 2):538–548, 2010.

[207] Xiaoping Yun and E.R. Bachmann. Design, Implementation, and Experimental Results of a Quaternion-Based Kalman Filter for Human Body Motion Tracking. *Robotics, IEEE Transactions on*, 22(6):1216–1227, 2006.

[208] Erwin V Zaretsky. STLE life factors for rolling bearings. *STLE SPECIAL PUBLICATION SP*, 1992.

[209] Erwin V Zaretsky. Rolling bearing life prediction, theory, and application. *NASA Technical Reports*, (November 2016):66, 2013.

[210] L Q Zhang, D Xu, G Wang, and R W Hendrix. Muscle strength in knee varus and valgus. *Medicine and science in sports and exercise*, 33(7):1194–9, 2001.

[211] Zhengyou Zhang. Parameter estimation techniques: A tutorial with application to conic fitting. *Image and Vision Computing*, 1997.

[212] Zichao Zhang, Guillermo Gallego, and Davide Scaramuzza. On the Comparison of Gauge Freedom Handling in Optimization-Based Visual-Inertial State Estimation. *IEEE Robotics and Automation Letters*, 2018.

[213] Jingdong Zhao. A Review of Wearable IMU (Inertial-Measurement-Unit)-based Pose Estimation and Drift Reduction Technologies. In *Journal of Physics: Conference Series*, 2018.

[214] Rong Zhu and Zhaoying Zhou. A real-time articulated human motion tracking using tri-axis inertial/magnetic sensors package. *IEEE Transactions on Neural Systems and Rehabilitation Engineering*, 12(2):295–302, 2004.

[215] Tobias Zimmermann, Bertram Taetz, and Gabriele Bleser. IMU-to-segment assignment and orientation alignment for the lower body using deep learning. *Sensors (Switzerland)*, 2018.